

INFLUENCE OF DRAWING CONDITIONS ON THE PROPERTIES
OF BISMUTH BORATE GLASS FIBERS

BY
JUERGEN WALKER

A THESIS
SUBMITTED TO THE FACULTY OF
ALFRED UNIVERISTY

IN PARTIAL FULFILLMENT OF THE REQUIREMENTS
FOR THE DEGREE OF
DOCTOR OF PHILOSOPHY
IN
MATERIALS SCIENCE AND ENGINEERING

ALFRED, NEW YORK
JUNE, 2007

Alfred University theses are copyright protected and may be used for education or personal research only. Reproduction or distribution in part or whole is prohibited without written permission from the author.

Signature page may be viewed at Scholes Library,
New York State College of Ceramics, Alfred University,
Alfred, New York.

INFLUENCE OF DRAWING CONDITIONS ON THE PROPERTIES
OF BISMUTH BORATE GLASS FIBERS

BY

JUERGEN WALKER

DIPL.-ING. FA UNIVERSITY ERLANGEN NUREMBERG (2001)

M.S. ALFRED UNIVERSITY (2002)

SIGNATURE OF AUTHOR _____ (Signature on File)

APPROVED BY _____ (Signature on File)
ALEXIS G. CLARE, ADVISOR

(Signature on File)
MATTHEW M. HALL, ADVISORY COMMITTEE

(Signature on File)
WILLIAM C. LACOURSE, ADVISORY COMMITTEE

(Signature on File)
JAMES E. SHELBY, ADVISORY COMMITTEE

(Signature on File)
DOREEN EDWARDS, CHAIR, ORAL THESIS DEFENSE

ACCEPTED BY _____ (Signature on File)
ALASTAIR CORMACK, DEAN
KAZUO INAMORI SCHOOL OF ENGINEERING

ACCEPTED BY _____ (Signature on File)
WILLIAM M. HALL, ASSOCIATE PROVOST
FOR GRADUATE AND PROFESSIONAL PROGRAMS
ALFRED UNIVERSITY

ACKNOWLEDGEMENTS

I imagine the road to a successful Ph.D. degree is long for anyone. I also imagine that it would be even tougher if there is nobody that is willing to help you.

I would like to thank a lot of people for helping me along my road. More people helped me make this journey than I can write about or even remember. So I want to acknowledge you all, even if I do not mention your name.

First and foremost I want to thank my fiancée Laura for her understanding, love and encouragement during all this time. I also want to thank all my family for their support of my decision despite their disagreement.

Second I wish to thank all my teachers, especially my advisor Dr. Clare, who encouraged me to pursue this path in the first place. I want to thank you for your guidance and your patience. And also for kicking me in the behind when I needed it. I also would like to thank my advisory committee, Dr. Hall, Dr. LaCourse and Dr. Shelby for their support. And I would like to thank all the other wonderful teachers at this school for attempting and mostly succeeding in imparting some of their knowledge to me.

And lastly, I would very much like to thank all my friends who helped me during this journey by just being there to listen to me. Laughing and joking. Ranting and raving. You know who you all are. Thank you for being my friends.

Thank you all for keeping me sane.

TABLE OF CONTENTS

ACKNOWLEDGEMENTS	III
TABLE OF CONTENTS	IV
LIST OF TABLES	VII
LIST OF FIGURES	VIII
ABSTRACT	XIII
1 INTRODUCTION	1-1
1.1 ORGANIZATION OF THESIS	1-2
1.2 FOUNDATIONS OF THE PRESENT WORK	1-2
1.3 THESIS GOALS	1-3
1.4 REFERENCES	1-4
2 PRODUCTION AND CHARACTERIZATION OF BULK Bi_2O_3 - B_2O_3 GLASS	2-1
2.1 INTRODUCTION	2-2
2.2 LITERATURE REVIEW	2-3
2.3 EXPERIMENTAL PROCEDURE	2-8
2.3.1 <i>Glass Melting</i>	2-8
2.3.2 <i>Density Measurement</i>	2-8
2.3.3 <i>X-ray analysis of glass</i>	2-8
2.3.4 <i>Spectrometric Analysis of Glass</i>	2-9
2.3.5 <i>Thermal analysis of glass</i>	2-9
2.4 RESULTS	2-12
2.4.1 <i>Glass Melting and Density Measurements</i>	2-12
2.4.2 <i>X-ray Diffraction Measurements</i>	2-12
2.4.3 <i>Spectrometric Analysis of the Glass</i>	2-14
2.4.4 <i>Thermal Analysis of the Glass</i>	2-16
2.5 DISCUSSION AND CONCLUSIONS	2-17
2.6 REFERENCES	2-18
3 PRODUCTION AND CHARACTERIZATION OF Bi_2O_3 - B_2O_3 GLASS FIBERS	3-1
3.1 INTRODUCTION	3-2
3.2 LITERATURE REVIEW	3-3
3.2.1 <i>Glass Fiber Production</i>	3-3
3.2.2 <i>Glass Transition</i>	3-5
3.2.3 <i>Structural Relaxation in Glass</i>	3-8
3.2.4 <i>Sub – T_g Relaxations</i>	3-15

3.2.5	<i>Structural Relaxations in the Glass Transition Range</i>	3-18
3.2.6	<i>Previous work</i>	3-22
3.3	EXPERIMENTAL PROCEDURE.....	3-30
3.3.1	<i>Glass Fiber Drawing</i>	3-30
3.3.2	<i>Fiber Drawing Parameters</i>	3-33
3.3.3	<i>Diameter Measurement of Glass Fibers</i>	3-34
3.3.4	<i>Heat Capacity Measurements</i>	3-35
3.3.5	<i>Pre – T_g Exotherm Measurement</i>	3-35
3.3.6	<i>Calculation of T_F</i>	3-39
3.4	RESULTS	3-42
3.4.1	<i>Fiber Diameters</i>	3-42
3.4.2	<i>Glass Transition Temperatures</i>	3-43
3.4.3	<i>Pre - T_g Exotherms of Bi_2O_3 - B_2O_3 Glass Fibers</i>	3-46
3.4.4	<i>Pre – T_g Exotherm Onset temperatures of Bi_2O_3 - B_2O_3 Glass Fibers</i>	3-49
3.4.5	<i>Fictive Temperature of Bi_2O_3 - B_2O_3 Glass Fibers</i>	3-52
3.4.6	<i>Heat Capacity of Bi_2O_3 - B_2O_3 Glass Fibers</i>	3-60
3.4.7	<i>Change of the glass transition of the fibers on reheating</i>	3-65
3.5	DISCUSSION AND CONCLUSIONS.....	3-68
3.6	REFERENCES	3-73
4	MICRO CONFOCAL RAMAN STUDY	4-1
4.1	INTRODUCTION.....	4-2
4.2	LITERATURE REVIEW	4-3
4.2.1	<i>Raman Spectroscopy</i>	4-3
4.2.2	<i>Confocal Micro Raman Spectroscopy</i>	4-10
4.2.3	<i>Raman Spectroscopy of Borate Glasses</i>	4-11
4.2.4	<i>Raman Studies of Heavy Metal Containing Borate Glasses</i>	4-20
4.3	EXPERIMENTAL PROCEDURE.....	4-26
4.4	RESULTS	4-27
4.5	DISCUSSION AND CONCLUSIONS.....	4-35
4.6	REFERENCES	4-38
5	DEPENDENCE OF HEAT CAPACITY OF FIBERS ON ASPECT RATIO.....	5-1
5.1	INTRODUCTION.....	5-2
5.2	LITERATURE REVIEW	5-3
5.2.1	<i>The heat capacity of an ideal gas</i>	5-3
5.2.2	<i>The Einstein model of heat capacity</i>	5-4
5.2.3	<i>The Debye model of heat capacity</i>	5-7

5.2.4	<i>Heat capacity in amorphous solids via low energy excitations</i>	<i>5-9</i>
5.2.5	<i>Previous work.....</i>	<i>5-11</i>
5.3	EXPERIMENTAL PROCEDURE.....	5-14
5.4	RESULTS	5-16
5.5	DISCUSSION AND CONCLUSIONS.....	5-22
5.6	REFERENCES	5-27
6	SUMMARY AND CONCLUSIONS	6-1

LIST OF TABLES

Table 2.I:	Heat Capacity of Bulk 0.25 Bi ₂ O ₃ – 0.75 B ₂ O ₃ Glass Powder	2-16
Table 3.I:	Glass Transition Temperatures of all Fiber Samples	3-43
Table 3.II:	Pre – T _g Exotherm Areas of all Fiber Samples.....	3-46
Table 3.III:	Pre T _g – Exotherm Onset Temperature.....	3-49
Table 3.IV:	Fictive Temperature Data for Fibers Drawn at all Temperatures.....	3-52
Table 3.V:	Heat Capacity of Fibers Drawn at 525°C	3-60
Table 3.VI:	Heat Capacity of Fibers Drawn at 550°C	3-60
Table 3.VII:	Heat Capacity of Fibers Drawn at 575°C	3-60
Table 4.I:	Types of Borate Groups Occurring in Alkali Borates	4-17
Table 5.I:	Length and Aspect Ratios of T575 S5 Fibers.....	5-16

LIST OF FIGURES

Figure 2.1.	Specific heat capacity curves of baseline, standard sapphire and unknown specimens.....	2-10
Figure 2.2.	XRD pattern of 0.25 Bi ₂ O ₃ – 0.75 B ₂ O ₃ glass.....	2-12
Figure 2.3.	XRD pattern of the crystalline layer on the glass surface.....	2-13
Figure 2.4.	XRD pattern of crystallized material taken from the bushing during drawing	2-14
Figure 2.5.	Raman spectrum of bulk 0.25 Bi ₂ O ₃ – 0.75 B ₂ O ₃ glass	2-15
Figure 3.1.	Design of a typical bushing.	3-4
Figure 3.2.	Property – temperature diagram for a glass.....	3-6
Figure 3.3.	Fictive temperature and glass transition.....	3-7
Figure 3.4.	Effects of cooling and reheating on the properties of a glass according to Varshneya.	3-8
Figure 3.5.	Schematic diagram of structural relaxation of property P with time following a single jump in temperature $\Delta T = T_2 - T_1$	3-9
Figure 3.6.	Influence of one day of aging at room temperature on the pre – T _g exotherm of drawn silicate glass fiber.....	3-16
Figure 3.7.	Change in pre – T _g exotherm behavior of rapidly drawn silicate glass fibers with aging and partial annealing at 593 K.	3-17
Figure 3.8.	Schematic plots of (a) temperature T, (b) equilibrium property P _e and experimentally measured property P with time and (c) P vs T during the stepwise cooling and reheating through the glass transition region.....	3-20
Figure 3.9.	Hysteresis in enthalpy H and derivative α_H during cooling and reheating.	3-21
Figure 3.11.	Pre – T _g exotherm as a function of draw speed and temperature.....	3-23
Figure 3.12.	Integrated exotherm for glass fibers up to the indicated temperature vs draw speed.....	3-25
Figure 3.13.	Dependence of exotherm area spin density on draw rate.	3-26
Figure 3.14.	Pre – T _g exotherm area measured by DSC versus the fiber drawing rate.	3-28
Figure 3.15.	Fictive temperature calculated from measured exotherm area versus ageing time.	3-29

Figure 3.16. Fiber drawing tower.....	3-30
Figure 3.17. Design of the fiber drawing bushing.	3-31
Figure 3.18. Thermocouple placement in the bushing.	3-32
Figure 3.19. Cold welded hermetic DSC pan	3-35
Figure 3.20. Error in pre – T_g exotherm calculations by not terminating integration at T_g	3-37
Figure 3.21. Schematic representation of the determination of pre- T_g areas	3-38
Figure 3.22. Area matching from Moynihan and column integration from Hall.....	3-40
Figure 3.23. Output of spreadsheet program.	3-41
Figure 3.24. Diameters of fibers vs draw speed.....	3-42
Figure 3.25. Glass transition temperatures for fibers drawn at 525°C vs drawing speed.....	3-44
Figure 3.26. Glass transition temperatures for fibers drawn at 550°C vs drawing speed.....	3-44
Figure 3.27. Glass transition temperatures for fibers drawn at 575°C vs drawing speed.....	3-45
Figure 3.28. Pre – T_g exotherm areas vs drawing speed, draw temperature 525°C.....	3-47
Figure 3.29. Pre – T_g exotherm areas vs drawing speed, draw temperature 550°C.....	3-47
Figure 3.30. Pre – T_g exotherm areas vs drawing speed, draw temperature 575°C.....	3-48
Figure 3.31. Pre T_g – exotherm onset temperature for fibers drawn at 525°C.....	3-50
Figure 3.32. Pre T_g – exotherm onset temperature for fibers drawn at 550°C.....	3-50
Figure 3.33. Pre T_g – exotherm onset temperature for fibers drawn at 575°C.....	3-51
Figure 3.34. Fictive temperature of fibers drawn at 525°C and reheated 5 times.	3-55
Figure 3.35. Fictive temperature of fibers drawn at 550°C and reheated 5 times.	3-55
Figure 3.36. Fictive temperature of fibers drawn at 575°C and reheated 5 times.	3-56

Figure 3.37. Fictive temperature of unrelaxed fibers drawn at 525°C vs drawing speed.	3-57
Figure 3.38. Fictive temperature of unrelaxed fibers drawn at 550°C vs drawing speed.	3-57
Figure 3.39. Fictive temperature of unrelaxed fibers drawn at 575°C vs drawing speed.	3-58
Figure 3.40. Fictive temperature of unrelaxed fibers vs drawing temperature for the different drawing speed regions.....	3-59
Figure 3.41. Heat capacity of fibers drawn at 525°C.....	3-62
Figure 3.42. Heat capacity of fibers drawn at 525°C vs drawing speed.	3-62
Figure 3.43. Heat capacity of fibers drawn at 550°C.....	3-63
Figure 3.44. Heat capacity of fibers drawn at 550°C vs drawing speed	3-63
Figure 3.45. Heat capacity of fibers drawn at 575°C.....	3-64
Figure 3.46. Heat capacity of fibers drawn at 575°C vs drawing speed	3-64
Figure 3.47. Reheating cycles of a glass fiber sample, heated to well above T_g	3-65
Figure 3.48. XRD pattern of glass fiber after a 1 hour soak at $T_g + 30^\circ\text{C}$	3-66
Figure 3.49. Change in crystallization in fibers upon reheating above T_g	3-66
Figure 3.50. Change in glass transition over several reheating cycles.....	3-69
Figure 4.1. Comparison between resonance fluorescence and scattering.	4-4
Figure 4.2. Scattering spectrum.	4-5
Figure 4.3. Potential energy curves of the ground and first excited states with the transitions observed in Raman spectrometry, infra – red spectrometry, and Fluorimetry	4-6
Figure 4.4. Principal setup of a confocal microscope.	4-11
Figure 4.5. Conversion of boroxol ring.	4-12
Figure 4.6. Further conversion of boroxol ring.....	4-13
Figure 4.7. Type of borate groups occurring in glasses, derived from analog groups in crystalline compounds	4-14
Figure 4.8. Bright field image of a glass fiber drawn at $T = 525^\circ\text{C}$, $S = 3.5 \text{ m/s}$	4-26
Figure 4.9. Raman spectrum of a $0.25 \text{ Bi}_2\text{O}_3 - 0.75 \text{ B}_2\text{O}_3$ glass fiber drawn at $T = 575^\circ\text{C}$ and a draw speed of 8 m/s	4-27

Figure 4.10. Raman spectra of fibers drawn at $T = 525^{\circ}\text{C}$, drawing speeds as shown.	4-28
Figure 4.11. Raman spectra of fibers drawn at $T = 550^{\circ}\text{C}$, drawing speeds as shown.	4-29
Figure 4.12. Raman spectra of fibers drawn at $T = 575^{\circ}\text{C}$, drawing speeds as shown.	4-30
Figure 4.14. Intensities of the 165 cm^{-1} peak vs drawing speed.....	4-31
Figure 4.15. Intensities of the 370 cm^{-1} peak vs drawing speed.....	4-32
Figure 4.16. Intensities of the 490 cm^{-1} peak vs drawing speed.....	4-32
Figure 4.17. Intensities of the 660 cm^{-1} peak vs drawing speed.....	4-33
Figure 4.18. Intensities of the 960 cm^{-1} peak vs drawing speed.....	4-33
Figure 4.19. Intensities of the 1310 cm^{-1} peak vs drawing speed.....	4-34
Figure 4.13. Bridged anion mode after Lines ($C = \text{cation}$).	4-36
Figure 5.1. Fiber cutter	5-14
Figure 5.2. Fiber preparation via microtome and elution	5-14
Figure 5.3. Cold welded hermetic DSC pan	5-15
Figure 5.4. Heat capacity dependence fibers on aspect ratio at 100°C	5-17
Figure 5.5. Heat capacity dependence of fibers on aspect ratio at 150°C	5-17
Figure 5.6. Heat capacity dependence of fibers on aspect ratio at 200°C	5-18
Figure 5.7. Heat capacity dependence of fibers on aspect ratio at 250°C	5-18
Figure 5.8. Heat capacity dependence of fibers on aspect ratio at 300°C	5-19
Figure 5.9. Heat capacity dependence of fibers on aspect ratio at 350°C	5-19
Figure 5.10. Heat capacity dependence of fibers on aspect ratio at 400°C	5-20
Figure 5.11. T_g dependance of fibers on aspect ratio.....	5-21
Figure 5.12. Averaged heat capacities for different aspect ratio regions.....	5-22
Figure 5.13. Difference in heat capacity between relaxed and unrelaxed fibers at high aspect ratio	5-23
Figure 5.14. DSC plot of fibers heated far above T_g	5-24

Figure 5.15. Change in glass transition height in fibers upon reheating above T_g	5-24
--	------

ABSTRACT

In this study the influence of forming conditions, namely draw temperature and draw speed, on thermal properties of glass fibers of the composition $0.25 \text{ Bi}_2\text{O}_3 - 0.75 \text{ B}_2\text{O}_3$ were examined using mainly DSC measurements and confocal micro – Raman spectroscopy. Glass fibers were drawn at temperatures of 525, 550 and 575°C and draw speeds ranging from 1 to 10 m/sec. DSC measurements were performed to measure glass transition, heat capacity, fictive temperature, and pre – T_g exotherm, both in strength and the onset. Concurrently micro – Raman measurements were used to identify the structural borate groups present in the fibers and their change with forming conditions. Several trends could be observed. As draw speed increases the glass transition decreases, indicating a more disordered structure. Pre – T_g exotherms show a local maximum at draw speeds of 4 m/s. Raman spectroscopy indicates the presence of $[\text{BiO}_6]$ octahedra that are becoming more distorted as the draw speed increases. The local maximum in both the pre – T_g exotherm and the corresponding Raman peak show that there is an optimal distortion. Pre – T_g exotherm onset temperatures show a linear decrease with draw speeds. All this supports the conclusion that there is no major structural rearrangement. Heat capacity shows no overall trends of behavior dependant on forming conditions. These glass fibers also show a decrease in glass transition height during reheating that indicates a decreasing amount of glass. This can either be due to crystallization or phase separation. Finally the aspect ratio of the glass fibers seems to have a direct influence on heat capacity. As the aspect ratio increases the heat capacity of the glass fibers increases suddenly by a factor of two. The exact mechanism for this effect is unclear at this point.

1 Introduction

1.1 Organization of Thesis

This thesis consists of several chapters detailing various investigations into the thermal behavior of bismuth borate glass fibers. The first chapter provides a short introduction into the relaxation behavior of glass and the theoretical basis of this work.

Chapter 2 describes the production and characterization of the bismuth borate glasses used in this work. In chapter 3 the results of the thermal experiments on heat capacity and pre – T_g exotherms on the bismuth borate glass fibers are discussed. Chapter 4 examines the micro confocal Raman analysis of the glass fibers, and lastly chapter 5 will examine the apparent dependance of the heat capacity of bismuth borate glass fibers on their aspect ratio. A final chapter summarizes the conclusions reached.

1.2 Foundations of the Present Work

Relaxation behavior of materials is described as “the time – dependant response of a system to an external perturbation such as mechanical stress or an electrical potential”.¹ In a glass, relaxation refers to the phenomenon that a glass as a super cooled liquid is not in an equilibrium state and as such will try to approach that equilibrium after a change in temperature. The response of the liquid will consist of two parts: first an isostructural change, which is nearly instantaneous and a time – dependant change towards the new equilibrium.¹

The study of relaxation in glass is important for both theoretical and practical purposes. For the theoretical modeling of the glass transition, new models are needed, as the currently available models, while giving a good phenomenological description, still cannot fully explain all features of the of the glass transition.² On the practical side of things, relaxation phenomena are very important technologically. For example in the annealing process of optical components,³ in

the tempering of glass,⁴ in the influence of thermal history on products in rapid manufacturing processes,⁵ in determining residual stress in optical glass fibers after drawing⁶ and determining residual stresses in composite materials with a glassy phase.⁷

A number of studies have examined relaxation behavior in glasses. The strength of the relaxation increases with increasing departure of the glass structure from the equilibrium. This departure is caused by the cooling rate of the glass exceeding the rate at which the glass can relax into the equilibrium structural arrangements as temperature decreases, and is therefore related to cooling rate. In order to better study relaxation behavior larger relaxations can be achieved by increasing the cooling rate of the glass from the melt. The most common methods used to increase cooling rate are roller quenching and fiber drawing. In this work fiber drawing is used to study relaxation behavior.

1.3 Thesis Goals

The overall goal of this thesis work was to provide insight into the structure and the relaxation behavior of bismuth borate glasses. To this end, thermal properties of glass fibers were measured. Bismuth borate glass is a material with several interesting properties, such as a very steep viscosity curve and good fiberizability despite its tendency towards crystallization. In addition confocal Raman spectroscopy was used to provide insight into the structure of the glass fibers as it changes with drawing conditions.

1.4 References

1. J. Huang, "Structural Relaxation in Thin Glass Fibers"; Ph.D. Thesis. Ohio State University, Ann Arbor, Ohio, 1992.
2. E.-J. Donth, *The Glass Transition: Relaxation Dynamics in Liquids and Disordered Materials*; p. 1-63. Edited by A. Zunger, R. Hull, R.M. Osgood Jr., and H. Sakaki. Springer - Verlag, New York, 2001.
3. M.J. Crochet, "Experimental Study of Stress Relaxation during Annealing," *J. Non-Cryst. Solids*, **14** [1] 242-54 (1974).
4. O.S. Narayanaswamy, "Stress and Structural Relaxation in Tempering Glass," *J. Am. Ceram. Soc.*, **61** [3-4] 146-52 (1978).
5. P.K. Gupta, "Glass Fibers for Composite Materials," Ch. 2 in *Fiber Reinforcement for Composite Materials*. Edited by A.R. Bunsell. Elsevier, New York, 1988.
6. G.W. Scherer, "Thermal Stresses in Optical Fibers: Fluid Core Assumption," *J. Non-Cryst. Solids*, **51** [3] 323-32 (1982).
7. C.T. Moynihan, A.J. Bruce, D.L. Gavin, S.R. Loehr, S.M. Opalka, and M.G. Drexhage, "Physical Aging of Heavy Metal Fluoride Glasses - sub-T_g Enthalpy Relaxation in a ZrF₄-BaF₂-LaF₃-AlF₃ Glass," *Polym. Eng. Sci.*, **24** [14] 1117-22 (1984).

2 Production and Characterization of Bulk Bi_2O_3 - B_2O_3 Glass

2.1 Introduction

Heavy metal oxide glasses exhibit interesting properties. These glasses are used in thermal and mechanical sensors, as glass ceramic layers in optical and electronic devices and reflecting windows.^{8,9} Among the most interesting properties are a high refractive index and strong non-linear optical responses.¹⁰ In bismuth borate glasses this behavior has been attributed to the very high polarizability of the bismuth Bi^{3+} ion.^{8,9,11} Recently bismuth borate crystals, especially the BiB_3O_6 phase have been shown to exhibit a very large non – linear optical response.¹²⁻¹⁴ These materials and bismuth borate glasses also show promise in a number of optical applications such as ultra fast optical switching.^{8,9} Also bismuth borate glasses have shown promise as gamma radiation shielding materials.^{15,16} They are less hygroscopic than alkali borates, easier to fiberize and show good controllability of the N_3 vs N_4 groups.

2.2 Literature Review

Some of the earliest work concerning amorphous bismuth was done by Heynes and Rawson¹⁷ in 1957. They repeated an earlier work by others with more control over the sample preparation. The authors melted and quenched bismuth oxide in an attempt to obtain vitreous bismuth oxide. However, they succeeded only after melting in a silica crucible and letting the bismuth oxide absorb an unknown amount of the crucible material. Using this method they were able to determine the maximum content of bismuth oxide in a glass mixture that forms a stable glass. For the bismuth borate system they determined the maximum bismuth oxide content for glass formation to be 57 mol%.

In 1969 Bishay and Maghrabi¹⁸ studied the system again in a systematic manner. They melted reagent grade materials in porcelain crucibles for 5 to 20 min. They used X-ray diffraction to determine the glass formation region to range from 22.5 to 68 mol% Bi_2O_3 . They also investigated the influence of bismuth oxide on the structure of the glass using infrared spectroscopy and doping with Co^{2+} as a tracer. The use of cobalt as a tracer depends on the fact that cobalt can take a four or six – coordinated arrangement in a glass depending on the presence of non – bridging oxygens. If there are few non – bridging oxygens present, the cobalt ions will arrange themselves in an octahedral (six – coordinated) manner, causing a pink color in the glass. However, if there are many non – bridging oxygens present the cobalt ions will take on a four – fold coordination causing a blue color in the glass. The coordinations are also easily distinguished by their characteristic absorption bands; bands at 630-690, 1250 and 1750 nm for the four – fold coordination and bands at 460 and 520 nm for the six – fold coordination. The authors conclude that the introduction of bismuth to boron oxide has three distinct effects on the structure of the glass. Bismuth oxide donates some of its oxygens to the boron network to create four – coordinated sites, it participated in the structural network by forming BiO_3 groups and it introduces non – bridging oxygens. The authors determined a maximum in

BO₄ content to occur at 45 mol% Bi₂O₃.

More systematic work on the physical properties of the bismuth borate system was done by Stehle et al.¹⁹ The authors examined the optical and physical properties of the bismuth borate system from 0 to 88 mol% bismuth oxide. The authors melted their samples in a platinum crucible at 1000°C for 20 min and the samples used were produced by roller quenching. The authors present the thermal stability diagram of the system. The system shows a maximum stability (defined by the authors as $T_g - T_x$) of 120°C at a J value (J: molar ratio of bismuth oxide to boron oxide) of $J = 1.5$ and then it decreases rapidly after that, reaching about 45°C at $J = 7.5$. Glass transition temperature shows an initial increase in T_g with a maximum of 457°C at $J = 0.3$ and a decline thereafter. The authors call on observations by Meera²⁰ and attribute the initial increase in T_g to the formation of dipentaborate groups. The density of the glass increases steadily up to $J = 1$ and then slowly levels off to approach 8.9 g/cm³, the value for pure Bi₂O₃. The molar volume shows a minimum value of 52 cm³/mole until $J = 0.3$ and then starts increasing linearly. The authors attribute this to the destruction of larger borate groups.

Most recently Becker²¹ investigated thermal and optical properties in the bismuth borate system containing 20 – 42.5 mol% Bi₂O₃. The author melted a large amount of reagent grade powders in a covered platinum crucible for 24 h. After casting and remelting, the resulting glass, ca. 75 cm³, was cooled at a rate of 1 K/min to room temperature. DTA measurements determined the onset of crystallization temperature, which shows the presence of two crystalline phases in the region below 60 mol% B₂O₃. X-ray diffraction confirmed the two phases to be Bi₃B₅O₁₂ and BiBO₃. Glass transition temperatures show a peak at 22.5 mol% Bi₂O₃, which agrees with Stehle's¹⁹ results. Linear thermal expansion measurements show a continuous decrease of expansion coefficient with decreasing bismuth oxide content down to a minimum value of $6.1 \cdot 10^{-6}$ 1/K at 22.5 mol% Bi₂O₃. At lower Bi₂O₃ contents the expansion coefficient rises again. The density of the glasses decreases linearly in the examined range as heavy metal content decreases. The same is true for refractive indices, which the

author examined at two different wavelengths. These results conform very nicely with the structural information about the system. Pure B_2O_3 is mainly arranged in boroxol rings (B_3O_6). The addition of Bi_2O_3 breaks these rings and causes the formation of BO_4 groups, whose content peaks at ca 25 mol% Bi_2O_3 and decreases again at higher values of bismuth oxide. Boroxol rings cannot be observed in bismuth borate glasses with more than 25 mol% bismuth oxide. Also due to the existence of compact dipentaborate groups,¹⁹ the most dense or “packed” glass structure occurs at 22.5 mol% as confirmed by the thermal expansion measurements.

Cheng et al.²² examined the crystallization kinetics in the bismuth borate system with bismuth oxide contents from 30 to 60 mol%. Samples were melted in an unknown crucible for 1 h and quenched in a graphite mold. Afterwards the samples were crystallized for 1 h, Infrared spectrometry showed the presence of distorted $[BiO_6]$ octahedra indicating this is the major component of the bismuth network since the characteristic band for $[BiO_3]$ polyhedra is absent. $[BO_3]$ and $[BO_4]$ units were also detected and the conversion of $[BO_3]$ into $[BO_4]$ units with increasing bismuth oxide content can be seen. Analysis of the crystallization kinetics shows that up to 45 mol% bismuth content the increase in heavy metal improves the crystallization stability of the glasses. For bismuth oxide contents of above 50 mol% the glasses exhibit an increased tendency towards crystallization. Crystal growth in bismuth borate glasses occurs as either one- or two-dimensional growth.

Agarwal et al.²³ examined the mixed alkali effect in bismuth borate glass of the composition $(30-x) Li_2O \cdot xK_2O \cdot 20 Bi_2O_3 \cdot 50 B_2O_3$. They melted reagent grade raw materials in a porcelain crucible for 30 min. Samples were made by plate quenching between two carbon plates. The authors examined the optical band gap and the refractive index finding a minimum and maximum, respectively at $x = 15$ mol%, confirming the existence of a mixed alkali effect in these glasses. They characterize these glasses as indirect gap semiconductors.

Measurements of optical properties of bismuth borate glasses and crystals by a number of authors^{9,11,13,14,19,21,24-26} have shown strong non – linear

responses.

Ehrt²⁴ measured a number of physical and optical properties of bismuth borate glasses with up to 73 mol% Bi_2O_3 . The author does not specify the melting techniques used. Ehrt notes that bismuth borate glasses show a high third order nonlinear optical susceptibility, as measured by Dimitrov et al.²⁷

Oprea et al.¹¹ examined refractive indices and ultraviolet absorption edge for bismuth borate glasses containing 25 to 65 mol% bismuth oxide. Samples were melted at 1000 K and then cooled to room temperature at a rate of 100 K/hour. The UV absorption edge was observed to shift to higher wavelengths as bismuth content increases in a linear fashion. The changes in refractive index were described with a modified Sellmeier relation. This implies that for the short wavelength region examined the determining factor is only the bismuth oscillator.

Terashima et al.²⁶ examined the third order optical susceptibility in $\text{PbO} - \text{Bi}_2\text{O}_3 - \text{B}_2\text{O}_3$ glasses. The boron network in these glasses was probed with Raman and ^{11}B NMR spectroscopies. Samples were made from reagent grade powders by melting for 30 min in a platinum crucible in the range of 25 – 65 mol% bismuth oxide. Raman spectroscopy showed the expected trends and the presence of the expected structural units (see Chapter 4). ^{11}B NMR measurements indicate that the maximum amount of $[\text{BO}_4]$ units occurs at 45 mol% Bi_2O_3 . For the measured third order optical susceptibility the bismuth borate glasses showed higher values than the lead borate glasses throughout the examined composition range. The largest observed value was measured for a ternary glass, 70 $\text{PbO} \cdot 15 \text{Bi}_2\text{O}_3 \cdot 15 \text{B}_2\text{O}_3$, with a value 50 times that of silica. These results go along with from those presented by Cheng.²² He noted that a significant change occurs in the crystallization behavior at 45 mol% bismuth oxide content. This is the maximum $[\text{BO}_4]$ content in the glasses examined.

Hirayama and Subbarao²⁸ examined dielectric properties of bismuth borate glasses with bismuth oxide contents from 26 to 74 mol%. Samples were prepared from reagent grade powders by melting in porcelain crucibles for 1 h. This caused approximately 1.5 wt.% SiO_2 and 1.3 wt.% of Al_2O_3 to be absorbed by the glasses. Density and linear expansion coefficients increase steadily with

increasing bismuth content. The sag points were determined and the data exhibits a maximum at 32 mol% bismuth oxide. Infrared spectra measured by the authors show results similar to other authors. The activation energy for conduction in these bismuth borate glasses was determined to range from 79.6 to 100.4 kJ/mol. The dielectric constant is high and not sensitive to frequency in the examined region from $10^2 - 10^6$ 1/s.

2.3 Experimental Procedure

2.3.1 Glass Melting

Reagent grade boric acid and bismuth trioxide were batched to create a glass with the composition $0.25 \text{ Bi}_2\text{O}_3 - 0.75 \text{ B}_2\text{O}_3$. This composition was chosen because it represents the maximum bismuth content that bismuth borate glasses can contain before phase separation becomes a problem.²⁹

50 g batches of the bismuth borate glass were melted in a platinum / 10% rhodium crucible at 1000°C for 30 min. The melt was then poured onto a steel plate and quenched by putting another steel plate on the still liquid glass.

The resultant glass was fritted and used for drawing glass fibers.

2.3.2 Density Measurement

The density of the glass was measured using an immersion method following Archimedes Principle. The weight of pieces of glass was measured in air and suspended in methanol ($\rho = 0.791 \text{ g/cm}^3$). The density was calculated according to the following formula

$$\rho_{\text{glass}} = \frac{m_{\text{dry}}}{m_{\text{dry}} - m_{\text{wet}}} \cdot \rho_{\text{methanol}} \quad (2.1)$$

2.3.3 X-ray analysis of glass

The glass was subjected to powder diffraction X-ray diffractometry. The glass was mechanically separated from any surface crystal and ground in an agate mortar and pestle. The powder was packed into an aluminium sample holder and measured in a X-ray diffractometer^a from an angle of $10 - 140^\circ$ with a step size of 0.05° and a dwell time of 5 sec. $\text{Cu-K}\alpha$ radiation was used. The

^a Siemens Kristalloflex 810

phase identification was performed with MDI Jade 7.0.

2.3.4 Spectrometric Analysis of Glass

The glass was also examined using micro - Raman spectrometry^b. The microscope consists of a 532 nm laser, whose light was focused through an optical fiber into a microscope with a 100x Leitz objective. The reflected light was analyzed by a Peltier – cooled CCD detector and processed with the custom software of the instrument.

The laser was focused onto a single fiber and a spectrum was taken with a 600 lines/mm grating and an integration time of one hour. Care was taken to focus the laser carefully on the exact center of the glass fiber.

2.3.5 Thermal analysis of glass

The heat capacity and glass transition temperature of the glass were measured using a Differential Scanning Calorimeter (DSC)^c. Glass powder was encapsulated in a hermetically sealed aluminium pan. The heating rate for the glass transition measurement was chosen to be 10 K/min. The heat capacity measurements were done according to standard ASTM E 1269 – 99. The heating profile was to hold the sample at a temperature of 80°C for 5 minutes and then heat to 420°C at a rate of 20 K/min and to hold the sample at that temperature for an additional 5 minutes. The first run was done with an empty cell, the second run with a calibration sapphire with a known heat capacity and finally the third run was conducted with the unknown sample. Figure 2.1 shows the three curves schematically.

^b WiTEC CRM 200 Micro Confocal Raman Microscope

^c TA Instruments Q10 and Q100

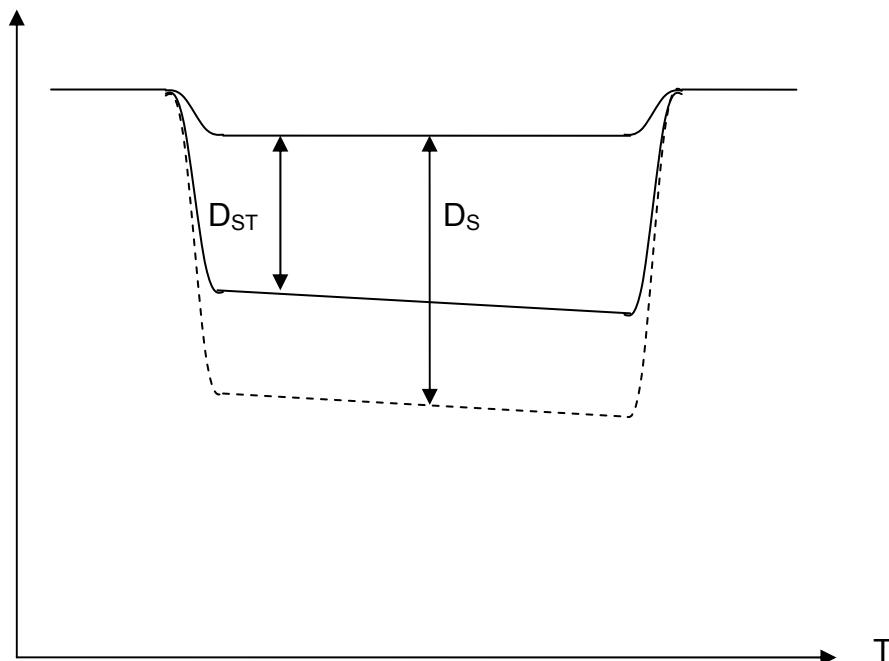


Figure 2.1. Specific heat capacity curves of baseline, standard sapphire and unknown specimens

The following procedure is a summary of ASTM E 1269 – 99. The calorimetric sensitivity of the instrument was calculated according to Equation 2.

$$E = \left[\frac{b}{(60 \cdot D_{st})} \right] \cdot [W_{st} \cdot C_p(st)] \quad (2.2)$$

b : heating rate, K/min

$C_p(st)$: specific heat capacity of the standard sapphire, $J(gK)^{-1}$

E : calorimetric sensitivity of the DSC instrument

D_{st} : vertical displacement between the specimen holder and the sapphire DSC curves, mW

W_{st} : mass of the sapphire, mg

This number was then used to calculate the heat capacity of the unknown sample according to Equation 3.

$$C_p(s) = \frac{60 \cdot E \cdot D_s}{W_s \cdot b} \quad (2.3)$$

$C_p(s)$: Specific heat capacity of the specimen, $J(gK)^{-1}$

D_s : vertical displacement between the specimen holder and the unknown DSC curves, mW

Alternatively some experiments were executed using a modulating differential scanning calorimeter^d. The heating rate was chosen to be 3 K/min with a modulation of 1°C and a period of 60 sec. This combination of parameters was shown to give results consistent with regular DSC measurements.³⁰ Previous measurements³⁰ and the current work confirm this equivalency.

The heat capacity of the sample was measured from 100°C to 400°C in 50°C intervals.

^d TA Instruments Q100

2.4 Results

2.4.1 Glass Melting and Density Measurements

The glass melts had very low viscosity, resulting in an easy pour. The resulting glass was deep brown in color and some formation of a white layer was observed on the surface of the glass. The density of the glass was measured to be $5.91 \pm 0.08 \text{ g/cm}^3$.

2.4.2 X-ray Diffraction Measurements

The glass was also measured in the diffractometer to show that no crystals were formed inside the glass during quenching. The resulting pattern can be seen in Figure 2.2. The pattern only shows a broad amorphous hump and no indication of crystals.

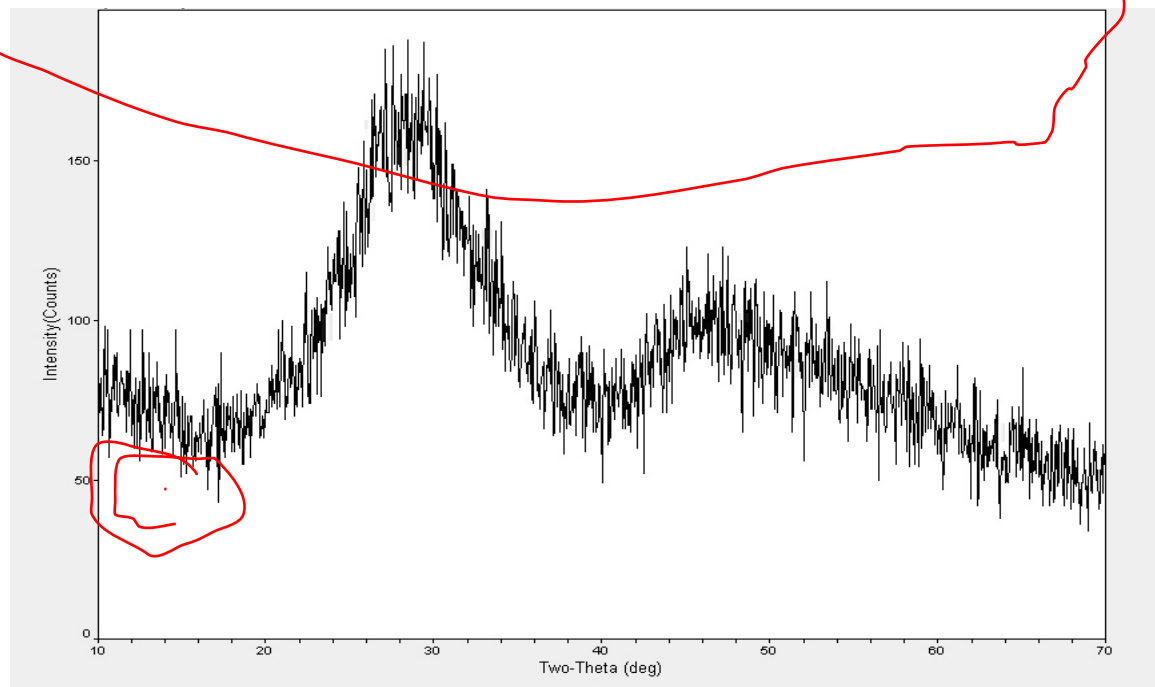


Figure 2.2. XRD pattern of 0.25 Bi_2O_3 – 0.75 B_2O_3 glass

However, a thin white film was formed on the surface of the glass, especially

towards the edges of the poured glass, where the glass was not surrounded on all sides by metal during quenching. To determine the nature of this film, it was mechanically separated and the powder examined in the X-ray diffractometer. The X-ray pattern of the white film can be seen in Figure 2.3.

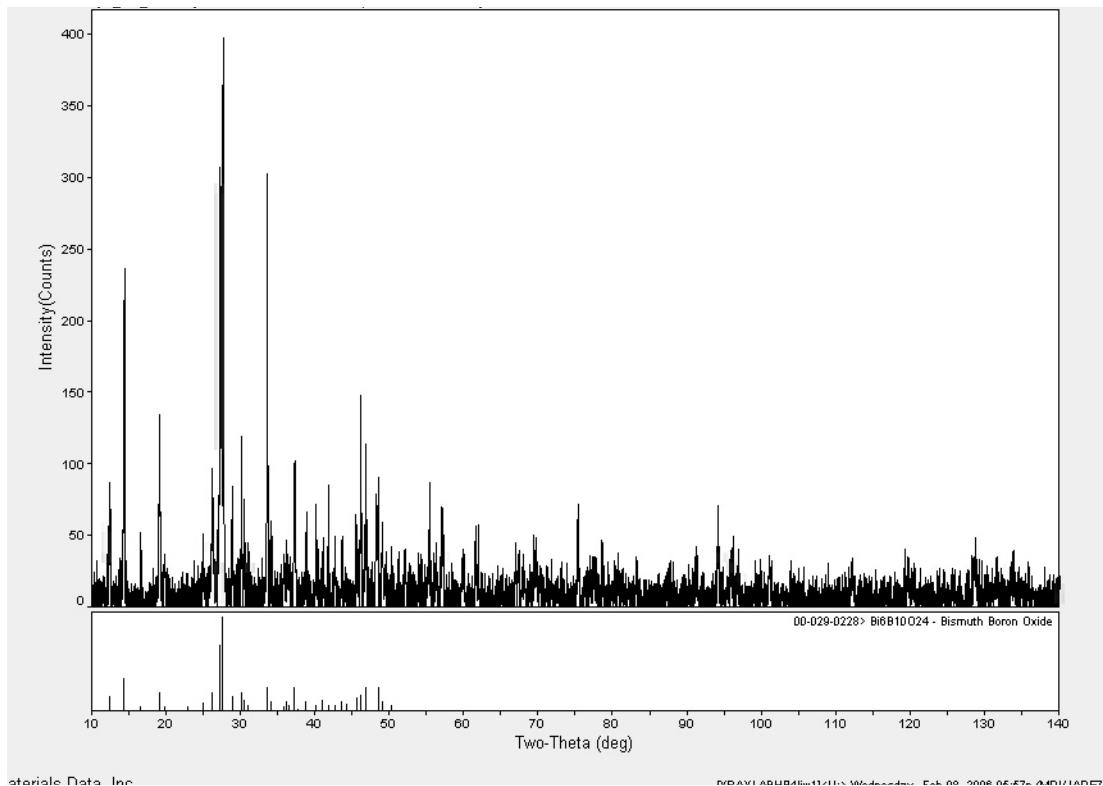


Figure 2.3. XRD pattern of the crystalline layer on the glass surface

The pattern clearly shows the presence of a crystalline phase with a large number of peaks. The crystalline phase was identified as $\text{Bi}_6\text{B}_{10}\text{O}_{24}$. The background of the pattern, which contains a small amorphous hump was subtracted from the pattern to improve pattern matching.

This crystal also occurred on occasion in the bushing during fiber drawing as can be seen in Figure 2.4. In this pattern the background also was subtracted but the pattern is shown without background correction for comparison purposes.

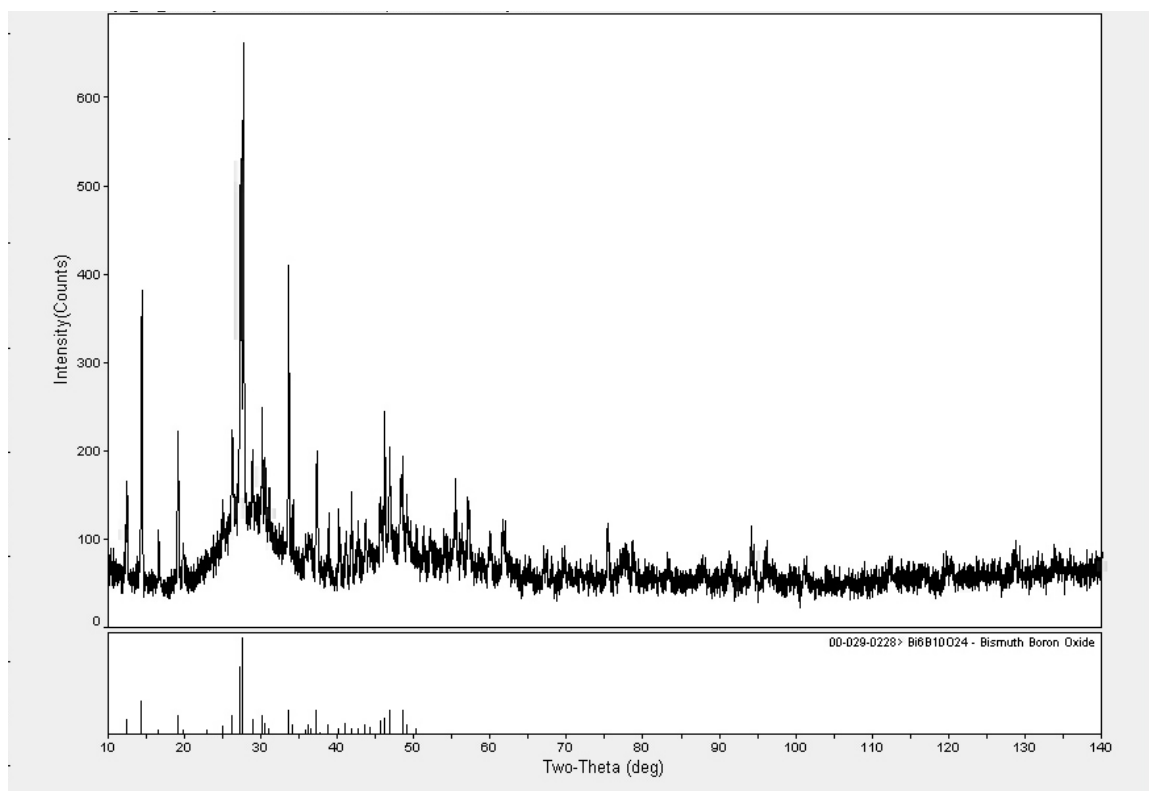


Figure 2.4. XRD pattern of crystallized material taken from the bushing during drawing

2.4.3 Spectrometric Analysis of the Glass

The results of the Raman scan can be seen in Figure 2.5. The spectrum shows several distinct features. There is a broad peak region ranging roughly from $120 - 700 \text{ cm}^{-1}$. Within this region several peaks stand out. Distinct bands can be observed at $165, 365, 490, 660, 1320$ and 2450 cm^{-1} .

For an in depth analysis of the Raman spectrum the reader is referred to chapter 4, which deals entirely with Raman spectroscopy.

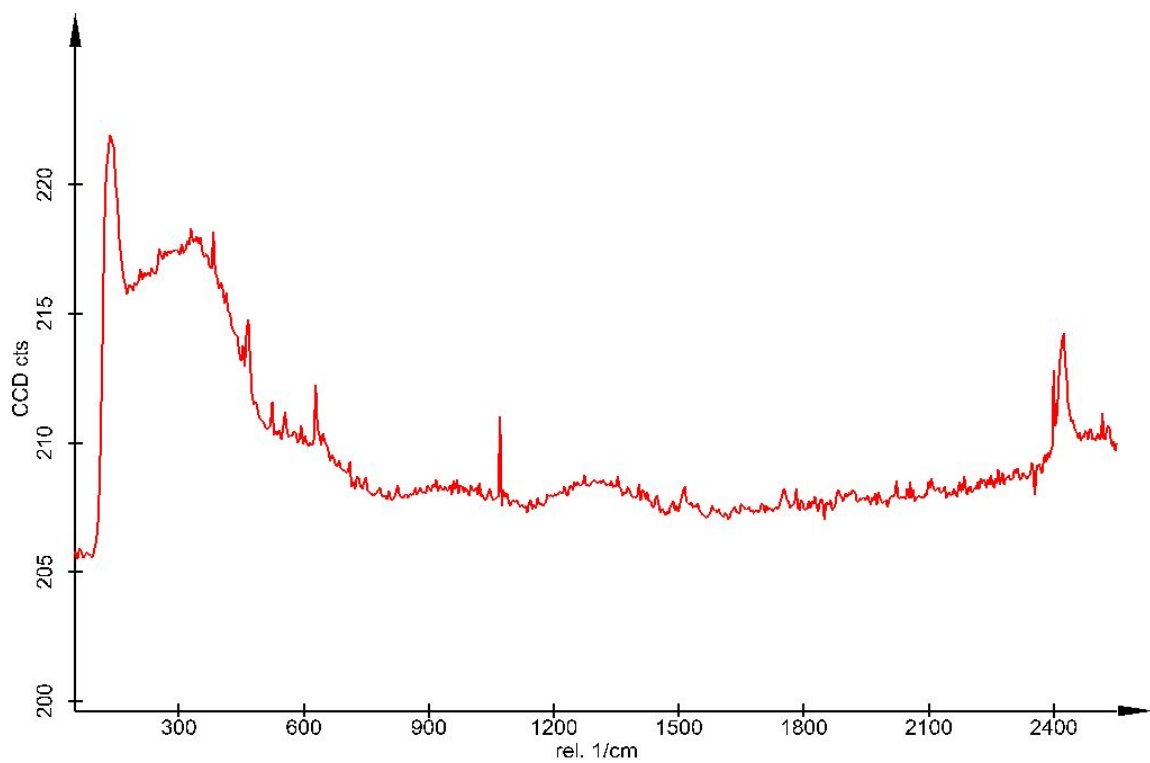
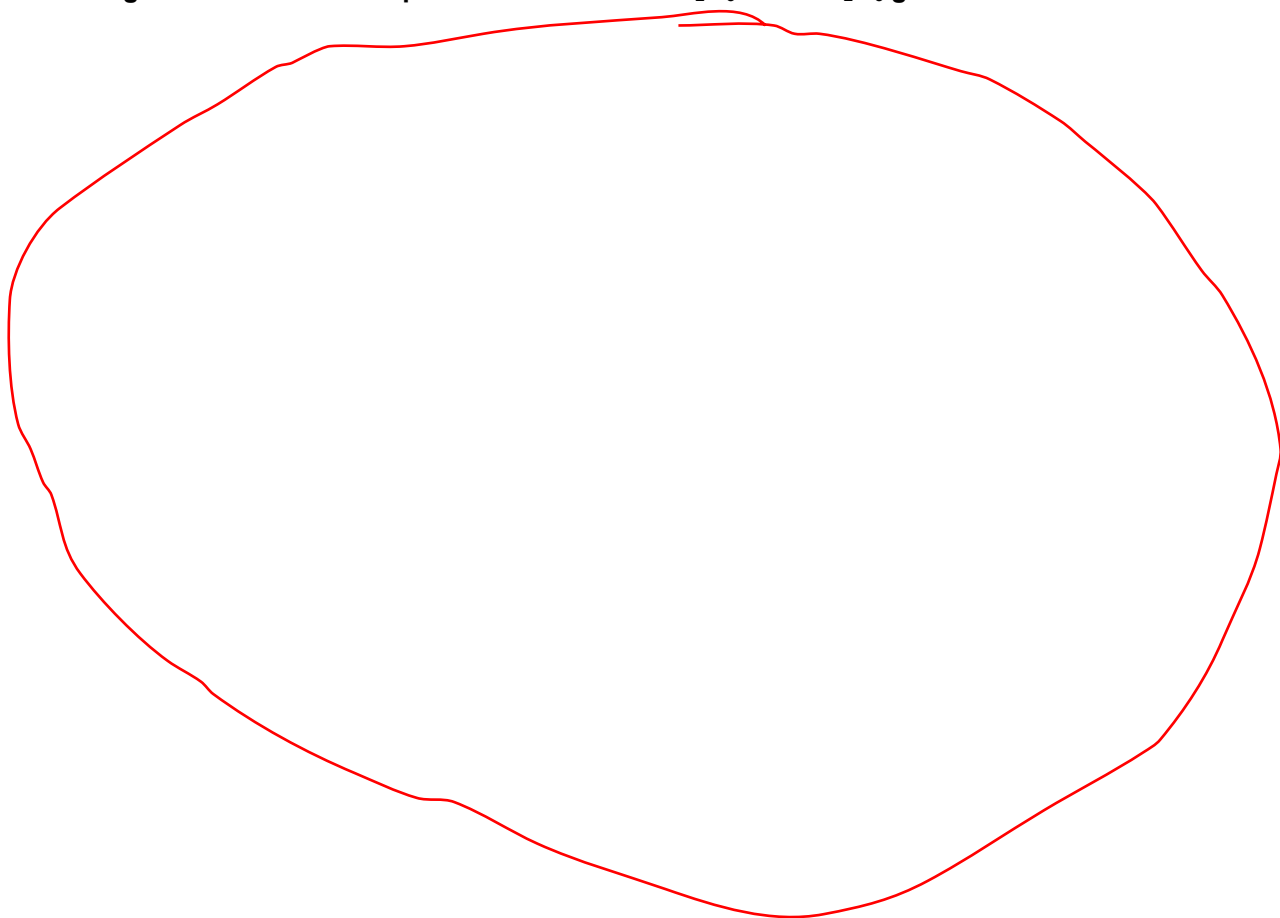


Figure 2.5. Raman spectrum of bulk 0.25 Bi₂O₃ - 0.75 B₂O₃ glass

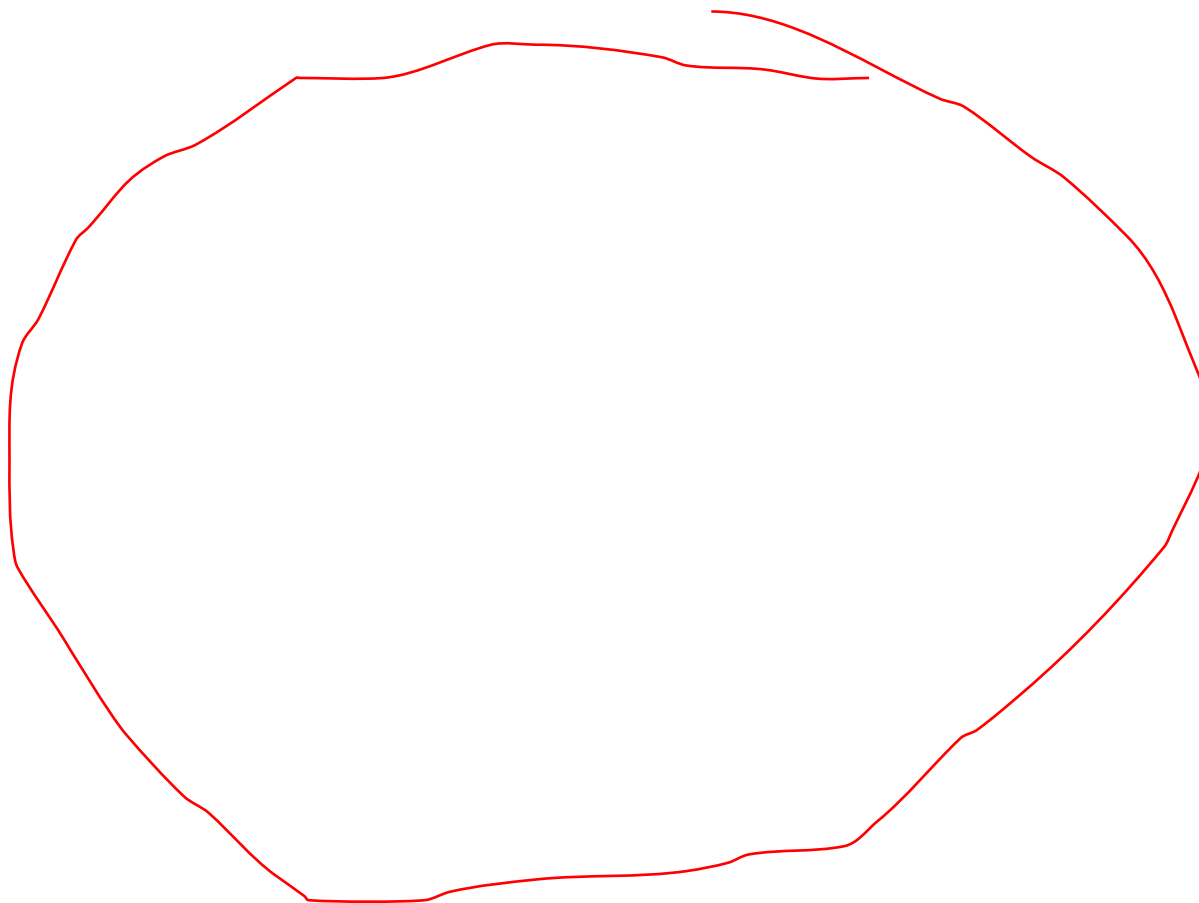


2.4.4 Thermal Analysis of the Glass

The results shown are drawn from six different glass samples, each of which was measured five times. The glass transition temperature of the glass was measured to be $446 \pm 3^\circ\text{C}$. The heat capacity of the bulk glass is shown in Table 2.I.

Table 2.I: Heat Capacity of Bulk $0.25 \text{ Bi}_2\text{O}_3 - 0.75 \text{ B}_2\text{O}_3$ Glass Powder

T [$^\circ\text{C}$]	Cp [$\text{J}(\text{gK})^{-1}$]	
100	$0.799 \pm$	0.034
150	$0.867 \pm$	0.030
200	$0.899 \pm$	0.027
250	$0.927 \pm$	0.031
300	$0.941 \pm$	0.043
350	$0.928 \pm$	0.061
400	$0.937 \pm$	0.053



2.5 Discussion and Conclusions

The X – ray analysis shows that glass is formed during the melting process. The crystallization on the glass surface is minor and of no consequence to the actual fiber drawing. During the drawing process the glass is heated in the bushing to a temperature above the melting point of the crystal and the fibers are drawn quenched fast enough that crystallization does not occur in the fiber.

The physical data measured coincide well with those measured by other authors.^{14,17,19}



2.6 References

1. D.W. Hall, M.A. Newhouse, N.F. Borelli, W.H. Dumbaugh, and D.L. Weidman, "Nonlinear Optical Susceptibilities of High - Index Glasses," *Appl. Phys. Lett.*, **54** [14] 1293-5 (1989).
2. N. Sugimoto, "Ultrafast Optical Switches and Wavelength Division Multiplexing (WDM) Amplifiers Based on Bismuth Oxide Glasses," *J. Am. Ceram. Soc.*, **85** [5] 1083-8 (2002).
3. W.H. Dumbaugh and J.C. Lapp, "Heavy Metal Oxide Glasses," *J. Am. Ceram. Soc.*, **75** [9] 2315-26 (1992).
4. I.-I. Oprea, H. Hesse, and K. Betzler, "Optical Properties of Bismuth Borate Glasses," *Opt. Mater.*, **26** [3] 235-7 (2004).
5. K. Gerth and C. Russel, "Crystallization of $\text{Bi}_4\text{Ti}_3\text{O}_{12}$ from Glasses in the System $\text{Bi}_2\text{O}_3 / \text{TiO}_2 / \text{B}_2\text{O}_3$," *J. Non-Cryst. Solids*, **221** [1] 10-7 (1997).
6. Z. Lin, Z. Wang, C. Chen, and M.-H. Lee, "Mechanism for Linear and Non-Linear Optical Effects in Monoclinic Bismuth Borate (BiB_3O_6) Crystal," *J. Appl. Phys.*, **90** [11] 5585-90 (2001).
7. M.B. Saisudha and J. Ramakrishna, "Optical Absorption of Nd^{3+} , Sm^{3+} and Dy^{3+} in Bismuth Borate Glasses with Large Radiative Transition Probabilities," *Opt. Mater.*, **18** [4] 403-17 (2002).
8. K. Singh, H. Singh, V. Sharma, R. Nthuram, A. Khanna, R. Kumar, S.S. Bhatti, and H.S. Sahota, "Gamma - Ray Attenuation Coefficients in Bismuth Borate Glasses," *Nucl. Instrum. Methods Phys. Res., Sect. B*, **194** [1] 1-6 (2002).
9. N. Singh, K.J. Singh, K. Singh, and H. Singh, "Comparative Study of Lead Borate and Bismuth Lead Borate Glass Systems as Gamma - Radiation Shielding Materials," *Nucl. Instrum. Methods Phys. Res., Sect. B*, **225** [3] 305-9 (2004).
10. M.S.R. Heynes and H. Rawson, "Bismuth Trioxide Glasses," *J. Soc. Glass Technol.*, **41** [1] 347-9 (1957).
11. A. Bishay and C. Maghrabi, "Properties of Bismuth Glasses in Relation to Structure," *Phys. Chem. Glasses*, **10** [1] 1-11 (1969).

12. C. Stehle, C. Vira, D. Hogan, S. Feller, and M. Affatigato, "Optical and Physical Properties of Bismuth Borate Glasses Related to Structure," *Phys. Chem. Glasses*, **39** [2] 83-6 (1998).
13. B.N. Meera and J. Ramakrishna, "Raman Spectral Studies of Borate Glasses," *J. Non-Cryst. Solids*, **159** [1-2] 1-21 (1993).
14. P. Becker, "Thermal and Optical Properties of Glasses of the System Bi_2O_3 - B_2O_3 ," *Cryst. Res. Technol.*, **38** [1] 74-82 (2003).
15. Y. Cheng, H. Xiao, W. Guo, and W. Guo, "Structure and Crystallization Kinetics of Bi_2O_3 - B_2O_3 Glasses," *Thermochim. Acta*, **444** [2] 173-8 (2006).
16. A. Agarwal, V.P. Seth, S. Sanghi, P. Gahlot, and S. Khasa, "Mixed Alkali Effect in Optical Properties of Lithium - Potassium Bismuth Borate Glass System," *Mater. Lett.*, **58** [5] 694-8 (2004).
17. D. Ehrt, "Structure, Properties and Applications of Borate Glasses," *Glass Technol.*, **41** [6] 182-5 (2000).
18. B. Karthikeyan and S. Mohan, "Structural, Optical and Glass Transition Studies on Nd^{3+} - Doped Lead Bismuth Borate Glasses," *Physica B*, **334** [3-4] 298-302 (2003).
19. K. Terashima, T.H. Shimoto, and T. Yoko, "Structure and Nonlinear Optical Properties of PbO - Bi_2O_3 - B_2O_3 Glasses," *Phys. Chem. Glasses*, **38** [4] 211-7 (1997).
20. V.V. Dimitrov, S. King, T. Yoko, and S. Sakka, "Third Harmonic Generation in PbO - SiO_2 and PbO - B_2O_3 Glasses," *J. Ceram. Soc. Jpn.*, **101** [1] 59-63 (1993).
21. C. Hirayama and E.C. Subbarao, "Dielectric Properties of Bismuth Borate Glasses," *Phys. Chem. Glasses*, **3** [4] 111-5 (1962).
22. D. Ehrt, "Structure, Properties and Applications of Borate Glasses," *Glass Technol.*, **41** [6] 182-5 (2000).
23. F.C. Raszewski, "Thermal Analysis of Glass - Covered Amorphous Metal Wires and Amorphous Ribbon for Security Applications"; M.S. Thesis. Alfred University, Alfred, New York, 2004.

3 Production and Characterization of Bi_2O_3 - B_2O_3 Glass Fibers

3.1 Introduction

Glass fibers today are used in many applications, in a great many fields of industry and commerce. Glass fibers are used for a number of properties that make them attractive as a material.

The great strength, low density and low cost of glass fibers make them attractive as a reinforcing material for a number of commercial materials such as cement or polymers. The thermal characteristics of glass fiber, low thermal conductivity and low heat capacity combined with the low density and low cost make glass fibers a premier insulation material. Tailored compositions of glass fibers can serve as thermal insulators in high temperature applications. The transmission capabilities of glass fibers make them attractive in all communications applications. Examples include the transmission of data in information technology in all fields of human life. Glass fibers are also used to transmit images from hard to reach places by using a flexible fiber bundle as a vehicle. Medicine and other fields make regular use of this feature.

In order to understand the dependence of the basic properties of bismuth borate glass on the production conditions, the following study of properties of bismuth borate glass fibers of the composition $0.25 \text{ Bi}_2\text{O}_3 - 0.75 \text{ B}_2\text{O}_3$ was undertaken. Special emphasis was placed on thermal properties such as the heat capacity, glass transition and relaxation behavior, as these parameters play an extremely important role in the processing of the glasses, both in fiberization and later industrial use.

3.2 Literature Review

3.2.1 Glass Fiber Production

— The two most common methods for producing glass fibers are fiber drawing out of a preform and drawing glass fiber with a bushing. The bushing method is the most commonly used method for producing bulk glass fiber, while the preform method is mainly used to produce optical glass fibers from ultra-pure preforms.⁴⁻⁹

In the bushing method glass is melted in a platinum crucible, called a bushing, that has a hole in the bottom. The glass flows through the hole and is pulled into a fiber. The pulling can be done in various ways. For the production of bulk glass fiber mats the glass fibers are produced by forcing glass through multiple holes in a spinning drum. The fibers are most commonly wound onto a rotating drum after pulling in both processes. The bushing method has several advantages. First, the drawing process is continuous, which makes it very attractive as an industrial process. Second, the bushing method does not require a preform. The bushing method, however, accepts glass frit, since the glass is melted in the bushing before drawing.

Bushings are made of platinum metal or platinum / rhodium alloys. Pure platinum metal is preferred in industrial practice, despite having slightly inferior mechanical properties. This is due to the fact that rhodium is slowly lost from the alloy, because rhodium oxide forms at the surface of the bushing and evaporates slowly. Alternative materials are currently not available; all experiments in this direction gave materials that were very expensive to manufacture and had only a very limited lifetime, while at the same time degrading the quality of the product.^{3,4}

Bushing design was and is mainly empiric. There are many different designs available and most manufacturers of glass fibers tend to use a single design for a long time. Special designs for the production of hollow glass fibers

or special glass fibers that are bi-lobal or even tri-lobal (cloverleaf shaped) are available.

✂ A typical bushing design for cylindrical fibers is shown in Figure 3.1.

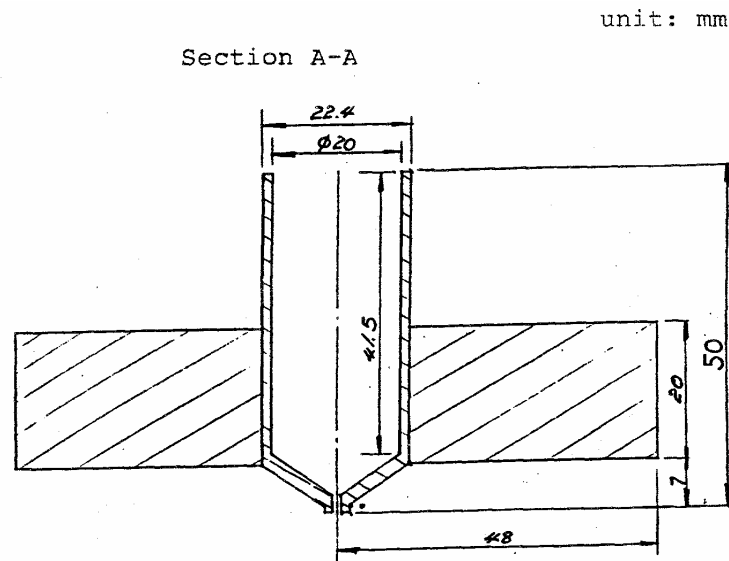



Figure 3.1. Design of a typical bushing. After Chung Tsair Ho.³

Loewenstein^{4,5} and Thomas⁹ state that in order for glass to be drawn into glass fiber, the viscosity must be maintained in a tightly controlled window between 600 and 1000 Poise. At lower viscosities the glass is too fluid and will drip away from the nozzle without forming a fiber. In this case surface tension is dominant. At too high viscosities the tension in the glass is too high and the fiber will break before it is fully formed. Another factor is that at too high viscosities the mass flow from the bushing can become too low and the glass is drawn away faster than it can be replenished from the bushing.

The drawing of glass fibers out of a bushing follows Poiseuille's equation, which states that the rate of mass flow of glass from the bushing \dot{m} , in g/h, is dependant on the radius of the nozzle of the bushing at it's narrowest cross section r , on the height of glass above the nozzle h , the length of the cylindrical section l and the viscosity of the glass η .


$$\dot{m} \propto \frac{r^4 \cdot h}{l \cdot \eta}$$

(3.1)

 In the case of a large bushing the situation becomes more complex, as cooler glass towards the top of the bushing has a higher viscosity and will cause a drag on the glass below it, altering the rate of mass flow.⁴

The diameter of the fiber will then vary at constant mass flow with the drawing speed that is applied to the fibers. That means if the temperature and the head of glass are kept constant, for one given bushing, the diameter of the fiber can be controlled by the speed of the drawing.

3.2.2 Glass Transition¹⁰

 The glass transition is a phenomenon that occurs in a material as it is cooled. When a material is cooled from the melt it will usually crystallize at a given temperature forming a solid crystal. The crystallization causes discontinuities in first order properties such as enthalpy, volume, thermal expansion etc. If the cooling rate is fast enough, depending on the material, the melt can pass through the crystallization temperature and form a supercooled liquid. If this liquid is cooled further it will solidify into an amorphous solid without crystallizing and the first order properties will not show any discontinuities. The temperature range between the liquid and the amorphous solid is referred to as the glass transition region. In this region second order properties, such as heat capacity, are discontinuous.

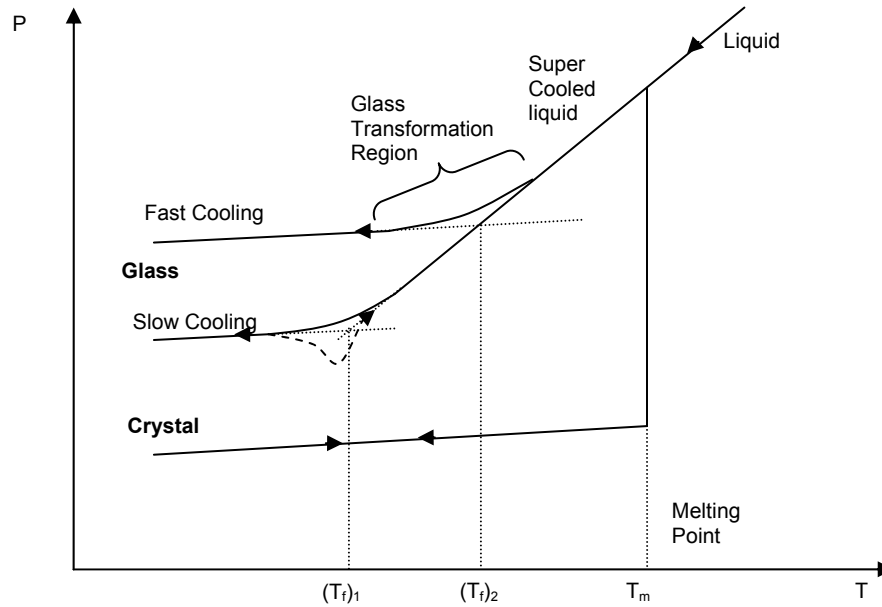


Figure 3.2. Property – temperature diagram for a glass.

The viscosity in the liquid state is very low and the material can relax easily into its equilibrium state. As the viscosity increases, the time necessary for relaxation also increases, making it more difficult for the glass to achieve an equilibrium state. After the material has passed below the glass transition the relaxation times are so large that the achievement of the equilibrium state will take more and more time, therefore the amorphous solid state is not an equilibrium state. The material is said to be a frozen liquid, a glass. Any property of a liquid can be described in two parts. First a part due to changes in structure and a second due to iso – configurational vibration.^{10,11} This causes the properties of an amorphous solid to be influenced not only by temperature and pressure but also by the history of thermal treatments. First order thermodynamic properties have not only a temperature and configuration dependant vibrational contribution but also a temperature independent configurational contribution. For example, enthalpy in an amorphous solid increases if the cooling rate increases. Second or higher order properties only possess vibrational contributions, because when a material is in a solid state, the configuration does not change. This means that the derivative of the

configurational contribution with respect to temperature is zero. This results in the interesting observation that although second order properties can be the same for two different amorphous solids even though first order properties can be different.

All properties of amorphous solids have both vibrational and configurational contributions in the glass transition range, although the configurational part is smaller than in a liquid.

The state of the amorphous solid can be characterized by the fictive temperature, a concept first described by Tool.¹³ The fictive temperature is the temperature at which the liquid and the glass have the same structure. It is influenced by thermal history the same way that the glass transition is and can be roughly found by interpolating the glass and liquid lines as seen in Figure 3.3.

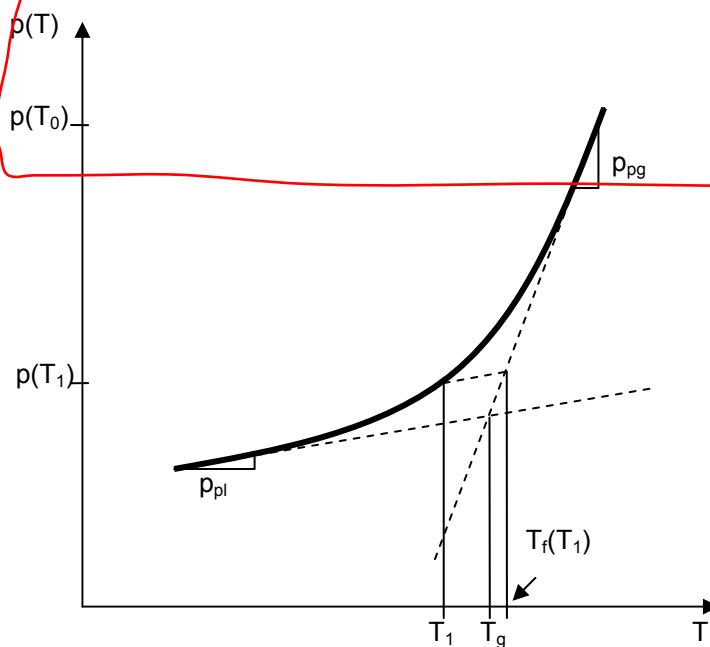


Figure 3.3. Fictive temperature and glass transition. After Scherer.¹⁴

3.2.3 Structural Relaxation in Glass

Structural relaxation is the process by which a glass in a non-equilibrium state approaches equilibrium. It is dependant on the thermal history of the glass, especially the heating and cooling rates and is usually discussed with respect to a single property such as heat capacity. A number of books^{14,15,17} and review articles^{13,16-18} give a detailed description of the evolution of the modeling of structural relaxation in glass.

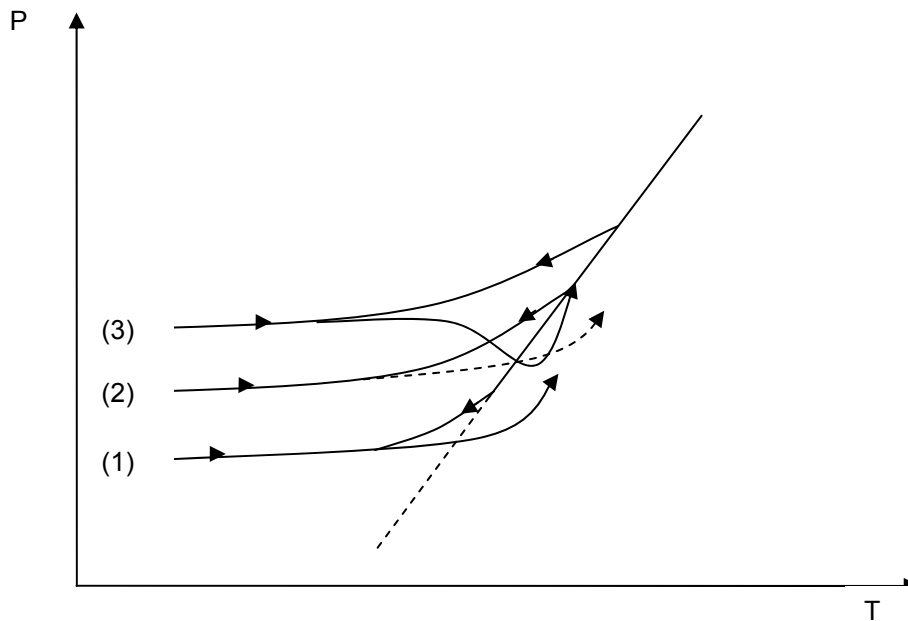


Figure 3.4. Effects of cooling and reheating on the properties of a glass according to Varshneya.¹⁰

The simplest model applied to structural relaxation in glasses is a model based on the well known Maxwell equation, given by

$$P = P_0 \exp \left[- \left(\frac{t}{\tau_p} \right) \right] \quad (3.2)$$

with P being a property of the glass with a value of P_0 at a time $t = 0$ and with τ_p being the relaxation time for the property P . This type of model is shown in Figure 3.5

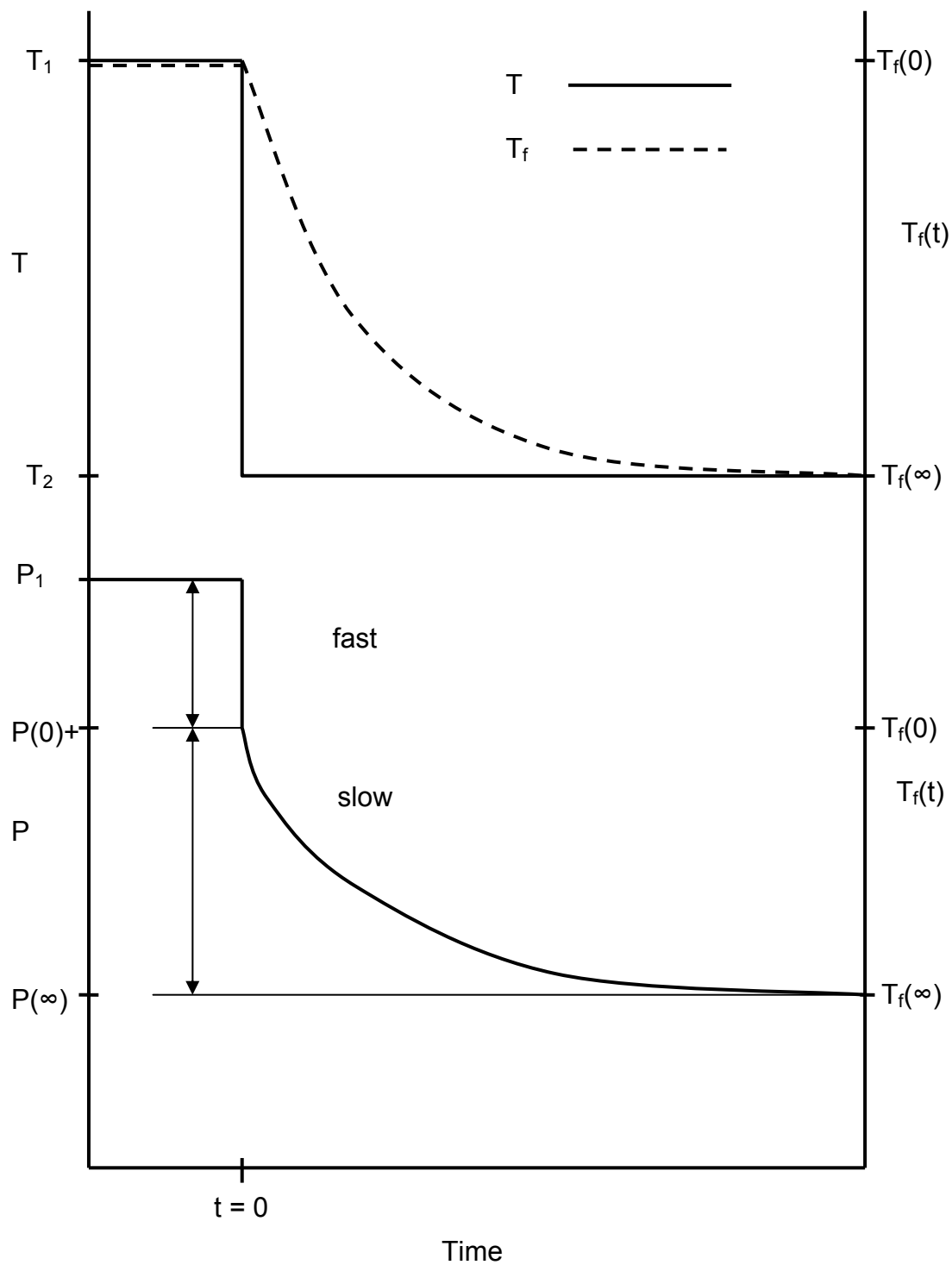


Figure 3.5. Schematic diagram of structural relaxation of property P with time following a single jump in temperature $\Delta T = T_2 - T_1$. After Scherer.¹⁴

The first model of structural relaxation was conceived by Tool.^{13, 19} He first developed the fictive temperature concept based on the analysis of a viscoelastic body to a change in temperature. He also was the first to account for transition range behavior in a glass, at least qualitatively, and he suggested that the changes in the glass are not only due to the change in temperature but also due to the change in structure, as portrayed by the change in fictive temperature. He was able to fit his data with the following equation,

$$\frac{dT_f}{dT} = K(T - T_f) e^{T/g} e^{T_f/h} \quad (3.3)$$

which can be rewritten as

$$\frac{dT_f}{dt} = \frac{T - T_f}{\tau_p} \quad (3.4)$$

This equation shows the effects of the actual and fictive temperatures upon the viscosity of the glass in the first and second exponential terms respectively, with g, h and K being fitting parameters determined empirically from data. This model shows a linear dependence of relaxation with respect to the driving force (T - T_f). The non – linearity is contained in the dependence of the fictive temperature on the viscosity of the glass. Tool concludes that the glass can be described totally by its temperature,, pressure, volume and fictive temperature, which represents the structure of the glass. This leads to the an Arrhenian description of relaxation time given by,

$$\tau_p = \tau_0 e^{(-A_1 T - A_2 T_f)} = \tau_0 e^{(\Delta H / RT)} \quad (3.5)$$

The underlying assumption is that the glass undergoes only a small departure from equilibrium and the model is only valid for small temperature ranges. This concept allows a glass to be described with a single structural parameter, but this model is not adequate especially with glasses that have undergone a complex thermal history.

The famous “cross-over” experiments performed by a number of authors, such as Ritland,²⁰ Spinner and Napolitano²¹ and others²²⁻²⁵ demonstrated that a single fictive temperature is not sufficient to describe the state of a glass

completely. They observed the model did not account for thermal history. In a classic study by Hara et al.,²² the authors studied the density of soda lime silicate glass. They took equally treated glass samples and equilibrated them at 500°C and 560°C and then changed the temperature of both classes of samples to 530°C. They studied the density evolution of the samples with time and found that the relaxation times of the two different sample classes are not equal. The glass that had been equilibrated at 560°C, with a higher fictive temperature and therefore more open structure, approached equilibrium faster than the glass equilibrated at 500°C, despite the equal jumps in temperature. This demonstrates conclusively that thermal history influences have to be taken into account when trying to describe glasses.

Narayanaswamy²⁵ refined Tools model by assuming that the total thermal history of a glass is calculable by summing up a number of smaller relaxation step changes to account for the total thermal history of the glass. This approach leads to treating the total relaxation process as the summation of a number of relaxation processes that describe the total effect. Narayanaswamy assumed that the “functional form” does not change with temperature. He termed materials that exhibit this behavior thermorheologically simple. After a step change in temperature, $\Delta T = T_2 - T_1$, he modeled the glasses response on the function

$$M_p^*(t, \Delta T) = \frac{(p - p_2)}{(p_1 - p_2)} = \frac{(T_{fp} - T_2)}{(T_1 - T_2)} = \exp(-kt) = \exp\left(-\frac{t}{\tau_p}\right) \quad (3.6)$$

with p_1 being the initial property value at T_1 , and p_2 being the ultimate property value at T_2 . He also normalized this function so that $M_{p(0)}^* = 1$ and $M_{p(\infty)}^* = 0$. τ_p is the relaxation time.

This observation leads to the use of the modified Kohlrausch – William – Watts equation, or stretched exponential, to describe this model

$$M_p^*(t) = \exp\left[-\left(\frac{t}{\tau}\right)^\beta\right] = \sum_k w_k \exp\left[-\left(\frac{t}{\tau_k}\right)\right] \quad (3.7)$$

with $M_p^*(t)$ being the response function, t the time, τ_k the characteristic relaxation

times and w_k the weights for the individual relaxation processes. The relationship of this model and the simpler Maxwell model, with $\beta = 1$, is obvious. The value of β describes the width of the relaxation time distribution. Large values of β imply a narrow distribution of relaxation times, small values imply the presence of faster relaxation processes.

Moynihan et al.²⁶ used the assumptions of both Tool and Narayanaswamy to modify equation 3.5 to yield

$$\tau_p = \tau_0 \exp \left[x \frac{\Delta H}{RT} + (1-x) \frac{\Delta H}{RT_f} \right] \quad (3.8)$$

with $0 \leq x \leq 1$. This accounts for the missing non – linearity parameter in Tool's model. The value of x is empirical, but it allows the separation of the structural and temperature contributions to relaxations times. Moynihan et al.^{24,26-29,41} use the assumption of Tool and Narayanaswamy, that the distribution of relaxation times is constant at all temperatures, in other words that the materials behaves in a thermorheologically simple fashion. In the work of these authors fictive temperature is expressed as

$$T_f(T) = T_0 + \int_{T_0}^T dT' \left\{ 1 - \exp \left[- \left(\int_{T'}^T \frac{dT''}{q\tau} \right)^\beta \right] \right\} \quad (3.9)$$

during heating or cooling. T_0 is an equilibrium temperature and q is the heating or cooling rate. DeBolt et al.³⁰ and Eastal et al.³¹ successfully used this mathematical model to fit data for B_2O_3 and As_2Se_3 , respectively and arrived at β values of 0.65 for B_2O_3 and 0.67 for As_2Se_3 for enthalpy data. In the data for B_2O_3 the b value for refractive index data was fitted with 0.83.³⁰ This may be an indication that the parameters of relaxation differ between material properties.

Adam and Gibbs³² proposed another model for relaxation near and below the glass transition using primarily polymer data. They give the relaxation time by

$$\tau_p = \tau_0 \exp \left(\frac{\Delta \mu S_C^*}{kTS_C} \right) \quad (3.10)$$

where k is the Boltzman constant, $\Delta\mu$ is the potential barrier to rearrangement per molecule, S_C is the configurational entropy and S_C^* is the configurational entropy of the smallest rearranging unit. This model is based on the assumption of cooperatively rearranging units of molecules. As the temperature drops, the number of available configurations for the molecular groups decreases, which allows the viscosity to increase. The configurational entropy can be derived using

$$S_C = \int_{T_2}^T \frac{\Delta C_p}{T} dT \quad (3.11)$$

with C_p being the configurational heat capacity and T_2 being the Kauzmann temperature, which is the temperature at which S_C extrapolates to zero.

The models given so far all assumed that the materials in question are thermorheologically simple, i.e. the relaxation function does not change with temperature or glass structure. The other assumption made is that there is only a small variation in temperature and only a small departure from equilibrium. These assumptions are clearly not true in the case of materials such as glass fibers and all previously presented models fail to accurately model the behavior of glass fibers.^{3,1217} A number of researchers have proposed an extension to the thermorheological simple model, termed the thermorheological complex model. Rhekson¹⁶ and Ducroux³⁶ first proposed this model by assuming that the shape of the structural relaxation function is a function of temperature. They gave the relationship of

$$\beta(T) = 1 \quad \text{when } T > T^\dagger \quad (3.12)$$

$$\beta(T) = b \left(1 - \frac{T_0}{T} \right) \quad \text{when } T^\dagger \geq T \geq T_0$$

with b and T_0 being adjustable parameters and T^\dagger being the temperature at which $\beta(T)$ is equal to unity. This allows them to model the relaxation time for a given property p by

$$\tau_p = \left(\beta w_c^{1-\beta} \tau_0 (T) \right)^{1/\beta} = \left(\beta w_c^{1-\beta} \exp\left(\frac{H}{T}\right) \right)^{1/\beta} \quad (3.13)$$

where w_c and τ_0 are fixed and H is an adjustable parameter. At temperatures above T^\dagger this model reduces the relaxation time to an Arrhenius type equation, whereas below T^\dagger the form of the equation resembles the Kohlrausch – William – Watts equation. As given above the relaxation function can be represented by

$$M_p(t) = \exp \left[- \left(\frac{t}{\tau_p(T_r)} \right)^{\beta(T_r)} \right] = \sum_{k=1}^n g_k \exp \left[- \left(\frac{t}{\tau_{pk}(T_r)} \right)^{\beta(T_r)} \right] \quad (3.14)$$

with the partial relaxation times, τ_{pk} , being defined in terms of configurational entropy and activation energy, all of which can be generated during numerical analysis.

$$\tau_{pk}(T) = \tau_{pk0} \exp \left[\frac{Q_k}{T \Delta S_c(T_{ik}, T)} \right] \quad (3.15)$$

The configurational entropy is approximately expressed by

$$\Delta S_c(T_{ik}, T) \approx \int_{T_{ik}}^T \frac{C_{pl}(T') - C_{pg}(T')}{T'} dT' \quad (3.16)$$

and the Kauzmann temperatures, T_{ik} , are given by

$$T_{ik} = A_1 \exp \left[- \left(\frac{\tau_{pk}(T_r)}{\tau_p(T_r)} \right)^{\beta(T_r)} \right] + B_1 \quad (3.17)$$

with A_1 and B_1 being two adjustable parameters.

The model has accounted for the structural relaxation of glasses formed by moderate cooling and rapidly cooled glass fibers in some cases.^{22,33-36, 5, 52, 62, 63} But Ho³ reported relaxation behavior in silicate fibers drawn under extreme conditions that cannot be explained by either the thermorheological simple or complex models.

3.2.4 Sub – T_g Relaxations

Relaxations in glasses can occur well below their glass transition range, as a number of authors have clearly demonstrated^{3,24,37-42} for various different glass systems. The glass transition range was low for most examined glass systems,³⁸⁻⁴³ but the phenomenon was also observed in silicate based fiber glass systems.^{3,35,44} Brawer¹⁵ characterized sub – T_g relaxations by an activation energy that is approximately one third to one half of that for relaxation processes in the glass transition range. This energy is an inferred, apparent, value, since the actual measurement in this relaxation scheme is outside of reasonable experimental times. It is however a useful indicator of the structural changes taking place during these relaxation processes.

In a glass fiber one expects relaxation processes to take place at temperatures 200 K or more below T_g , due to the rapid cooling of the glass during the fiber draw process. This rapid cooling of the fiber results in a lower effective viscosity of the glass which in turns presents a lower barrier to structural rearrangement. Defects, such as broken bonds and unfavorable, high-energy bonding arrangements, also play an important role in relaxations at low temperatures. In Figure 3.6 Ho³ shows the DSC traces of a silicate glass fiber that is freshly drawn and one aged one day at room temperature. The glass transition temperature for these glasses is on the order of 800 K. There is a clearly visible exotherm peak showing at 600 K that disappears after even one days aging at room temperature, indicating some relaxation processes taking place. The broad exotherm region, extending for several hundreds of degrees, however is unaffected by the aging at room temperature. This hints at the presence of at least two different relaxation processes.

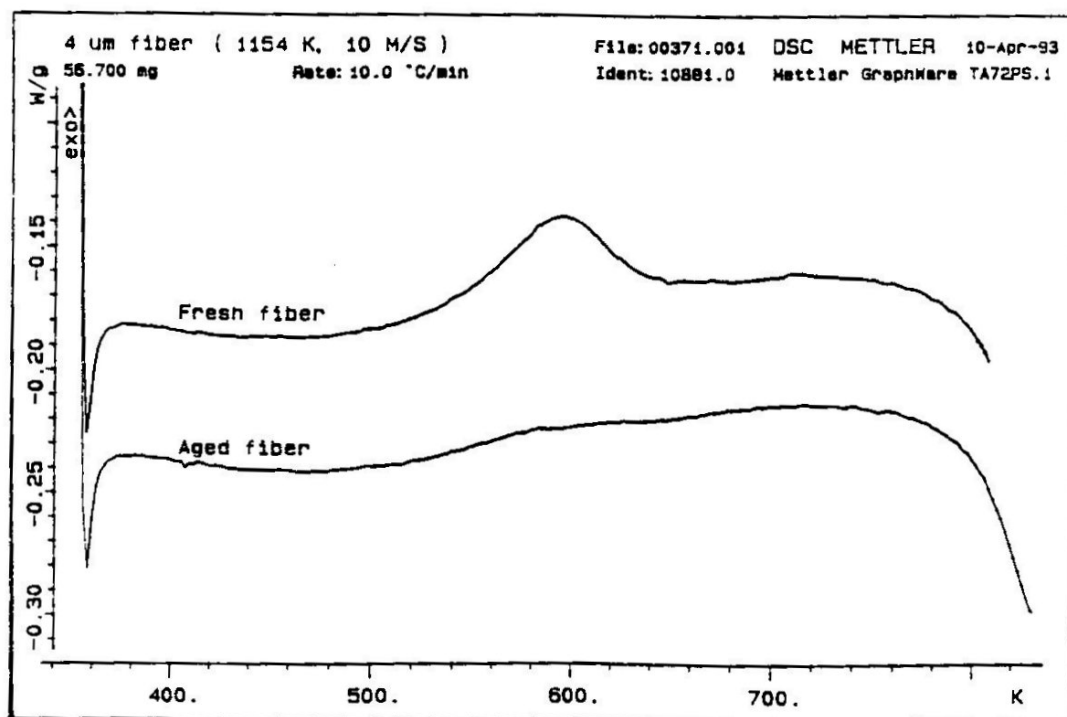


Figure 3.6. Influence of one day of aging at room temperature on the pre - T_g exotherm of drawn silicate glass fiber.³

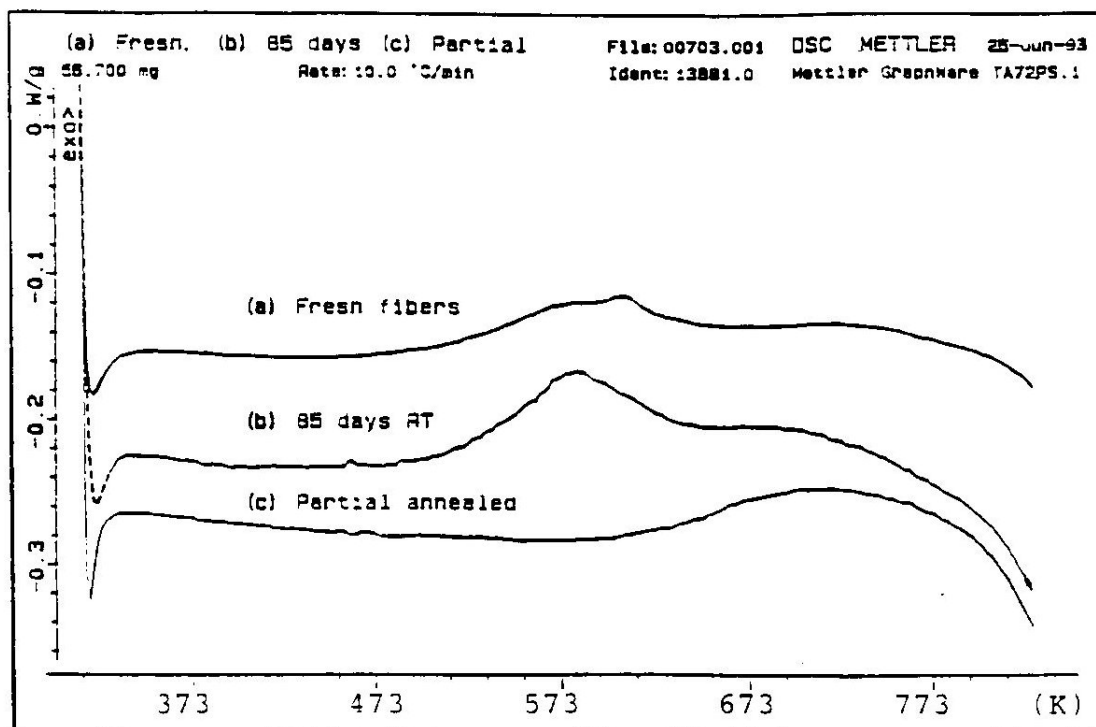


Figure 3.7. Change in pre - T_g exotherm behavior of rapidly drawn silicate glass fibers with aging and partial annealing at 593 K.³

In Figure 3.7 Ho shows the effects of long term aging at room temperature and elevated temperatures on the pre- T_g exotherms behavior of his silicate fibers. Room temperature aging causes the two features at 593 K and 614 K to decrease, while the peak at 581 K is formed and increases. These features were attributed to different structural features. A 15 min anneal eliminates the feature at 581 K completely, but leaves the higher temperature exotherm untouched. The author attributes the initial high energy defects to the partial fracture of the fiber during drawing and suggests a cooperative process in which the high energy defects “heal”, i.e. convert, to lower energy defects. The broad relaxation at higher temperatures appears to be separate from the above process.

3.2.5 Structural Relaxations in the Glass Transition Range^{14,24,45}

Moynihan explained the hysteresis that evolves during the repeated heating and cooling of a glass through the glass transition by separating the process into a number of small temperature steps as shown in Figure 3.8. The dashed stands for both the temperature and the equilibrium property, whereas the solid line represents a measured property. On the first downward step in temperature the relaxation time τ is short enough ($\tau \ll \Delta t$) so the system can equilibrate by the time the second step begins. But as the temperature decreases the relaxation times become greater and the system no longer had time for complete relaxation. This behavior continues to intensify until after the last two steps there is almost no relaxation taking place in the time allowed the system. The system exhibits only a fast change in enthalpy like a frozen in glass does. After the first heating step the relaxation time is still too long to allow relaxation and the glass exhibits only a step change in enthalpy like the frozen glass it still is. After the next heating step, the glass can partially relax towards the equilibrium, but since the enthalpy is higher than the equilibrium enthalpy the glass relaxes “downward” towards equilibrium. At higher temperatures the relaxation times become long enough so that the glass can relax in liquid like fashion towards equilibrium. This

behavior shows itself as the hysteresis depicted in Figure 3.8(2) and Figure 3.9. This type of behavior is prevalent when the heating and cooling rates for the glass are similar. The hysteresis changes slightly when the rates are wildly different as shown in Figure 3.10. When the cooling rate, q_c , is much greater than the rate of reheating q_H , the property p relaxes towards the equilibrium (dashed line) during reheating. This results in a pronounced undershoot, to the point where the slope α_p may be negative for a while and an almost negligible overshoot. If the cooling rate is much lower than the heating rate the property p is so relaxed that there is a significant delay before a reaction can be observed at a high temperature. This results in a negligible undershoot and a pronounced overshoot in the derivative curve.

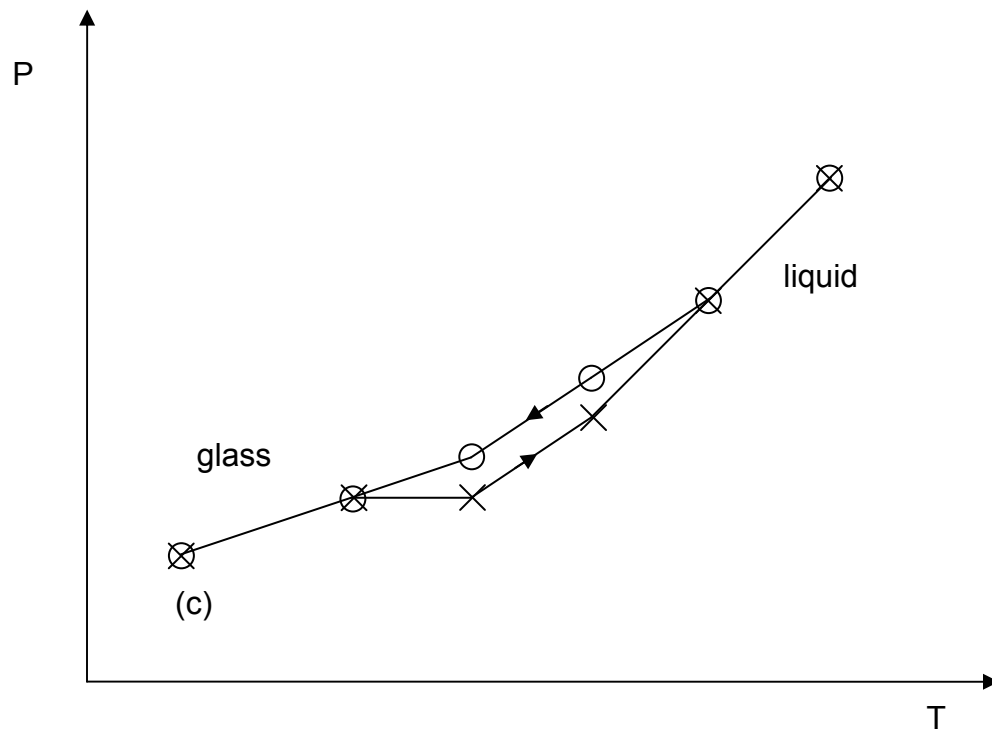
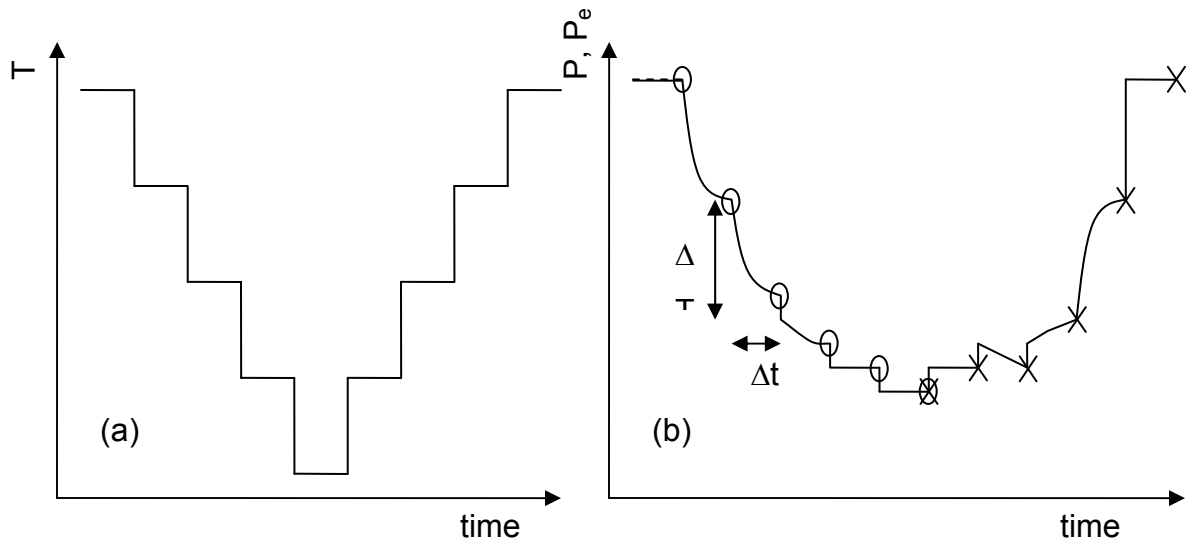


Figure 3.8. Schematic plots of (a) temperature T , (b) equilibrium property P_e and experimentally measured property P with time and (c) P vs T during the stepwise cooling and reheating through the glass transition region, After Moynihan.²⁴

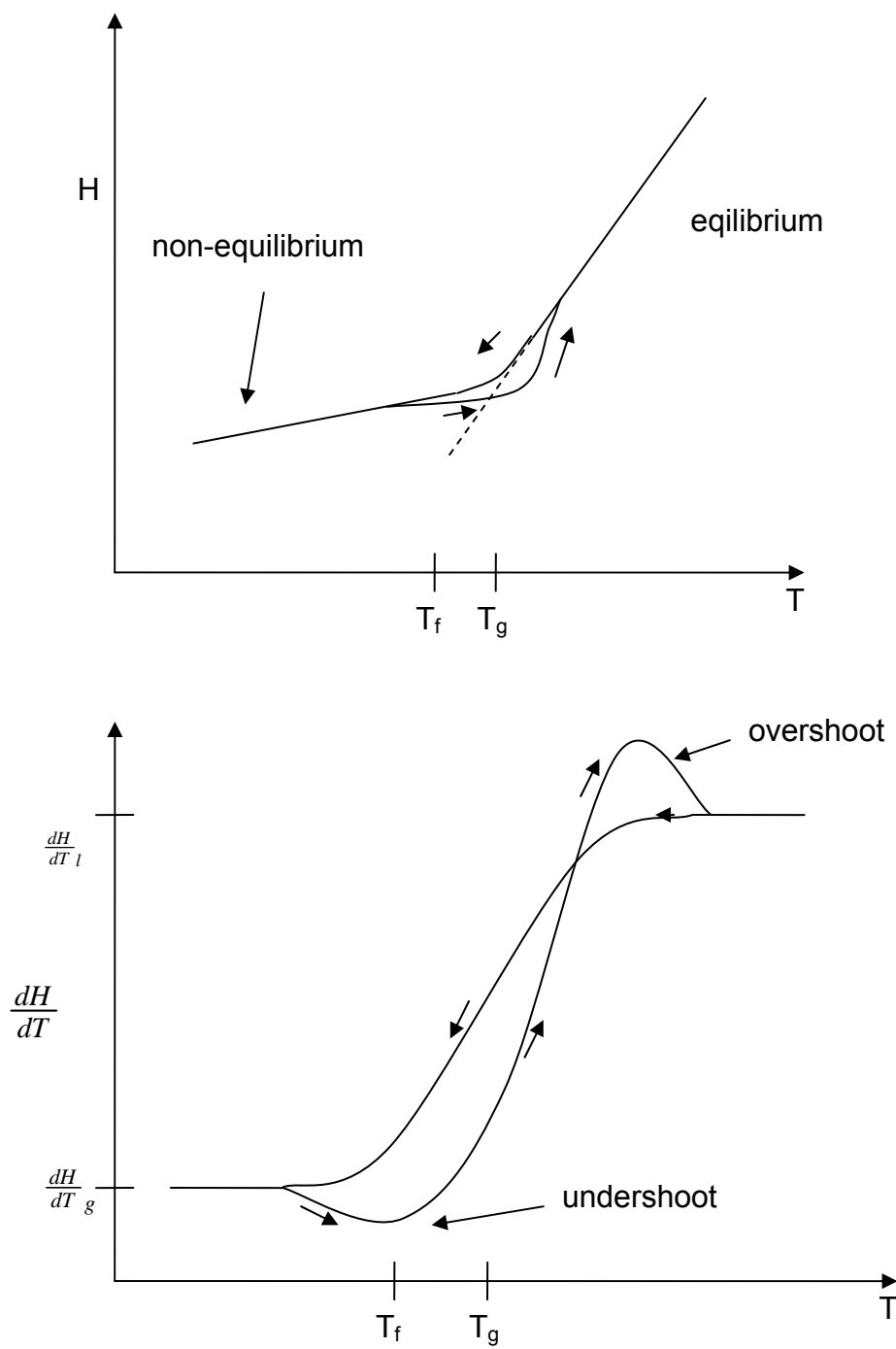


Figure 3.9. Hysteresis in enthalpy H and derivative α_H during cooling and reheating. After Scherer.¹⁴

3.2.6 Previous work

A large amount of work has been done on the behavior of various glass fiber forming systems. A quick overview over some of the work done on silicate glass fibers^{3,12,34,35} and chalcogenide glass fibers^{31,37,40,43-45} will be summarized in the following, as the most data is available on these systems.

Some of the earlier systematic work on structural relaxation in silicate glass fibers was done by Huang^{34,35} in his Ph.D. work. The authors examined NBS-710 silicate glass. Fibers were drawn from the glass using a bushing method to diameters from 9 – 12 μm diameter. DSC traces were run on the fibers and bulk samples at various heating rates. The fiber samples exhibit relaxation exotherms starting at ca. 400 K below the glass transition, which is at much lower temperatures than bulk samples. The authors also tried to fit the DSC data using a fitting model, based on a combination of the Tool – Narayanaswamy, Kohlrausch – William – Watts and Adam – Gibbs model using five fitting parameters. They were able to successfully fit the traces of bulk samples but the model did not prove a good fit for rapidly cooled samples and fibers.

Later Ho³ examined the effect of drawing conditions on shear thinning phenomena in silicate glass fibers. He was able to draw several conclusions from his work as shown in Figure 3.11. The pre – T_g exotherms increases with drawing speed up to the point where the shear thinning region is reached and then starts to decrease. He attributed the decrease in the exotherm area to structural changes in the glass. He was able to show that some fibers are starting to relax at a temperature 400 K below their glass transition temperature (800 K). The fibers Ho examined exhibit two very distinct exotherm peaks on reheating, indicating two very specific relaxation mechanisms for the release of stored energy in the fiber. His study of the fictive temperature of the fibers shows that effects induced by cooling are not sufficient to describe the relaxation behavior. Further examinations of the fibers via Raman and EPR spectroscopy both suggest the breakdown of the three – dimensional structure of the glass network at extreme drawing conditions. Ho suggests that the existence of a

number of different defect centers suggest the presence of low molecular weight species in the fiber. And he attributes the existence of the pre – T_g relaxation peaks to the presence of a specific defect similar in behavior to an oxygen hole.

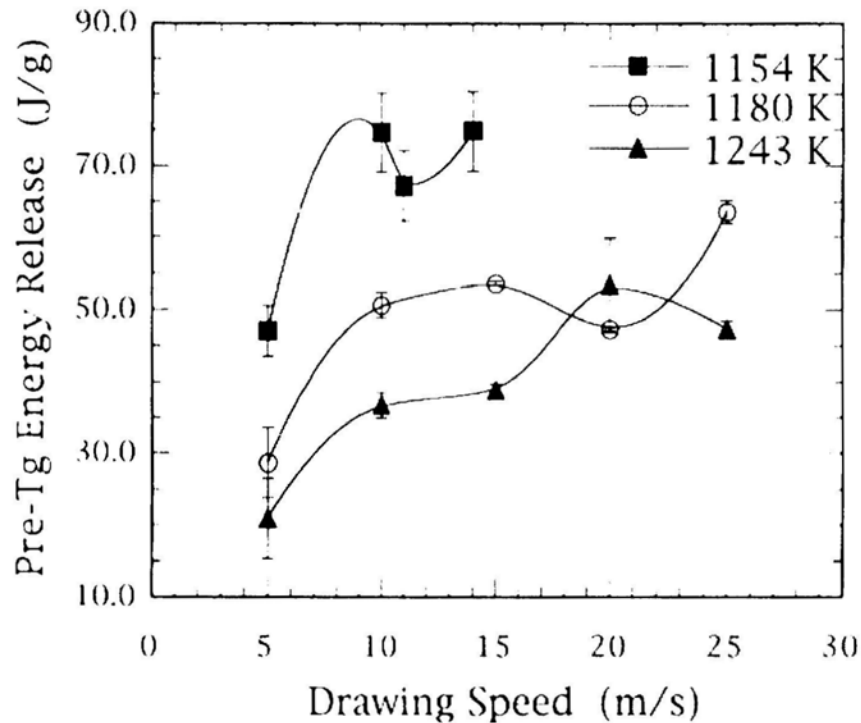


Figure 3.10. Pre – T_g exotherm as a function of draw speed and temperature. After Ho.³

In later work Zheng¹² examined silica glass fibers with the compositions $25 \text{ Na}_2\text{O} - x \text{ Al}_2\text{O}_3 - (75-x) \text{ SiO}_2$ and $25 \text{ Na}_2\text{O} - x \text{ B}_2\text{O}_3 - (75-x) \text{ SiO}_2$ using DRIFTS and NMR spectroscopy in addition to thermal measurements. He was able to show a maximum in the pre – T_g exotherm as drawing speed increases. He shows the use of this maximum in the characterization of the onset of shear thinning behavior in the melt during drawing. At a constant drawing temperature shear thinning may occur as draw rate is increased. At a constant draw rate, shear thinning may be induced by lowering the temperature. The fictive temperature of his fibers shows a similar behavior to that of the total exotherm, which in turn follows a similar trend than the pre – T_g exotherm. Zheng draws two conclusions from this. First, a high cooling rate does not necessarily mean a

high fictive temperature, which indicates that the fictive temperature alone is not sufficient to describe the structure of a glass completely. And second, the large structural changes caused by shear thinning cannot be relaxed at temperatures close to T_g .

Shen⁴⁶ examined the influence of drawing parameters on pre – T_g exotherms of glass fibers with the composition 25 Na₂O – 2.5 Al₂O₃ – 72.5 SiO₂. Fibers were drawn using external pressure from a gas to achieve a constant diameter and using drawing speeds of 1.3 – 15.9 m/s. The data for the pre – T_g exotherms shows an increase of the exotherm with drawing speed. This increase is only sustained up to a drawing speed of 8 m/s and decreases after this maximum follows. This decrease implies a decrease in fictive temperature that the author terms abnormal. The author attributes this behavior to the onset of shear thinning. DRIFTS experiments carried out by the author showed a new structural band appearing at draw speeds higher than 8 m/s that remained even after relaxation. According to the author this indicates the formation of new fiber structural arrangements at high drawing speeds that cannot be relaxed through normal annealing in the glass transition range.

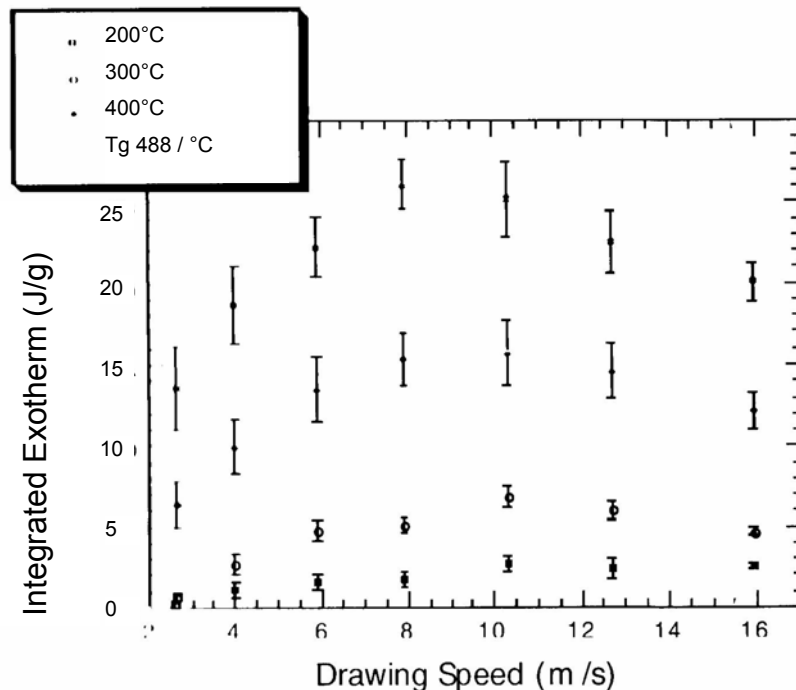


Figure 3.11. Integrated exotherm for glass fibers up to the indicated temperature vs draw speed. After Shen.⁴⁷

Cerqua – Richardson³⁷ examined arsenic selenide glass fibers with compositions containing 5 – 50 mol% arsenic. DSC measurements revealed a maximum in the pre – T_g exotherms of the glass fibers at an intermediate draw speed of 0.6 m/sec. The exotherm area decreases after this point, which the author relates to the onset of shear thinning behavior in the melt. The glass transition temperature in contrast shows a decrease up to 1 m/s draw speed and then a sharp increase. This behavior is consistent with the behavior of the tensile strength of the glass fibers, which show an increase in strength up until 1 m/s draw speed and then a decrease to levels below the original bulk strength of the glass. The author is able to relate this behavior to defects examined via EPR. Two different factors affecting the defect structure are responsible for the pre – T_g exotherm and strength behavior, according to the author. First the release of stretched bonds and bond angles in non – equilibrium configurations contributes to the presence of a pre – T_g exotherm and second the “healing” (relaxation) of defects or rearrangement of high energy defects into more stable, lower energy configurations. The author notes, however, that there may be other processes occurring, because there are samples in which even an isothermal hold above T_g does not remove all pre – T_g exotherm peaks in the glass. Richardson also shows that stress can inhibit relaxation behavior and retard aging in fibers, by comparing samples that were aged while wrapped around a cylindrical object to those aged left hanging freely under their own weight. The wrapped samples show that one reheating cycle is not sufficient to remove all their pre – T_g exotherm. There also appears a low temperature exotherm in the wrapped fibers after the first reheat, implying that there is a fast process in the relaxation that does not involve structural rearrangements in the bulk of the material.

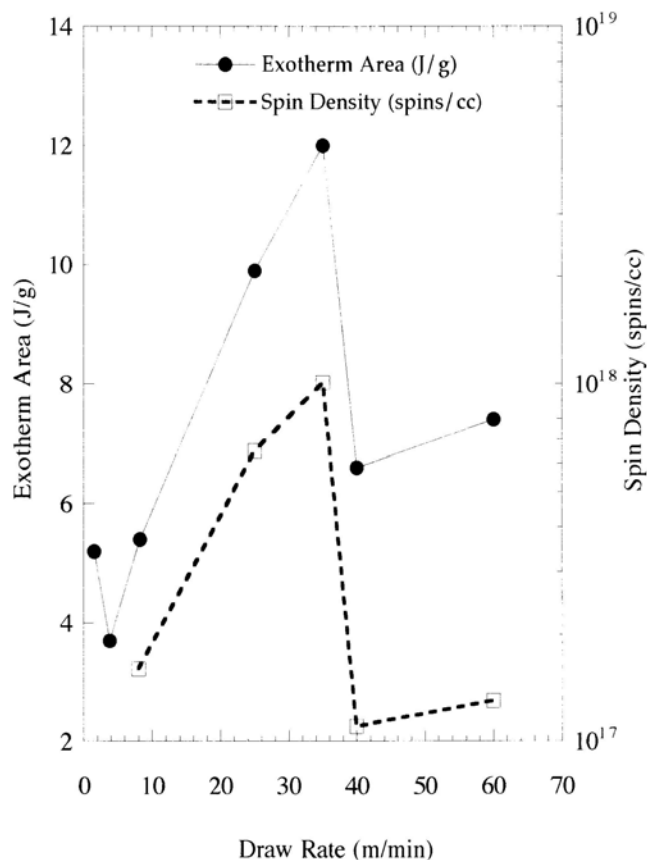


Figure 3.12. Dependence of exotherm area spin density on draw rate. After Cerqua – Richardson.³⁷

King⁴³ examined As_2Se_3 glass fibers in his work using NQR, neutron scattering and DSC measurements to elucidate relaxation behavior and propose a structural model for relaxations below the glass transition. He was able to draw several conclusions from his work. King states that under increasingly extreme fiber drawing conditions, the amount of defects grows in the glass structure. Once a critical drawing speed is reached he observes shear thinning behavior in his glass. His neutron scattering and NQR experiments show defects that cannot be observed in either the bulk glass or fibers drawn under less extreme conditions. He explains this behavior with a model of the glass structure in which the drawing process introduces strain and orientation into the structure of the fiber. As the drawing speeds exceeds the critical point, the stress induced into

the glass structure becomes large enough to actually rupture bonds and break the ring structures the arsenic selenide glasses possess. The appearance of new structural arrangements under neutron scattering and NQR for fibers drawn under shear thinning conditions firms up his suppositions.

As shown in Figure 3.14 the critical drawing speed for shear thinning is roughly 90 m/s determined by the maximum in the pre – T_g exotherm. The complex nature of the pre – T_g exotherm data also suggests that there are number of processes involved in the relaxation of the fibers. King proposes the following model for the data. In region I the stress induced in the glass structure is not high enough to cause many broken bonds and other high energy defects. The major contribution to stored energy is frozen – in strain. After the onset of shear thinning at the critical point A bonds will start to break in the glass structure, raising the amount of stored energy significantly. The defect concentration in region II is initially low, which leads to isolated defects that are not able to heal cooperatively. After critical point B the defect concentration is high enough to cause the structure to assume an energetically lower form as rings. As drawing speed increases in region III more and more of the damaged regions are able to relax due to a lower effective viscosity in them. The low value of the stored energy at point C implies that the frozen – in bond length and angle distortions from region I are eliminated, because more and more of the structure undergoes the bond rupture and reformation process. In region IV the stored energy increases again as the reformation process cannot keep pace with the increasing damage inflicted by the extreme drawing speeds.

Figure 3.15 shows short term relaxation of arsenic selenide glass fibers. This behavior is also complex to interpret. The greatest initial fictive temperature was shown by sample C, which also showed the greatest initial decrease in fictive temperature with ageing. These two observations are related due to the fact that the driving force for relaxation is the distance from equilibrium. Sample C also shows a large memory effect where the fictive temperature is increasing again with ageing. The greater relaxation of sample B to sample A may be due to the larger frozen in strain in sample B. Samples C,D, E, F and G were drawn

under shear thinning conditions. Samples A and E show the lowest relaxations, which is consistent with them smallest pre - T_g exotherms.

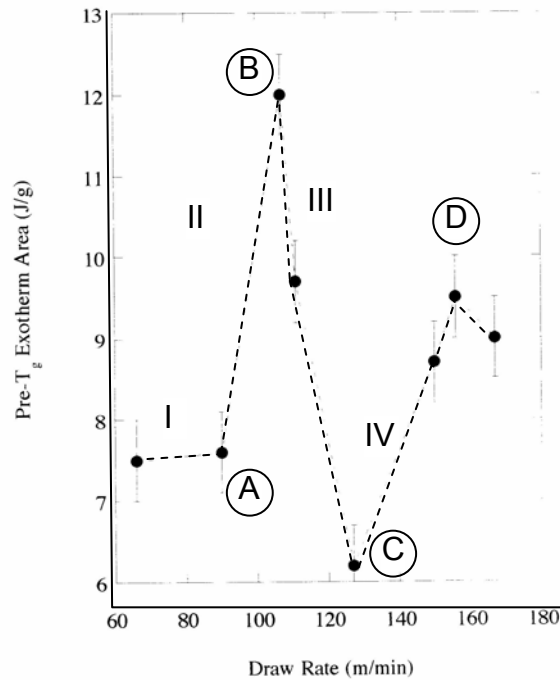


Figure 3.13. Pre - T_g exotherm area measured by DSC versus the fiber drawing rate. Lines are drawn as a guide to the eye. After King.⁴³

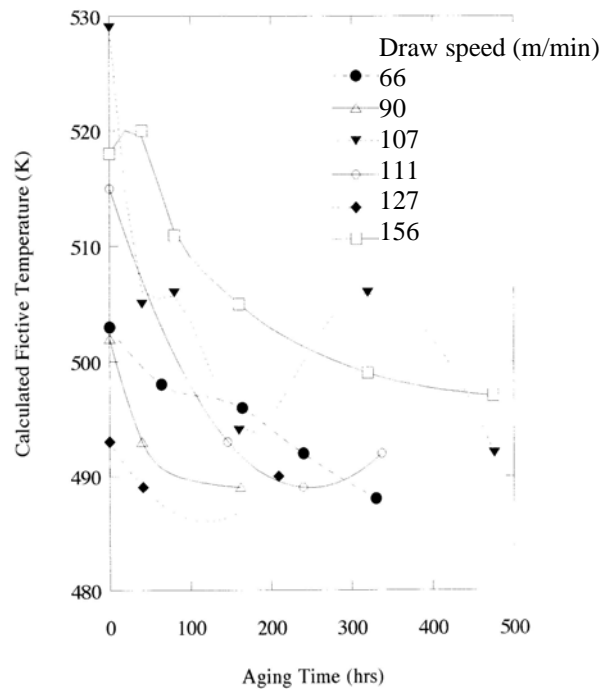


Figure 3.14. Fictive temperature calculated from measured exotherm area versus ageing time. Lines are drawn to guide the eye. After King.⁴³

3.3 Experimental Procedure

3.3.1 Glass Fiber Drawing

The fiber drawing was conducted on a bushing fiber drawing tower constructed by a former doctoral student, Chung Tsair Ho,³ as part of his Ph.D. thesis.³³ The machine is displayed in Figure 3.16. A platinum – 20% rhodium bushing was held by water – cooled copper clamps, which were connected to a transformer^e that supplied enough power to resistively heat the bushing up to 1500°C.

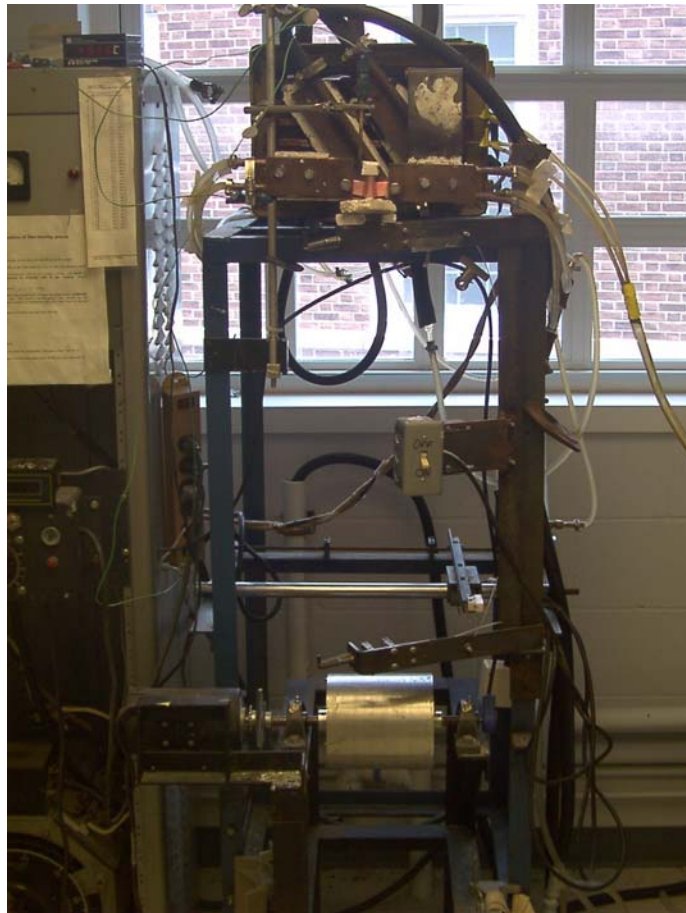


Figure 3.15. Fiber drawing tower.

^e ACME Transformer Model T-15073-8

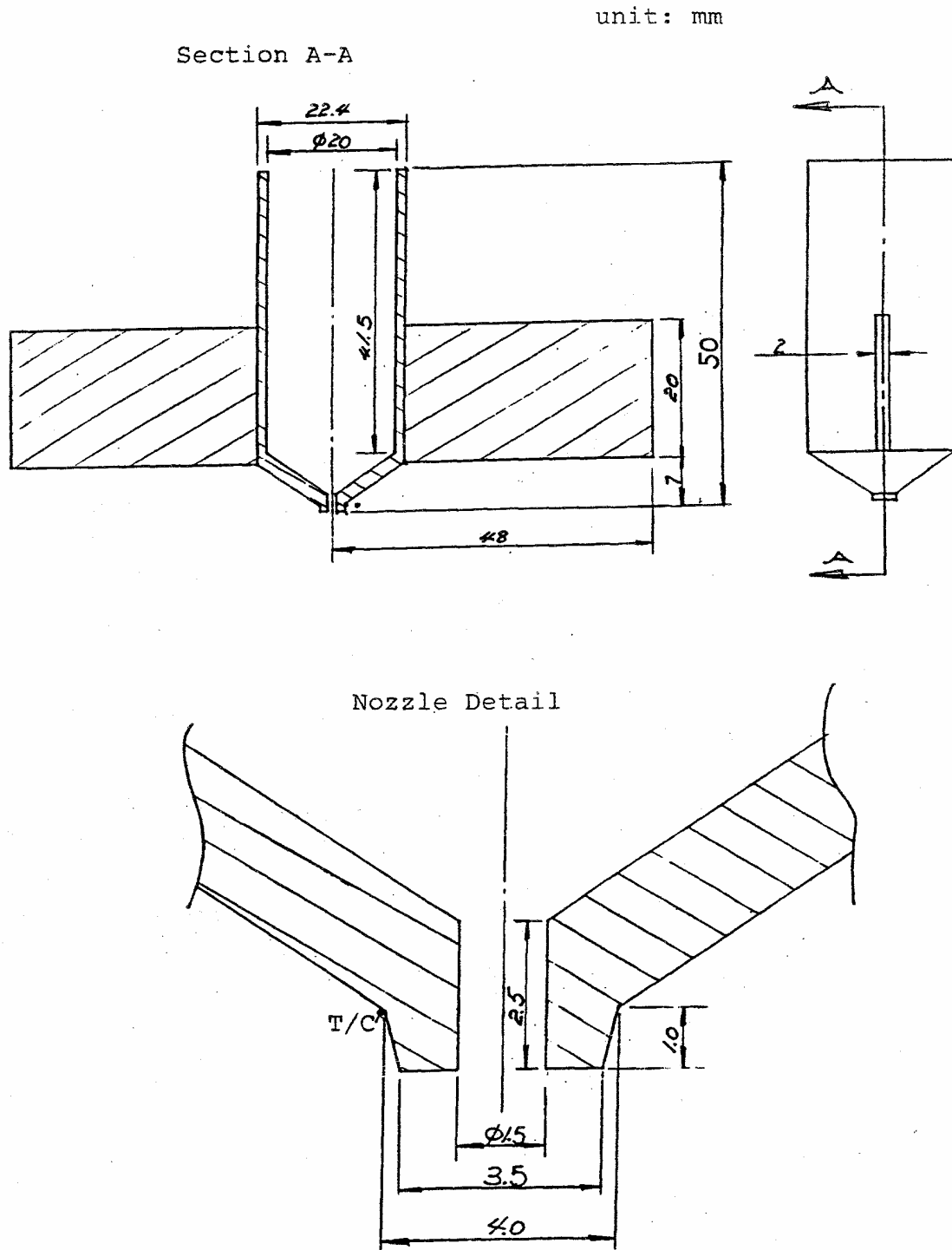


Figure 3.16. Design of the fiber drawing bushing. After Ho.³

The dimensions of the bushing can be seen in Figure 3.17. The bushing tapers at the bottom, where it contains a hole of 1.5 mm diameter.

Thermocouples were placed against the bushing to measure the temperature. For temperature measurement a thermocouple was placed into the melt in the bushing itself. The arrangement is displayed in Figure 3.18. Care was taken that the thermocouple rest at the bend of the bushing to increase repeatability of the experiments.

The thermocouple was a S – type thermocouples consisting of platinum and platinum / 10% rhodium wires. S type thermocouples are good for a temperature range between 0°C and 1450°C.

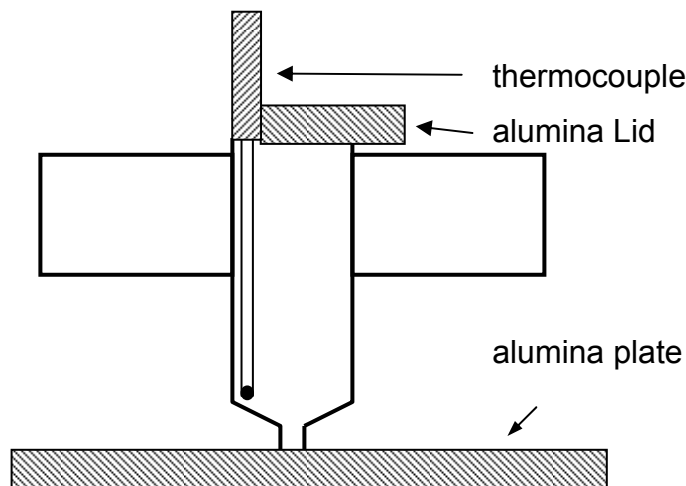


Figure 3.17. Thermocouple placement in the bushing.

This arrangement was necessary because the alumina plate cooled the nozzle of the bushing and prevented accurate temperature measurements at the nozzle.

A controller connected to the thermocouple controlled the temperature of the bushing^f. This controller was manually regulated with respect to output. At the settings used approximately 55% of the maximum power output produced a temperature of ca. 1300°C.

^f Eurotherm 818 Controller

The glass fibers were wound onto an aluminum drum below the orifice of the bushing. The drum had a diameter of 15.3 cm and was turned by a motor⁹ with electronic controls. The motor can turn the drum fast enough to reach drawing speeds of roughly 15 m/sec.

The arm on the machine is used to obtain virgin glass fiber samples for tensile testing, but was not used in these experiments, since virgin glass fibers were not required.

3.3.2 Fiber Drawing Parameters

The main parameter that determines the usefulness of the glass fibers in reinforcement is their diameter. The diameter of a glass fiber drawn in a bushing apparatus is, according to Thomas⁹ and Loewenstein,⁴ mainly influenced by the diameter of the nozzle of the bushing, the composition of the glass, the temperature of the glass, the drawing speed, the vertical depth of the glass column above the nozzle and the design of the crucible.

The bushing was the same for all experiments. So nozzle diameter, and design of the bushing did not change. Due to the volatility of the glass components, a lid had to be kept on the bushing during the whole course of the experiments. This prevented the maintenance of a constant level of glass in the bushing. The lid that was used was a 1 cm thick block of alumina.

The two parameters that were varied for each of the three glasses used in the course of the experiments were temperature and drawing speed.

The procedure to draw the glass fibers was as follows. First the bushing was filled with crushed glass frit until full. The bushing was then placed in the drawing tower, the thermocouple was brought into contact with the bushing, and the alumina plate was placed under the bushing. The temperature was raised to about 800°C. More glass frit was added until the level of molten glass was within 5 mm of the top of the bushing. Then the alumina lid was placed on the bushing,

⁹ Balder AP7402

while care was taken not to disturb thermocouple 1. The temperature was maintained at 800°C for ca. 2 min in order to homogenize the glass. After this the temperature was lowered to the draw temperature and the motor for the drum was started and allowed to equilibrate for at least one minute, after regulating the speed to the desired drawing speed. Then the temperature was dropped until the draw temperature was reached, at which point the alumina plate was removed. The temperature was then manually regulated to the desired drawing temperature maintaining a precision of $\pm 1^\circ\text{C}$ by manual adjustments of the controller.

At the drawing temperatures the glass was fluid enough to drip from the nozzle on its own. This necessitated a speedy start of the drawing process, before too much glass could escape the bushing. The glass drop at the nozzle was caught with a pair of tweezers and was wound onto the rotating drum by wrapping the fiber around the drum and pulling tight. Then tension was quickly applied by using a small diameter wire that was mounted on a mobile arm. The drawing continued until the bushing ran out of glass.

After drawing the bushing was either lowered to room temperature to be cleaned in boiling water or topped off with glass frit to start a new drawing process.

3.3.3 Diameter Measurement of Glass Fibers

The diameter of the glass fibers was measured using a light microscope^h with attached CCD cameraⁱ. This allowed images to be taken of a calibration standard consisting of an etched Silicon wafer. Image processing software^j was calibrated by measuring known distances of the standard, which then allowed measurements on images taken with the same magnification. The diameter

^h Leitz Laborlux 11 POL

ⁱ SPOT Insight 2 Megapixels

^j Image Pro 3.2

measurements were performed on at least 15 fiber fragments and then averaged.

3.3.4 Heat Capacity Measurements

Glass fibers were cut to approximately 3 mm in length and DSC samples were prepared. 20 mg of cut fiber were mixed with 20 mg of alumina powder and filled into a hermetically sealed DSC pan (see Figure 3.19). A reference pan was prepared containing only 20 mg of alumina powder. The alumina powder was used to prevent thermal contact problems that could falsify the measurements. Some experiments were conducted using an empty reference pan.

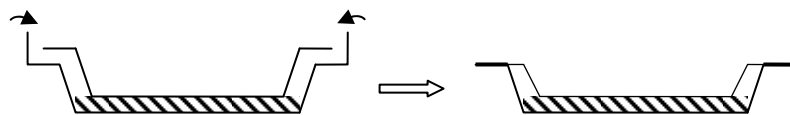


Figure 3.18. Cold welded hermetic DSC pan

The heat capacities of the samples were measured using either the ASTM standard method of calibrating the DSC cell with a known sapphire standard at a heating rate of 20 K/min or using a modulated DSC measurement at a heating rate of 3 K/min. Both measurement methods could be shown to give equivalent results. Heat capacities were measured from 100°C to 500°C in 50°C steps. The exact methodology is described in chapter 2.

Of each drawing condition three samples were prepared and each sample was run between three and five times. The displayed heat capacities are averaged over all samples and all runs at a given drawing condition.

3.3.5 Pre – T_g Exotherm Measurement

The pre- T_g exotherms were measured using the same type of sample as in the heat capacity measurements. For some samples the heat capacity was determined after the sample had run through the pre- - T_g measurement.

The sample was heated at a rate of 10 K/min to a temperature of 550°C and cooled at the same speed to room temperature. This cycle was repeated three to five times. In order to determine the pre – T_g exotherms the last run of a given sample was used as a baseline and subtracted from the first run to show the pre – T_g exotherm. The area under the curve was then integrated to show the amount of energy released. Figure 3.20 shows this schematically. However, due to the slow crystallization of the glass fibers, the height of the glass transition changes, shrinking. This distorts the exotherm curve, but a horizontal integration coincides very well ($\pm 2^\circ\text{C}$) with the inflection point of the glass transition. Therefore a cutoff of the exotherm at the glass transition temperature has not been performed. The pre – T_g exotherms shown are averaged over all three samples of a given drawing condition.

The onset of the pre – T_g exotherm was determined using the intercept method. Due to the decreasing height of the glass transition peak it was actually not necessary to terminate the integration at T_g . The decreasing peak height allowed the full horizontal integral to be used to calculate the pre – T_g exotherm area with minimal error. Figure 3.20 shows a typical example. If the integration is terminated at T_g exactly the measured integral is equal to 19.23 J/g, if the integration is allowed to terminate naturally at the limit presented by the decreased height of the glass transition the integral measures to 19.28 J/g. The error is 0.25 %, which is negligible.

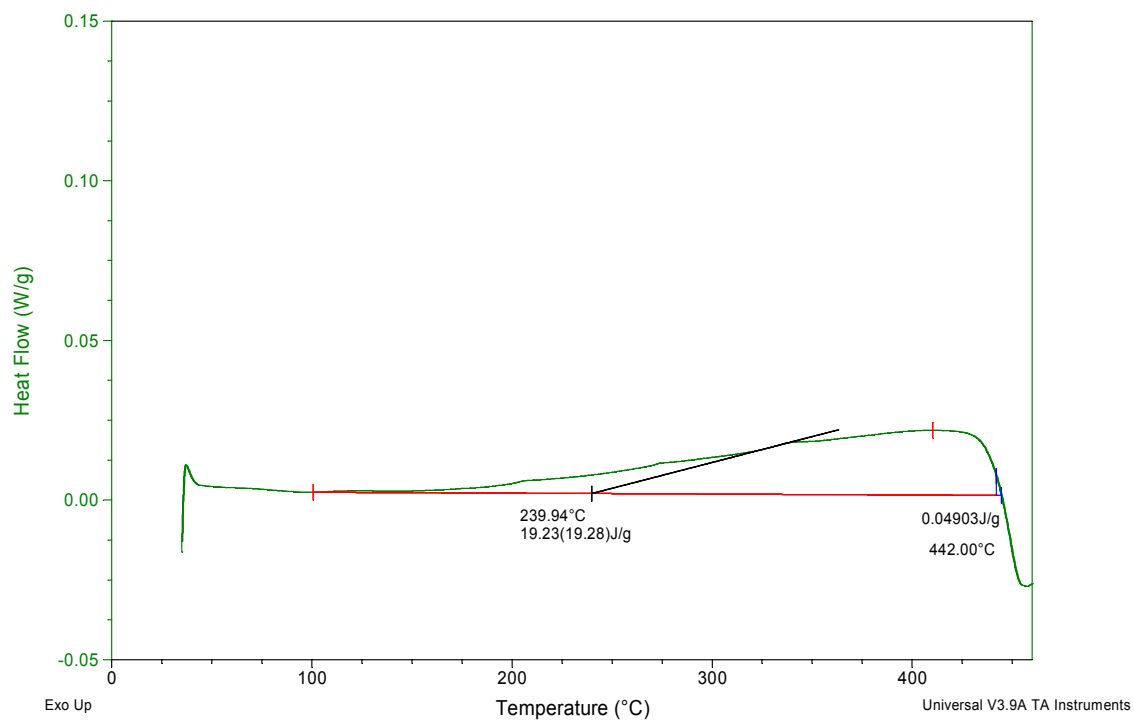
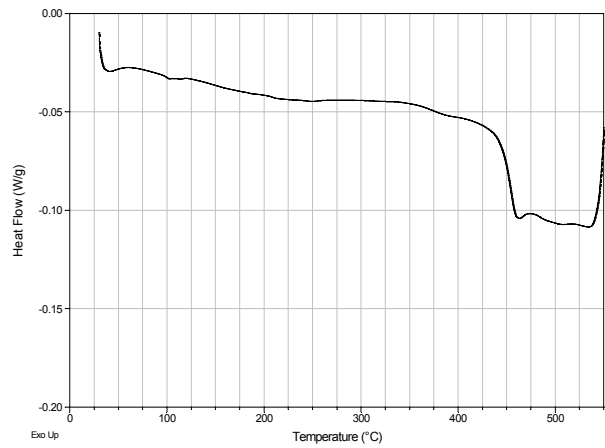
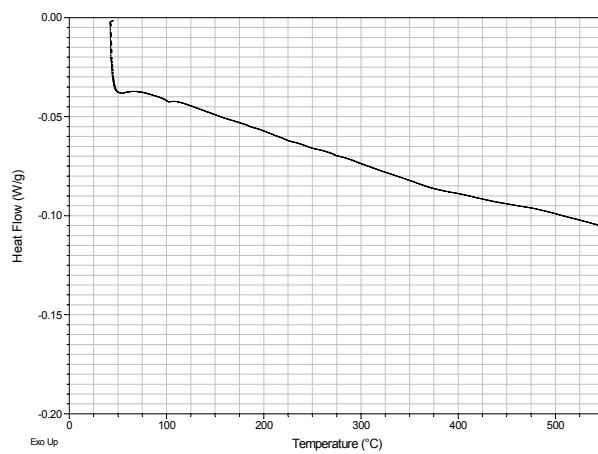


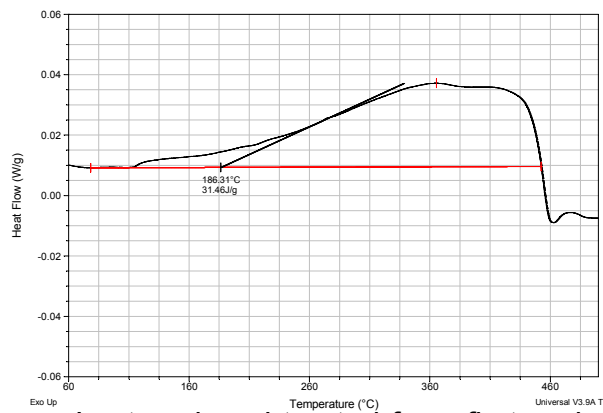
Figure 3.19. Error in pre - T_g exotherm calculations by not terminating integration at T_g



First cycle



Last cycle



Last cycle subtracted from first and integrated

Figure 3.20. Schematic representation of the determination of pre- T_g areas

3.3.6 Calculation of T_f

The method used to calculate fictive temperatures in this work is the same as that suggested by Moynihan et al.²⁶ in their paper. The authors observed a dependency of the fictive temperature on cooling rate. This is obvious when one realizes that cooling rate determines the structure of a glass and that the fictive temperature is closely related to structure. The authors also noted that for DSC work the measurement of the cooling rate, which can be difficult over a wide temperature range is not necessary. When a glass is cooled through the transition region, it acquires a fictive temperature T'_f . But during reheating the heating rate may be chosen in order to maximize the accuracy of the DSC measurements according to the following rationale.

Moynihan et al.²⁶ stated that “when p is a macroscopic property of a vitreous system, the fictive temperature, T_f , in a given state is defined as the temperature at which the equilibrium liquid has a relaxational value of p the same as that of the system in that state.” If a glass has been heated or cooled through the glass transition region, the value of T_f at a temperature T' may be obtained using the following formula:

$$p(T') = p_e(T_f) - \int_{T'}^{T_f} \left(\frac{\partial p}{\partial T} \right)_g dT \quad (3.17)$$

The subscript g refers to the glassy state and the subscript e to the equilibrium state. The temperature coefficient of the system is defined as

$$\left. \frac{dT_f}{dT} \right|_{T'} = \frac{\left[\left(\frac{dp}{dT} \right) - \left(\frac{\partial p}{\partial T} \right)_g \right]_{T'}}{\left[\left(\frac{\partial p}{\partial T} \right)_e - \left(\frac{\partial p}{\partial T} \right)_g \right]_{T_f}} \quad (3.18)$$

When using a DSC trace to determine the value of T_f the integrated form of equation 3.18 is much more useful.

$$\int_{T^*}^{T'_f} (C_{pe} - C_{pg}) dT_f = \int_{T^*}^{T'} (C_p - C_{pg}) dT \quad (3.19)$$

This equation allows one to calculate the value of T_f from heat capacity data obtained on any DSC instrument by matching the areas represented by either side of the equation. T^* represents a temperature well above the transition region and C_{pe} and T' represent equilibrium heat capacity and a temperature well below the transition region. This is shown schematically in Figure 3.22.

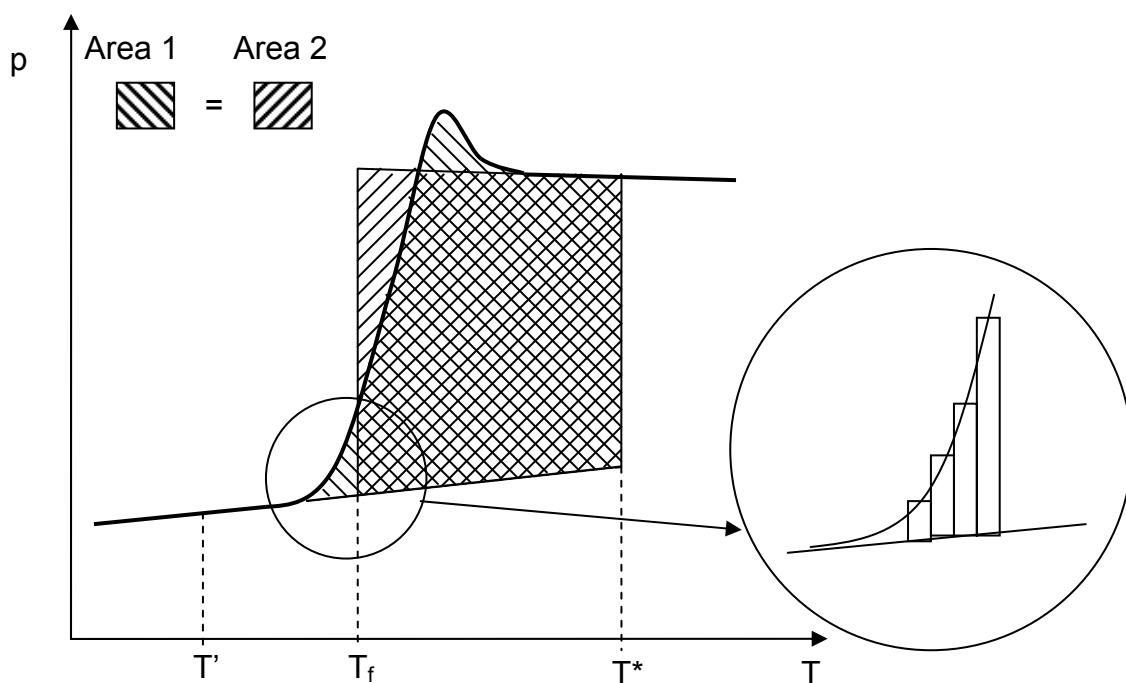


Figure 3.21. Area matching from Moynihan^{26,28} and column integration from Hall.⁴⁷

The actual integration was performed in a spreadsheet program using a column summation algorithm. Small temperature steps are defined and the height of a column reaching the average height of the curve at the beginning and end of the temperature step is calculated. The areas of these columns are all calculated and summed up to determine the area. A movable temperature indicator T_f is used to minimize the difference between the two areas. The minimum of this value is taken as the fictive temperature. Figure 3.23 shows the output of the program. Care has been taken to calculate the positive and

negative contributions to Area 1.

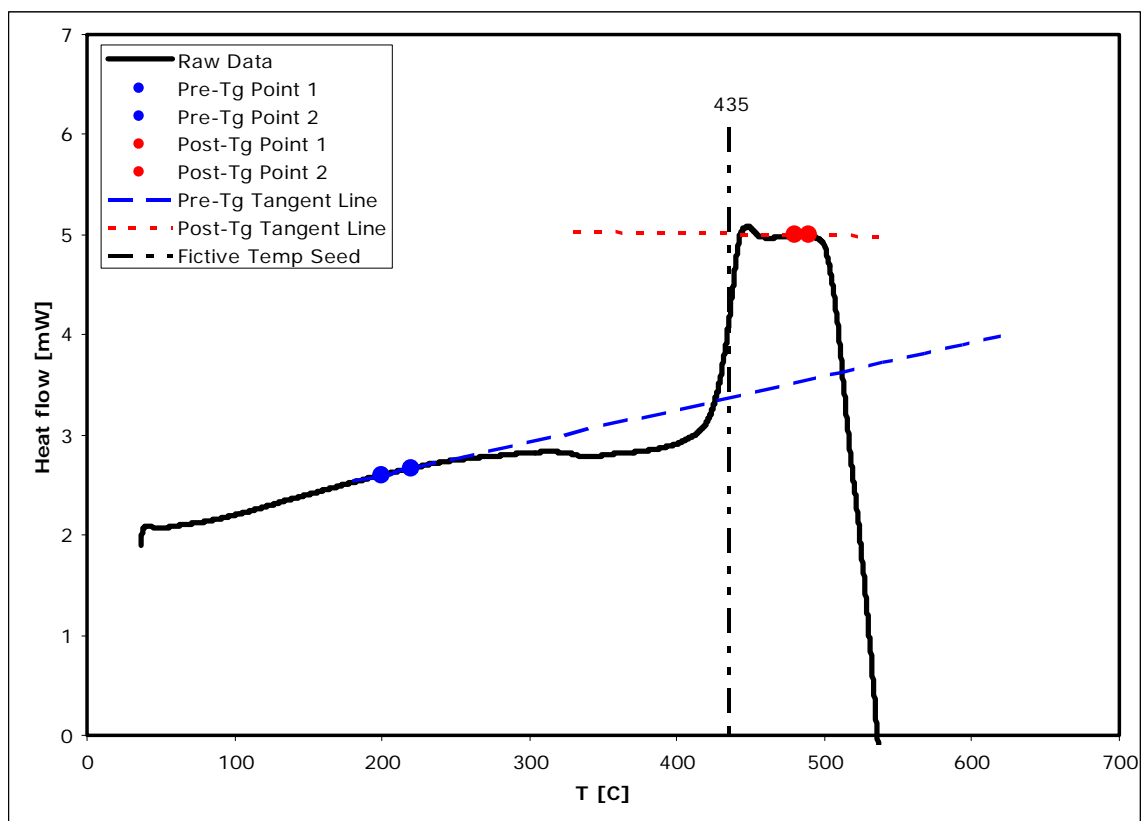


Figure 3.22. Output of spreadsheet program.⁴⁷

3.4 Results

Note:

In the graphs the x – values of some data points have been altered slightly, by adding or subtracting a small amount in the x – value of data points. For example if four data points are being displayed for a given x – coordinate of e.g. 6 m/s for each point, for purposes of readability the graph will actually display the x – coordinates of 5.8, 5.9, 6.0 and 6.1 m/s for the data points. This has been done for purposes of clarity and readability of the graphs themselves, it does not imply a change in the actual values. For the exact value the reader is referred to the always included tables.

3.4.1 Fiber Diameters

The fiber diameters were measured as described above. Each data point represents at least 15 measurements. The results are displayed in Figure 3.24.

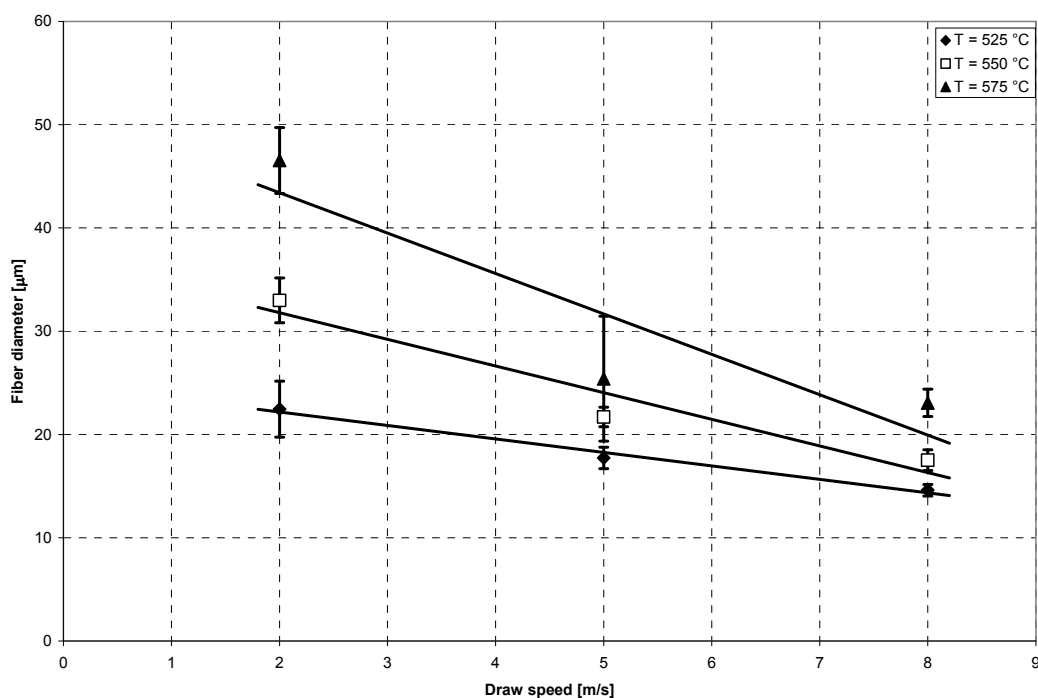


Figure 3.23. Diameters of fibers vs draw speed (The lines are linear fits).

As can be seen from the graph the diameters of the fibers decrease linearly with drawing speed and increase with drawing temperature.

3.4.2 Glass Transition Temperatures

Glass transition temperatures were calculated for all fiber samples. The results are shown in Table 3.I. All data points were obtained from at least three samples each of which was subjected to at least three cycles. Figure 3.25 to Figure 3.27 show this information graphically. Please note that the values of the data points along the x – axis of the graphs have been spread for clarity. This does not imply a change in draw speed.

Table 3.I: Glass Transition Temperatures of all Fiber Samples

T [°C]	S [m/s]	T _g [°C]	
Bulk	-	446	± 3
525	1	442	± 8
525	2	440	± 1
525	3.5	439	± 7
525	6	449	± 4
550	1	437	± 7
550	2	445	± 7
550	3.5	447	± 5
550	5	445	± 8
550	6.5	446	± 5
550	8	445	± 7
550	9.5	421	± 1
575	2	440	± 8
575	4	423	± 3
575	5	442	± 2
575	6	433	± 6
575	8	439	± 6

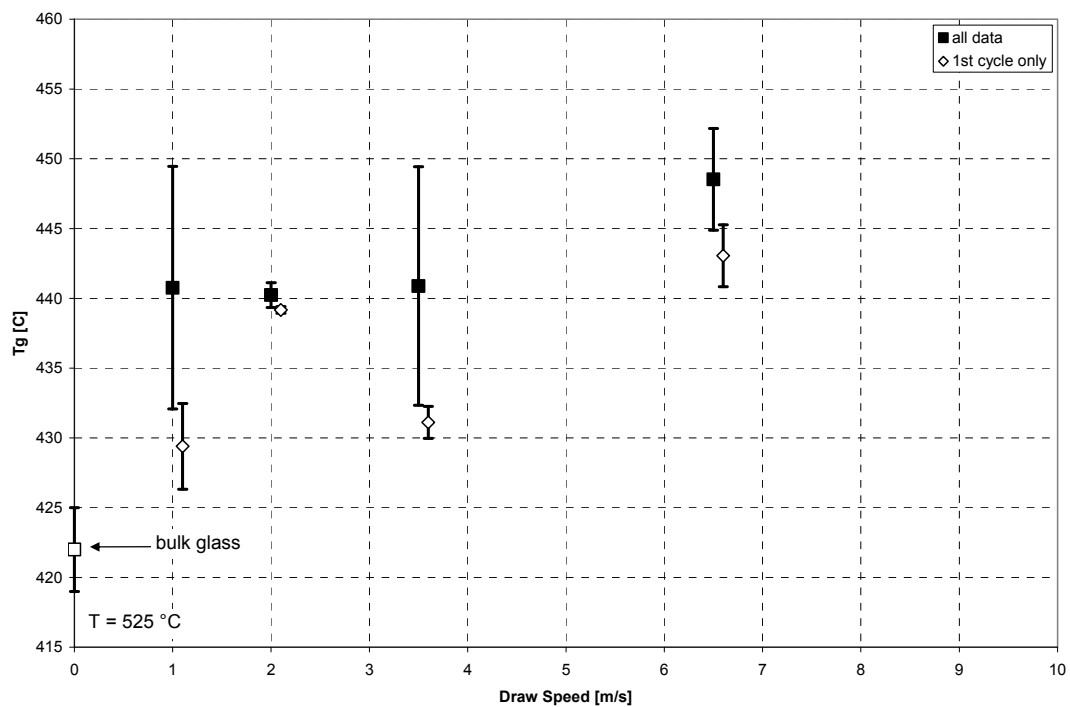


Figure 3.24. Glass transition temperatures for fibers drawn at 525°C vs drawing speed.

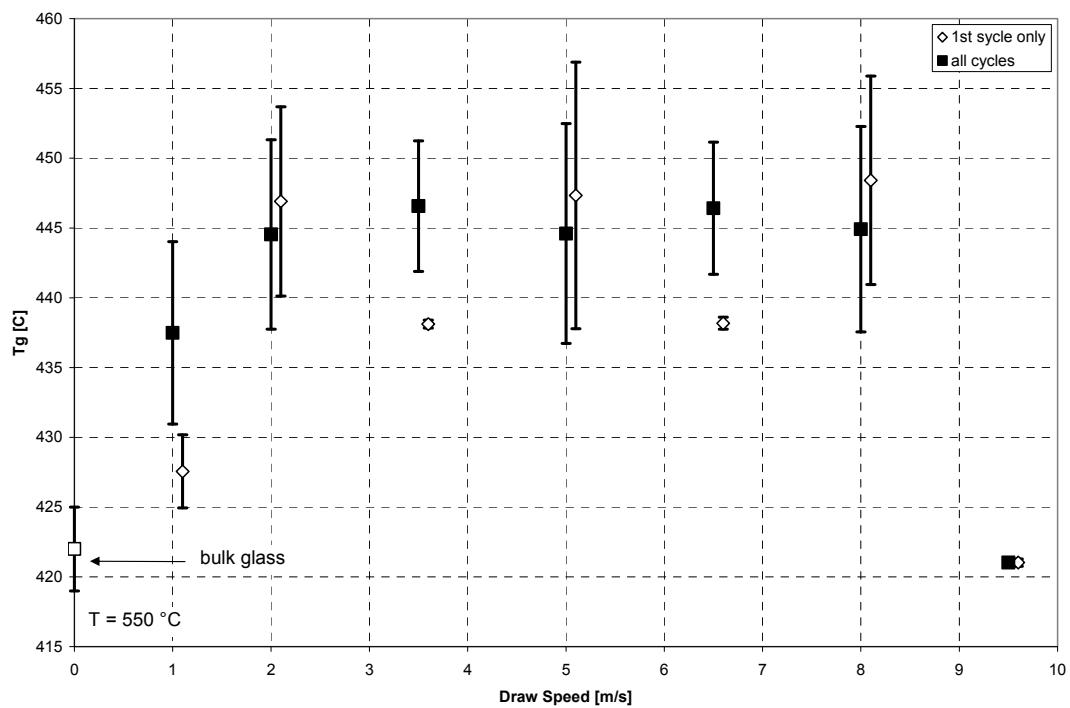


Figure 3.25. Glass transition temperatures for fibers drawn at 550°C vs drawing speed.

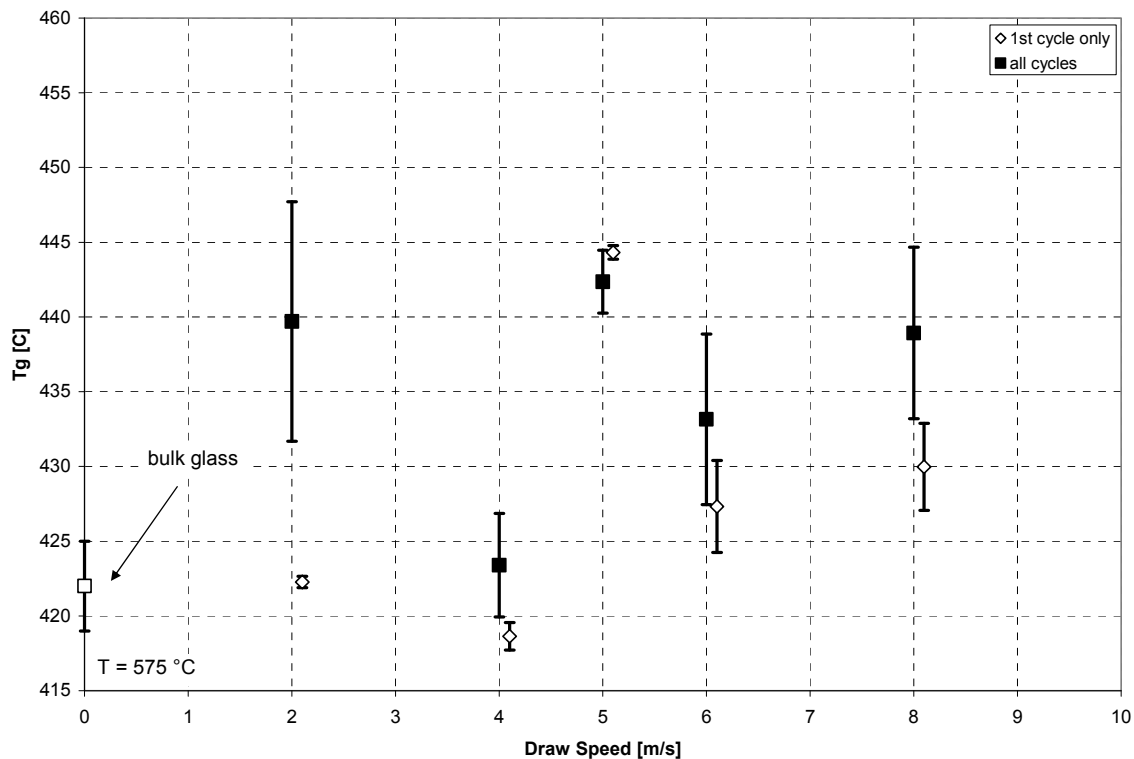


Figure 3.26. Glass transition temperatures for fibers drawn at 575°C vs drawing speed.

The average glass transition temperatures of the fibers at all three draw temperatures do generally not vary more than 20°C from the glass transition temperature of the bulk glass. The data for the first cycle, i.e. the unrelaxed fibers, shows varying behavior. The glass transition temperatures of the unrelaxed fibers are for the most part not close to the averages. There are some draw speeds however, such as 2 m/s at 525°C, 2, 5 and 8 m/s at 550°C and 5 m/s at 575°C where the T_g 's of the unrelaxed fibers are very close to the averages.

3.4.3 Pre - T_g Exotherms of Bi₂O₃ - B₂O₃ Glass Fibers

Pre - T_g exotherm areas were calculated as described in Chapter 3.3.5. Table 3.II displays this data in table format and Figure 3.28 to Figure 3.30 display this data graphically.

Table 3.II: Pre – T_g Exotherm Areas of all Fiber Samples

T [°C]	S [m/s]	Pre T _g exotherm [J/g/K]	
525	1	16	± 8
525	2	10	± 4
525	3.5	16	± 4
525	5	10	± 3
525	6.5	15	± 9
525	8	30	± 5
550	1	8	± 4
550	2	11	± 4
550	3.5	19	± 2
550	5	9	± 2
550	6.5	10	± 1
550	8	12	± 2
550	9.5	77	± 18
575	2	7	± 4
575	4	16	± 9
575	5	10	± 2
575	6	23	± 11
575	8	16	± 9

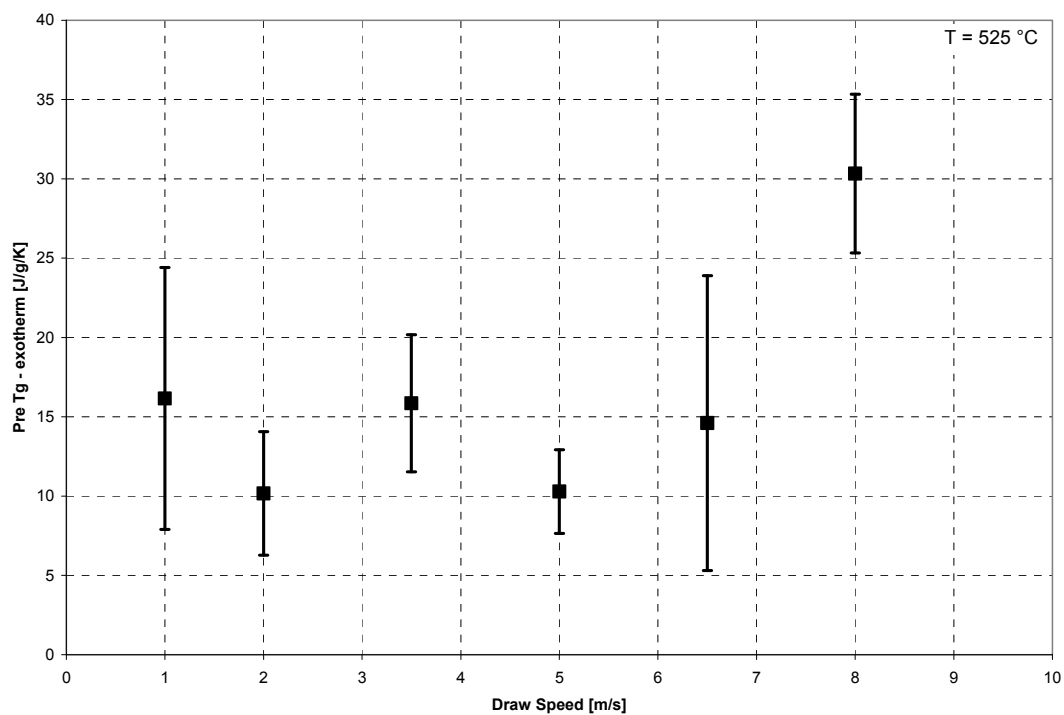


Figure 3.27. Pre – T_g exotherm areas vs drawing speed, draw temperature 525°C.

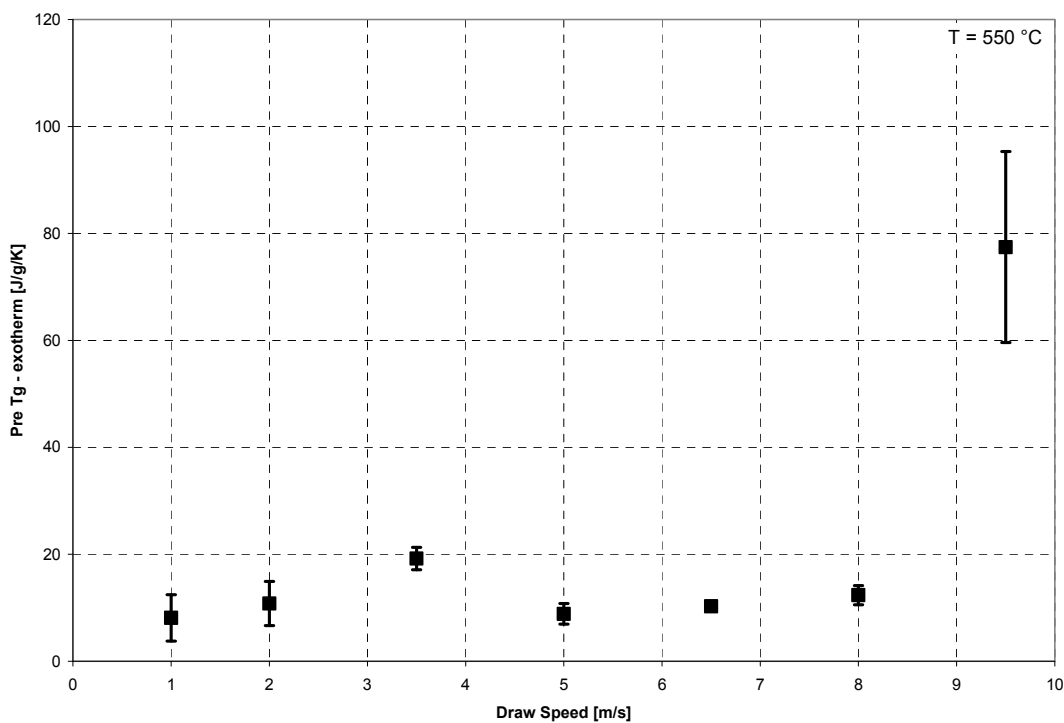


Figure 3.28. Pre – T_g exotherm areas vs drawing speed, draw temperature 550°C.

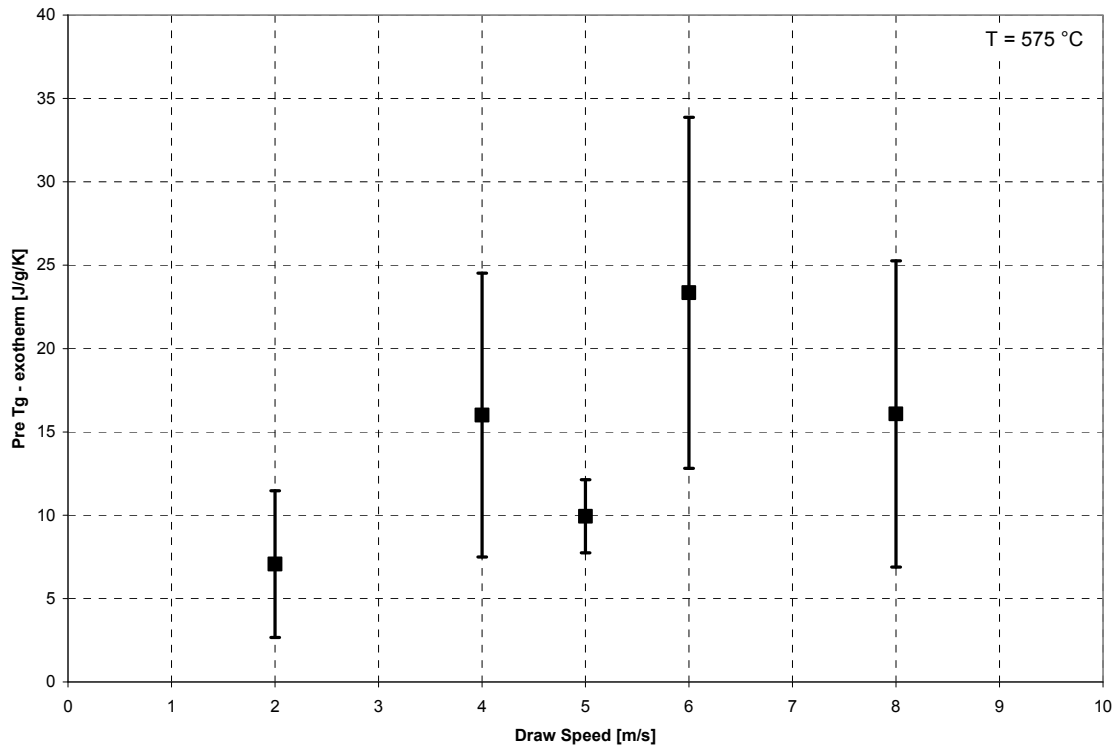


Figure 3.29. Pre – T_g exotherm areas vs drawing speed, draw temperature 575°C.

The pre – T_g exotherms of the drawn fibers show similar behavior for the two lower draw temperatures. The exotherm area is uniform at low speeds, increases slightly at middling draw speeds and returns to a low value. At the highest draw speeds the exotherm area increases significantly. At the lowest draw temperature of 525°C, the exotherm area increases by a factor of two, while the increase at 550°C is a factor of four. At the highest draw temperature of 575°C the exotherm areas show significantly higher standard deviations than at the lower temperatures. The exotherm areas also show an earlier increase by a factor of two, beginning at middle draw speeds.

3.4.4 Pre – T_g Exotherm Onset temperatures of Bi₂O₃ - B₂O₃ Glass Fibers

The onset temperatures of the pre – T_g exotherms have been determined as described above. The data is shown in Table 3.III and Figure 3.31 to Figure 3.33.

Table 3.III: Pre T_g – Exotherm Onset Temperature

T [°C]	S [m/s]	Pre T _g exotherm onset [°C]	
525	1	232	± 4
525	2	211	± 1
525	3.5	223	± 4
525	6.5	219	± 7
550	1	251	± 18
550	2	253	± 1
550	3	229	± 5
550	5	234	± 12
550	6.5	226	± 3
550	8	218	± 1
550	9.5	220	± 21
575	2	213	± 3
575	4	209	± 8
575	5	206	± 1
575	6	217	± 13
575	8	200	± 22

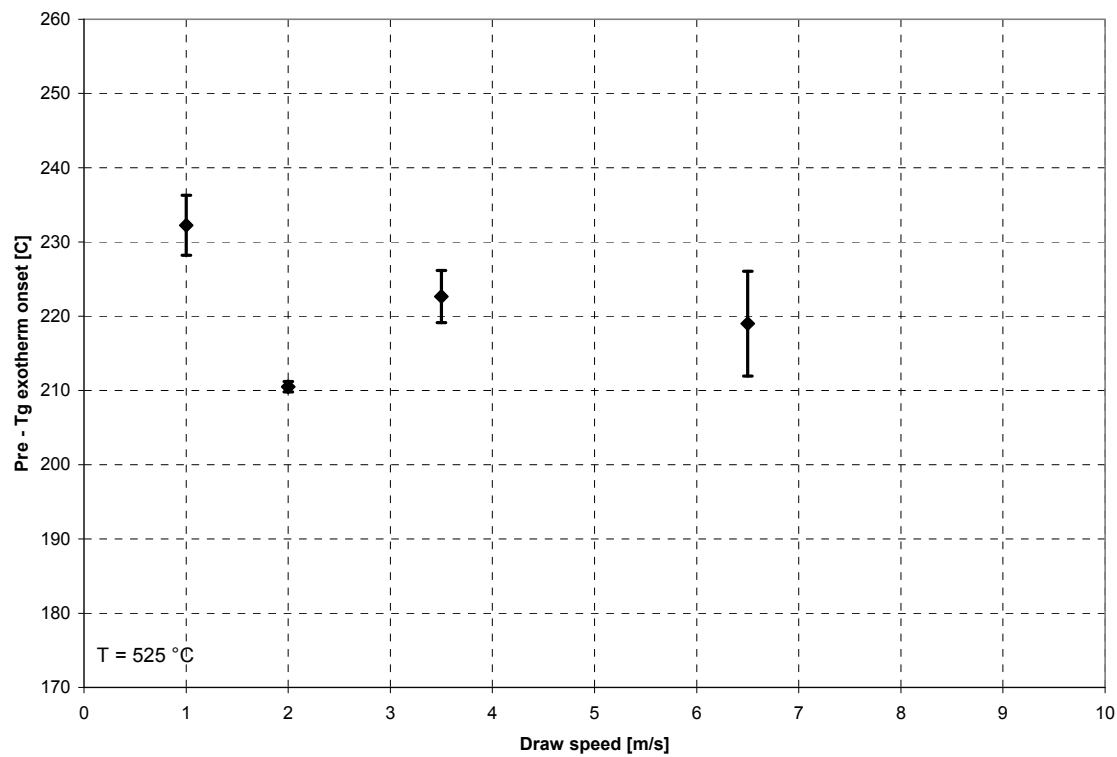


Figure 3.30. Pre T_g – exotherm onset temperature for fibers drawn at 525°C.

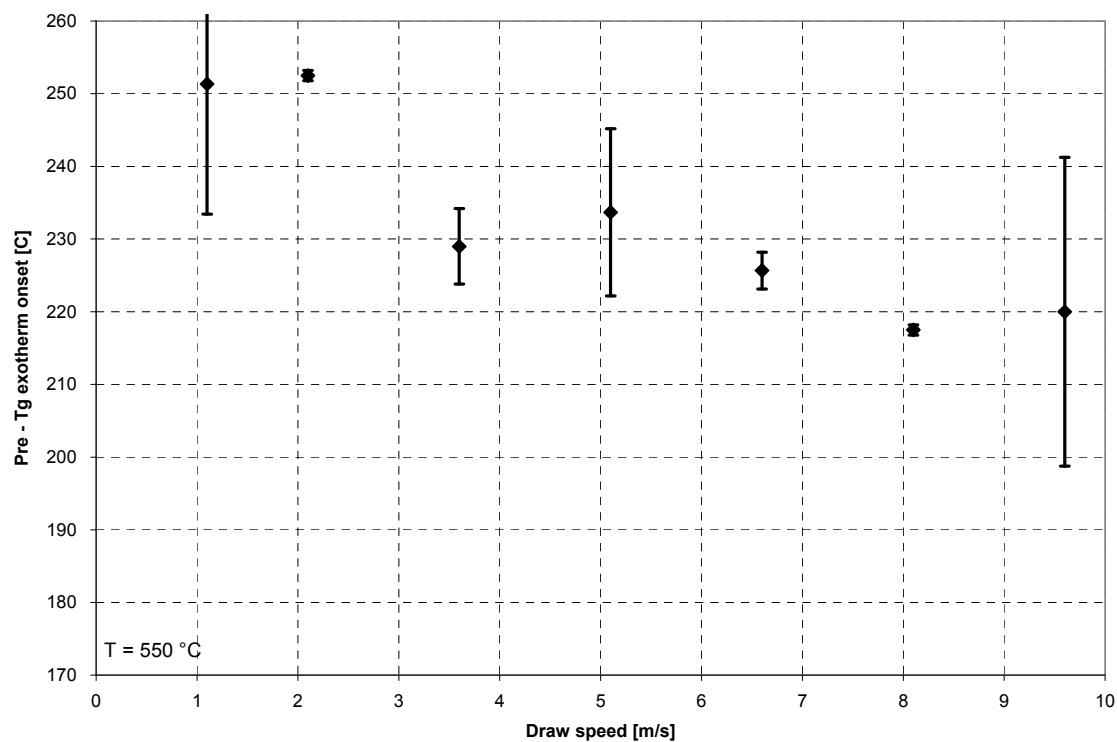


Figure 3.31. Pre T_g – exotherm onset temperature for fibers drawn at 550°C.

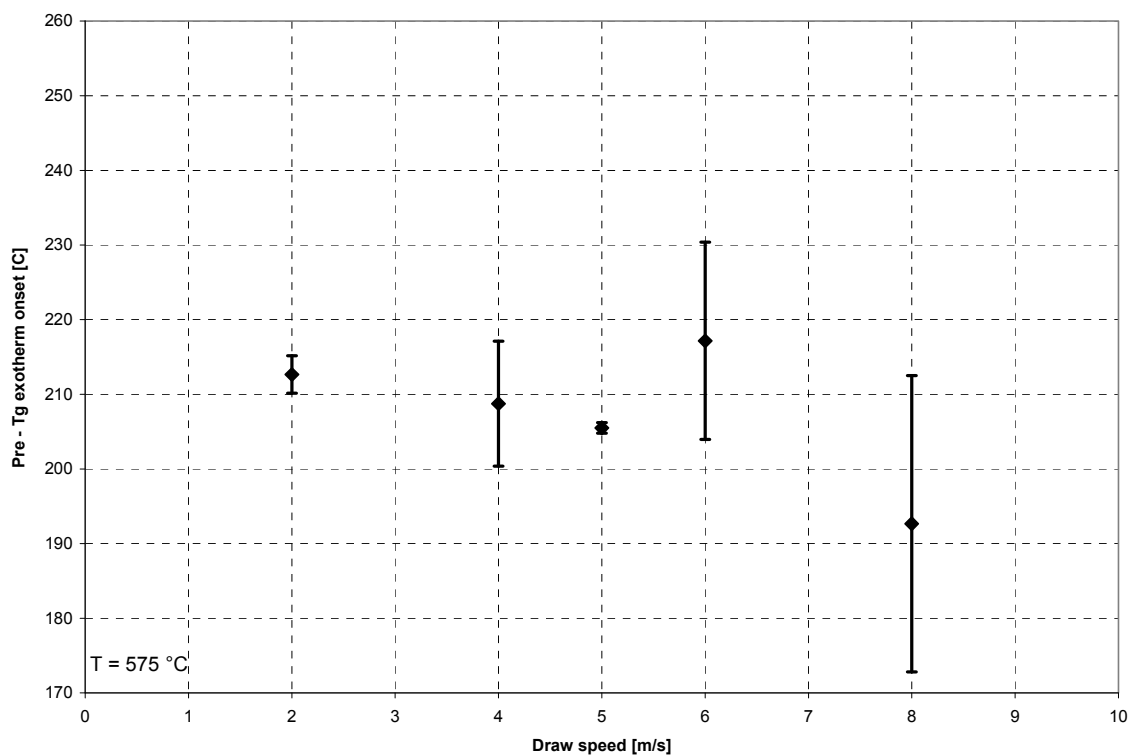


Figure 3.32. Pre T_g – exotherm onset temperature for fibers drawn at 575°C.

The onset temperatures for the pre – T_g exotherms all show a similar trend for all three draw temperatures. The onset temperatures decrease with increasing drawing speed.

3.4.5 Fictive Temperature of Bi₂O₃ - B₂O₃ Glass Fibers

The fictive temperatures were calculated as described previously. The raw data is shown in Table 3.IV.

Table 3.IV: Fictive Temperature Data for Fibers Drawn at all Temperatures

T[°C]	S [m/s]	Cycle	T _f [°C]		T[°C]	S [m/s]	Cycle	T _f [°C]	
					T[°C]	S [m/s]	Cycle	T _f [°C]	
525	1	1	466	± 2	550	1	1	475	± 1
525	1	2	452	± 5	550	1	2	445	± 2
525	1	3	455	± 4	550	1	3	448	± 1
525	1	4	455	± 5	550	1	4	450	± 2
525	1	5	461	± 3	550	1	5	449	± 4
525	2	1	467		550	2	1	467	± 11
525	2	2	434		550	2	2	443	± 1
525	2	3	438		550	2	3	442	± 6
525	2	4	438		550	2	4	440	± 11
525	2	5	444		550	2	5	448	± 4
525	3.5	1	473	± 3	550	3.5	1	480	± 3
525	3.5	2	449	± 1	550	3.5	2	456	± 9
525	3.5	3	457	± 1	550	3.5	3	454	± 3
525	3.5	4	462	± 3	550	3.5	4	459	± 8
525	3.5	5	465	± 10	550	3.5	5	462	± 11
525	6.5	1	484	± 4	550	6.5	1	480	± 2
525	6.5	2	452	± 1	550	6.5	2	455	± 4
525	6.5	3	455	± 2	550	6.5	3	456	± 3
525	6.5	4	458	± 1	550	6.5	4	461	± 1
525	6.5	5	462	± 2	550	8	1	489	
					550	8	2	442	
					550	8	3	442	
					550	8	5	448	

T[°C]	S [m/s]	Cycle	T _f [°C]	
575	2	1	467	
575	2	2	443	
575	2	3	439	
575	2	4	441	
575	2	5	439	
575	4	1	463	± 14
575	4	2	439	± 11
575	4	3	435	± 13
575	4	4	431	
575	4	5	435	
575	5	1	477	
575	5	2	441	
575	5	3	440	
575	6	1	481	± 4
575	6	2	454	± 1
575	6	3	471	± 12
575	8	1	485	± 2
575	8	2	461	± 5
575	8	3	466	± 12

The following graphs show various aspects of the raw data.

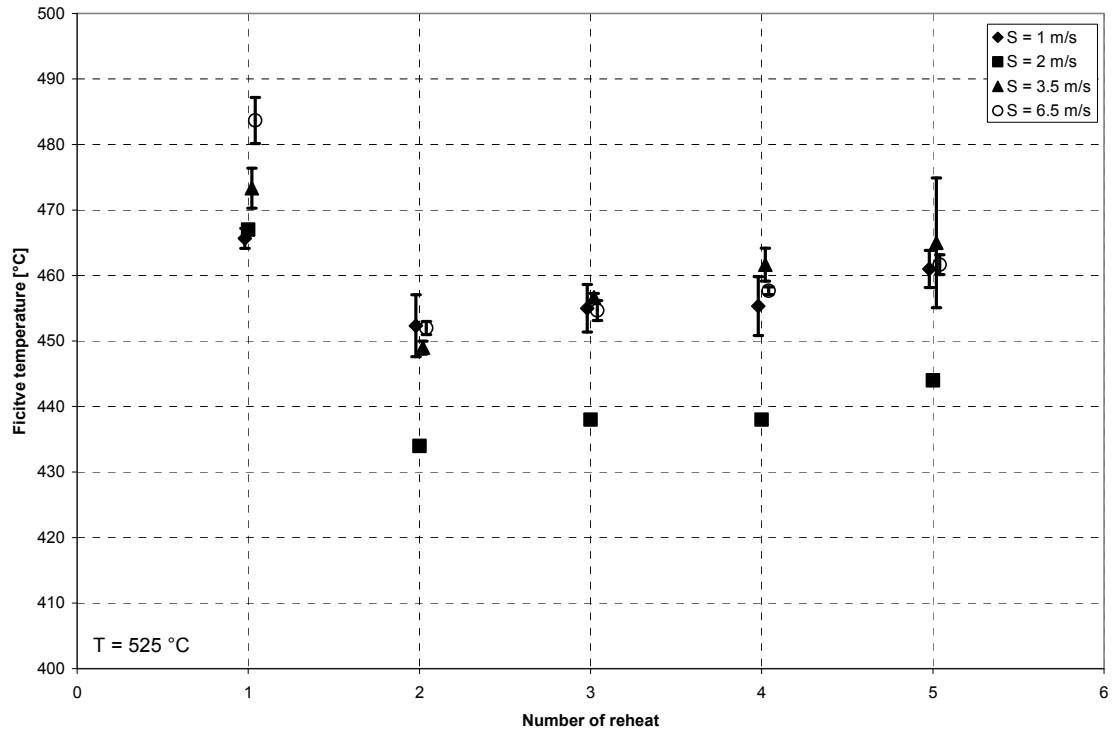


Figure 3.33. Fictive temperature of fibers drawn at 525°C and reheated 5 times.

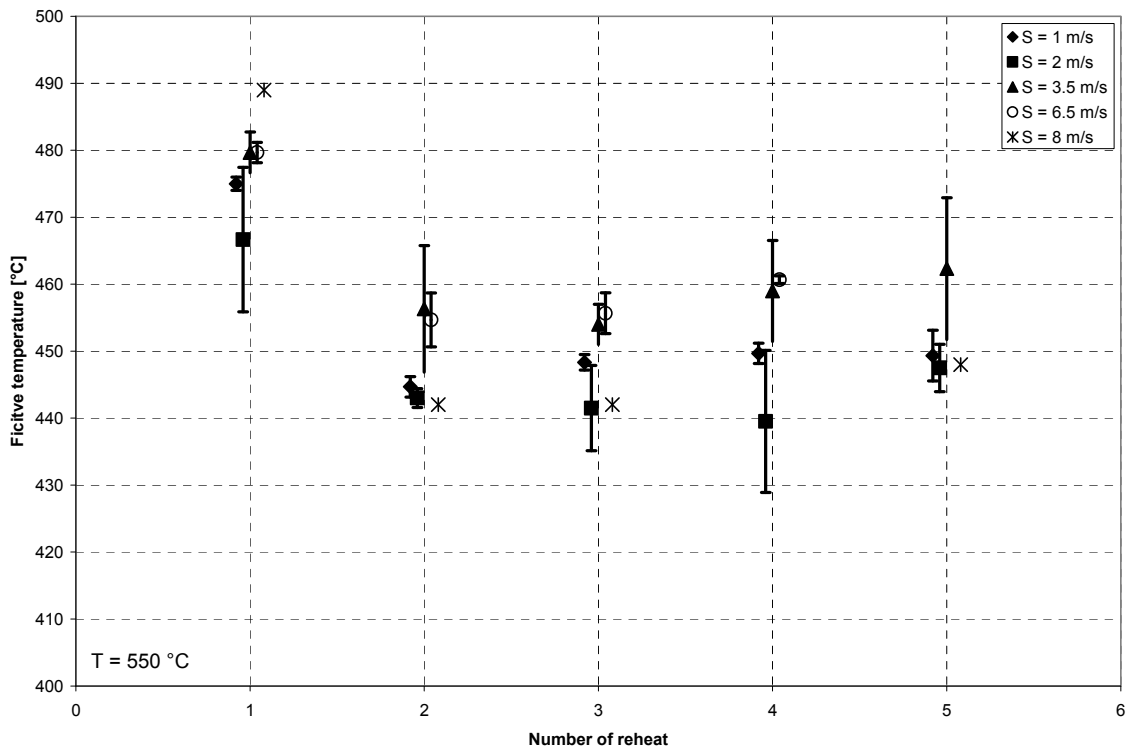


Figure 3.34. Fictive temperature of fibers drawn at 550°C and reheated 5 times.

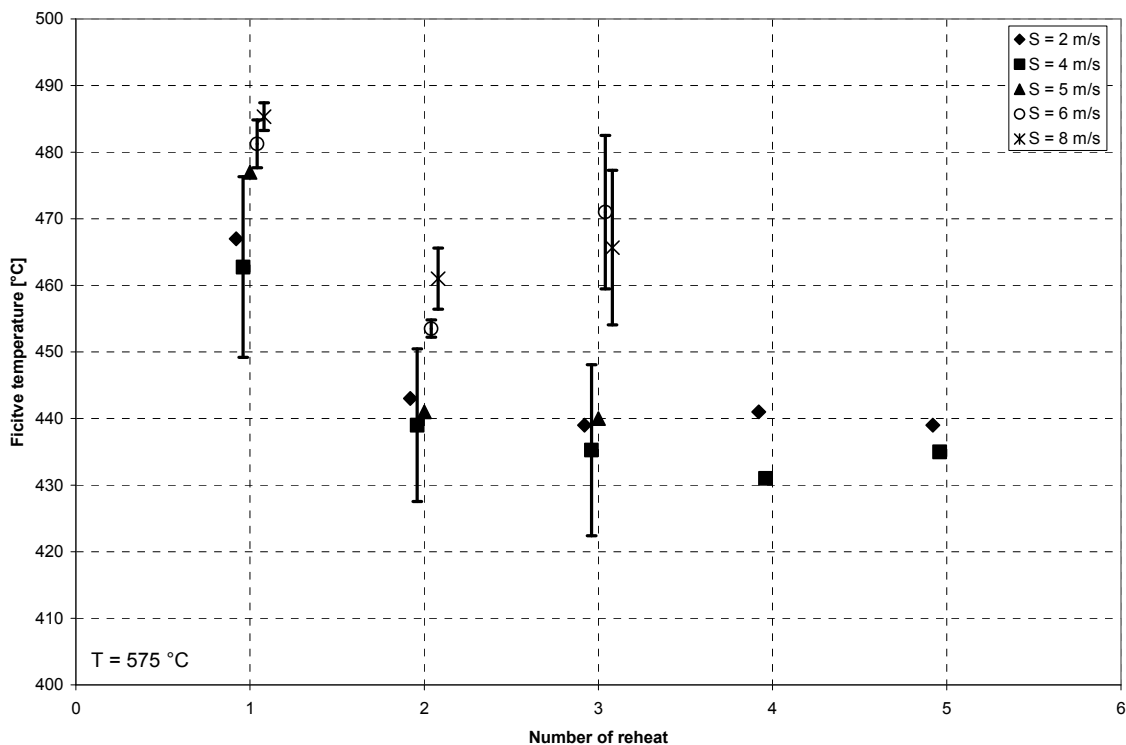


Figure 3.35. Fictive temperature of fibers drawn at 575°C and reheated 5 times.

Figure 3.34 to Figure 3.36 show the changes in fictive temperature when a sample is reheated repeatedly through the glass transition region. All samples show similar behavior. The fictive temperature of the fibers is high during the first heating cycle. It then drops considerably on reheating the fiber (cycle 2). On subsequent reheating the change in fictive temperature is much lower. It is difficult to determine whether the fictive temperature increases after the second reheating because of the large error bars. It is interesting to note that for a draw temperature of 525°C the fictive temperature of the 2 m/s fiber is lower than that of the 1 m/s fiber initially. On subsequent reheating cycles the difference disappears. This behavior is not observed in other properties of the fiber such as pre – T_g exotherm, heat capacity or glass transition.

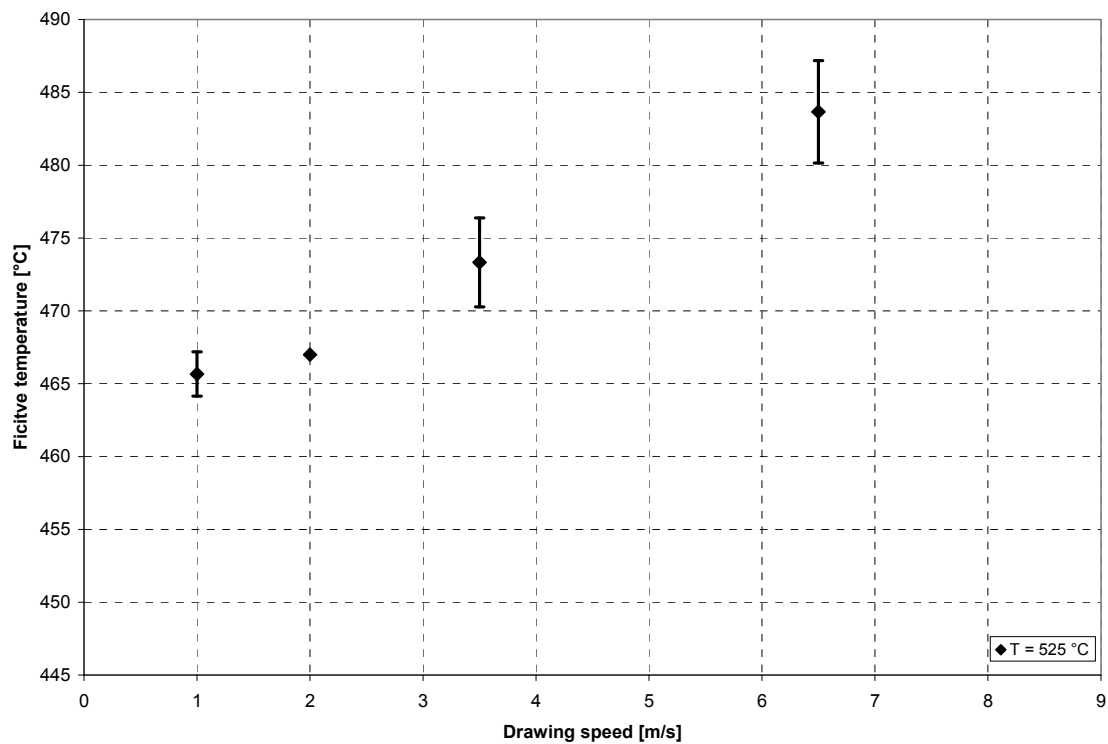


Figure 3.36. Fictive temperature of unrelaxed fibers drawn at 525°C vs drawing speed.

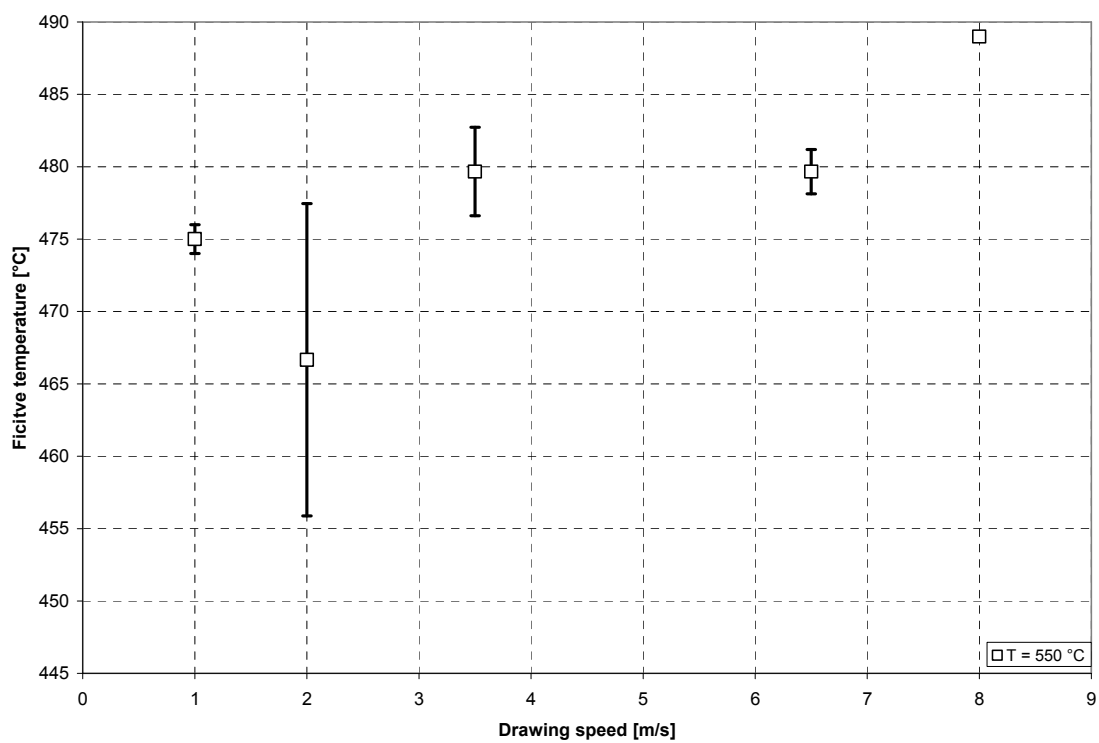


Figure 3.37. Fictive temperature of unrelaxed fibers drawn at 550°C vs drawing speed.

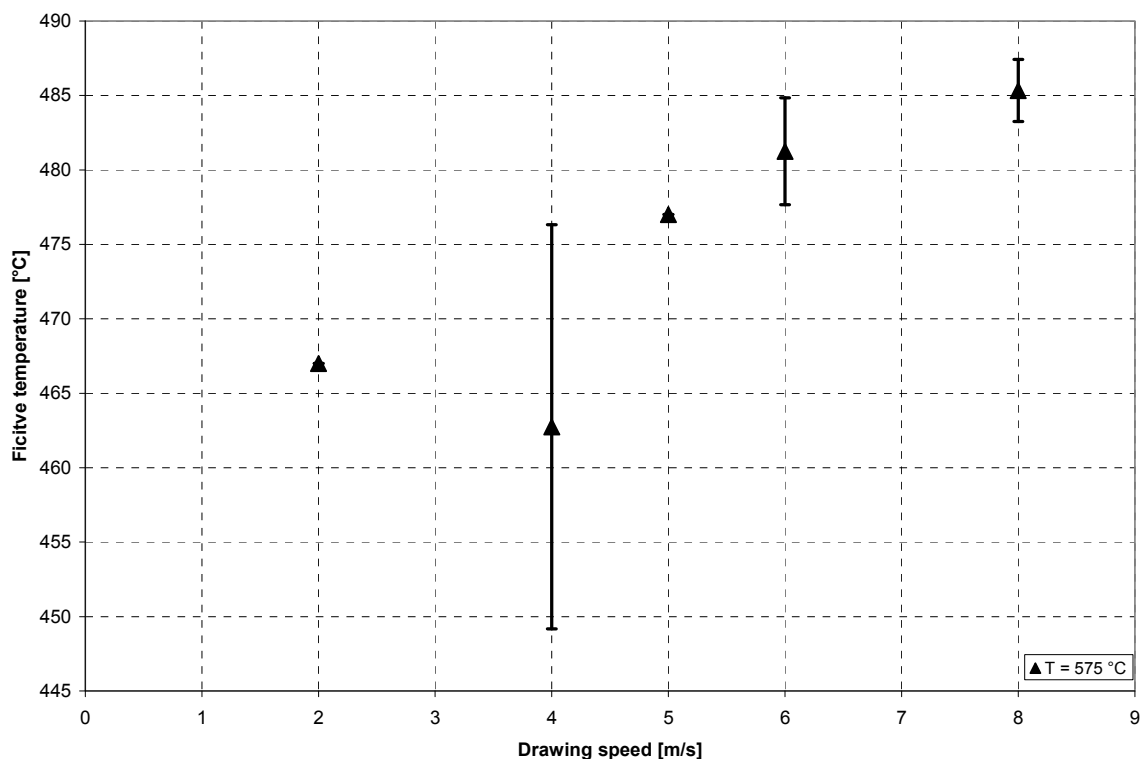


Figure 3.38. Fictive temperature of unrelaxed fibers drawn at 575°C vs drawing speed.

Figure 3.37 to Figure 3.39 show the changes in fictive temperature as the drawing speed increases. At each temperature the general trend for all samples is for an increasing fictive temperature with increasing draw speed. This trend is opposite that of the pre – T_g exotherm, which decreases with drawing speed, which is indicative of a more disordered structure due to a faster cooling rate and / or drawing stress.

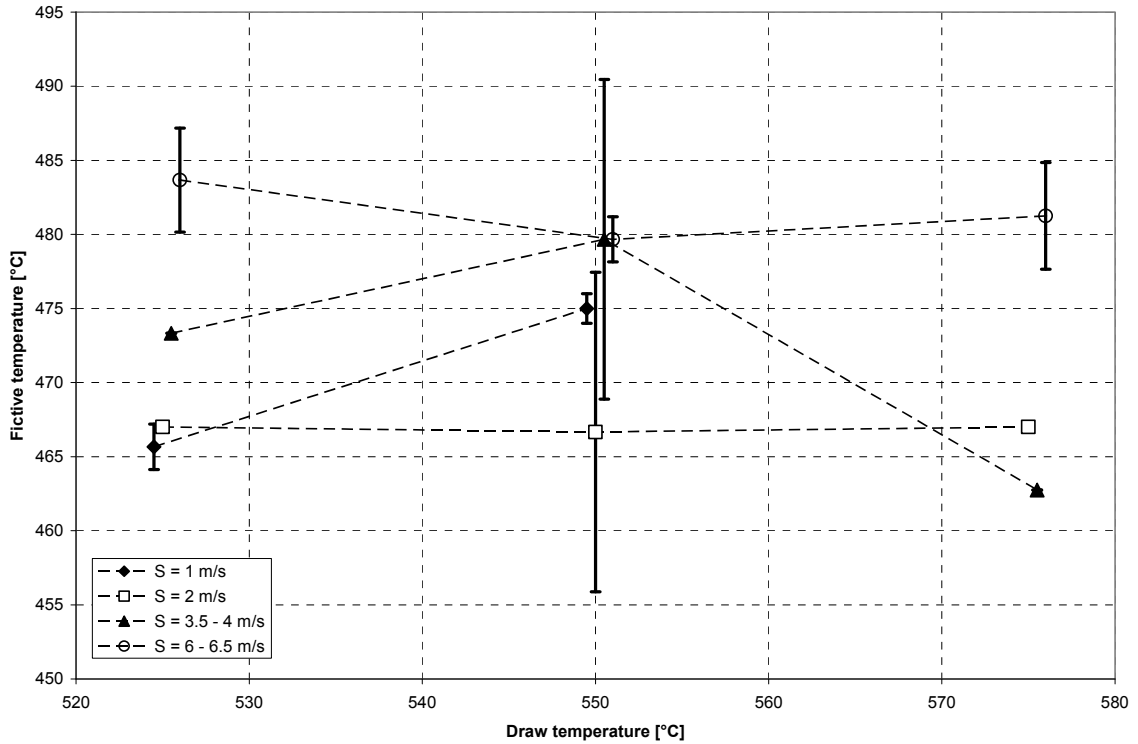


Figure 3.39. Fictive temperature of unrelaxed fibers vs drawing temperature for the different drawing speed regions (The lines are drawn to guide the eye).

And lastly Figure 3.40 shows the changes in fictive temperature versus the drawing temperature of the fibers. No common trends can be noted for the different drawing speed regions. At low drawing speeds of 1 m/s the fictive temperature increases from 525°C to 550°C. For draw speeds of 2 m/s the fictive temperature does not change, although the large error for the middle temperature may be obscuring the real value. For draw speeds of 3.5 to 4 m/s the fictive temperature decreases with increasing draw temperature and for draw speeds of 6 to 6.5 m/s the fictive temperature shows a small decrease as the draw temperature increases.

3.4.6 Heat Capacity of Bi_2O_3 - B_2O_3 Glass Fibers

The results of the heat capacity measurements are shown in tabular form in Table 3.V to Table 3.VII.

Table 3.V: Heat Capacity of Fibers Drawn at 525°C

S [m/s] T [°C]	Cp [J/g/K]					
	1		3.5		6.5	
100	0.263	± 0.012	0.337	± 0.020	0.332	± 0.010
150	0.277	± 0.013	0.352	± 0.021	0.351	± 0.013
200	0.289	± 0.012	0.368	± 0.022	0.368	± 0.015
250	0.300	± 0.012	0.387	± 0.023	0.386	± 0.017
300	0.310	± 0.012	0.406	± 0.023	0.405	± 0.019
350	0.319	± 0.012	0.425	± 0.025	0.423	± 0.021
400	0.325	± 0.010	0.442	± 0.030	0.439	± 0.023

Table 3.VI: Heat Capacity of Fibers Drawn at 550°C

S [m/s] T [°C]	Cp [J/g/K]							
	1		3.5		6.5		9.5	
100	0.342	± 0.023	0.241	± 0.020	0.279	± 0.046	0.421	± 0.086
150	0.354	± 0.022	0.247	± 0.021	0.294	± 0.053	0.433	± 0.089
200	0.365	± 0.022	0.251	± 0.021	0.304	± 0.058	0.443	± 0.093
250	0.377	± 0.024	0.256	± 0.023	0.315	± 0.064	0.455	± 0.095
300	0.390	± 0.029	0.262	± 0.023	0.326	± 0.070	0.464	± 0.099
350	0.403	± 0.035	0.266	± 0.024	0.335	± 0.076	0.462	± 0.112
400	0.415	± 0.040	0.268	± 0.023	0.342	± 0.080	0.456	± 0.124

Table 3.VII: Heat Capacity of Fibers Drawn at 575°C

S [m/s] T [°C]	Cp [J/g/K]			
	6		8	
100	0.268	± 0.046	0.264	± 0.011
150	0.270	± 0.047	0.267	± 0.013
200	0.275	± 0.048	0.270	± 0.016
250	0.278	± 0.049	0.271	± 0.022
300	0.276	± 0.052	0.267	± 0.031
350	0.274	± 0.057	0.261	± 0.042
400	0.271	± 0.061	0.255	± 0.048

Several different graphical views are presented in Figures 3.41 to 3.46.. First the heat capacity behavior is shown vs temperature and the second graph shows the behavior of the heat capacity vs the draw speed of the fiber. For all these graphs, the reader is advised that the temperature coordinates of the points have been varied slightly in order to facilitate readability. The actual temperatures are as given in the above tables.

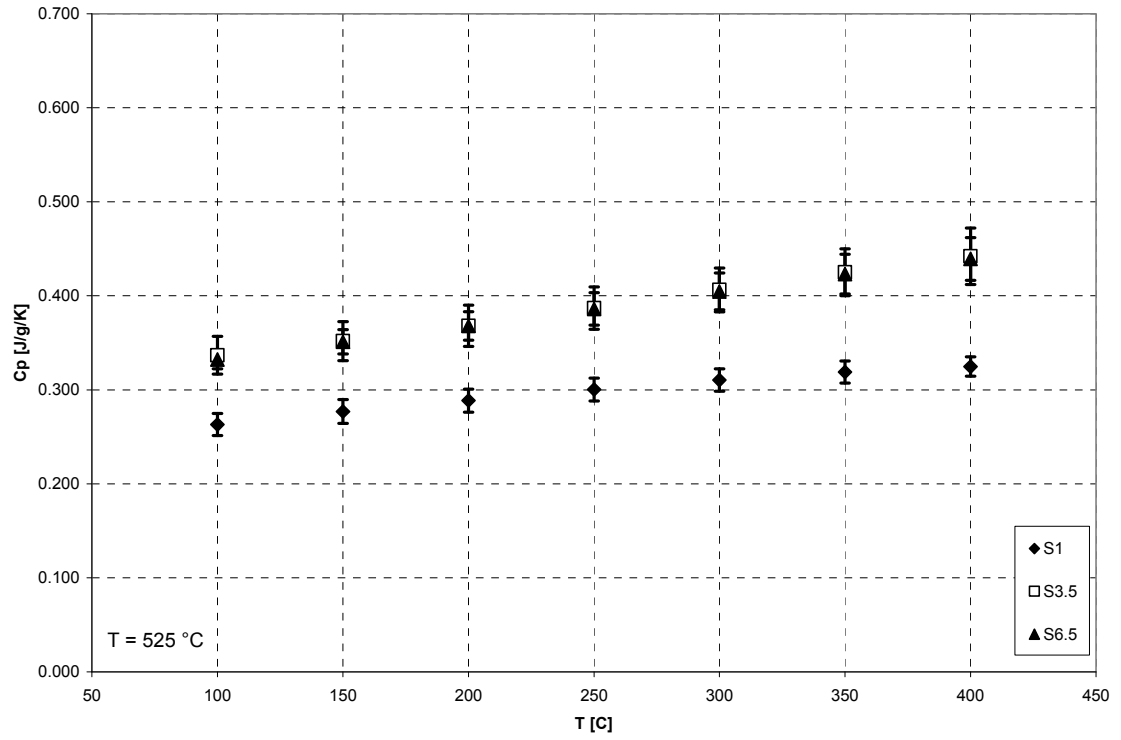


Figure 3.40. Heat capacity of fibers drawn at 525°C.

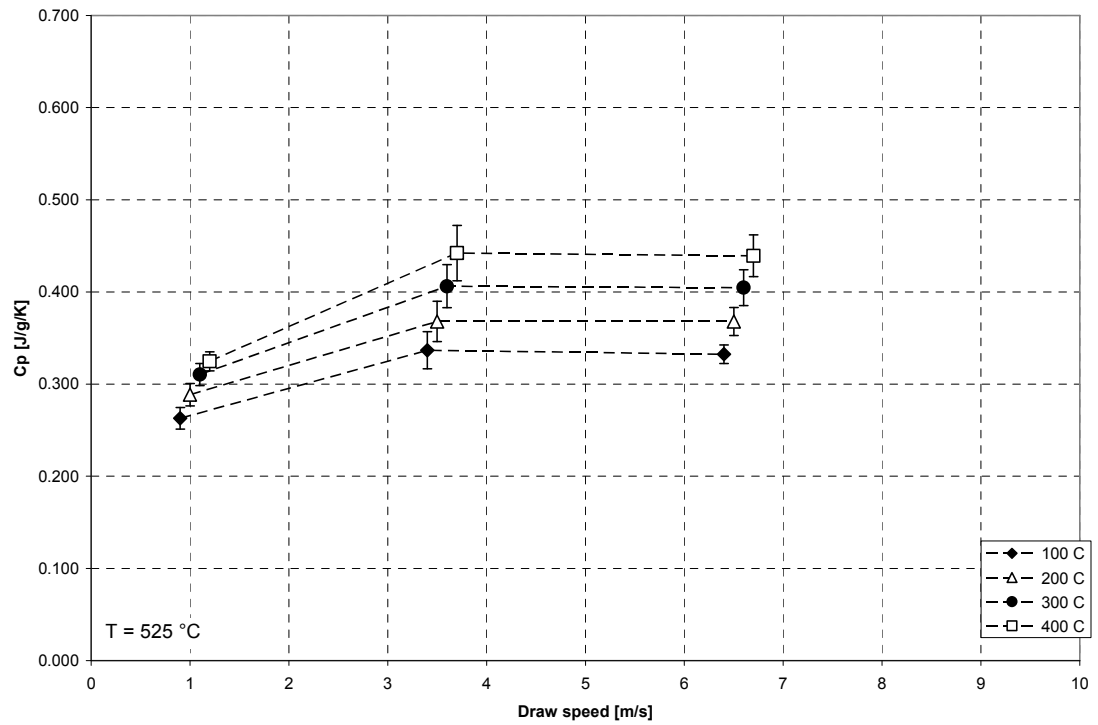


Figure 3.41. Heat capacity of fibers drawn at 525°C vs drawing speed (The lines were drawn to guide the eye).

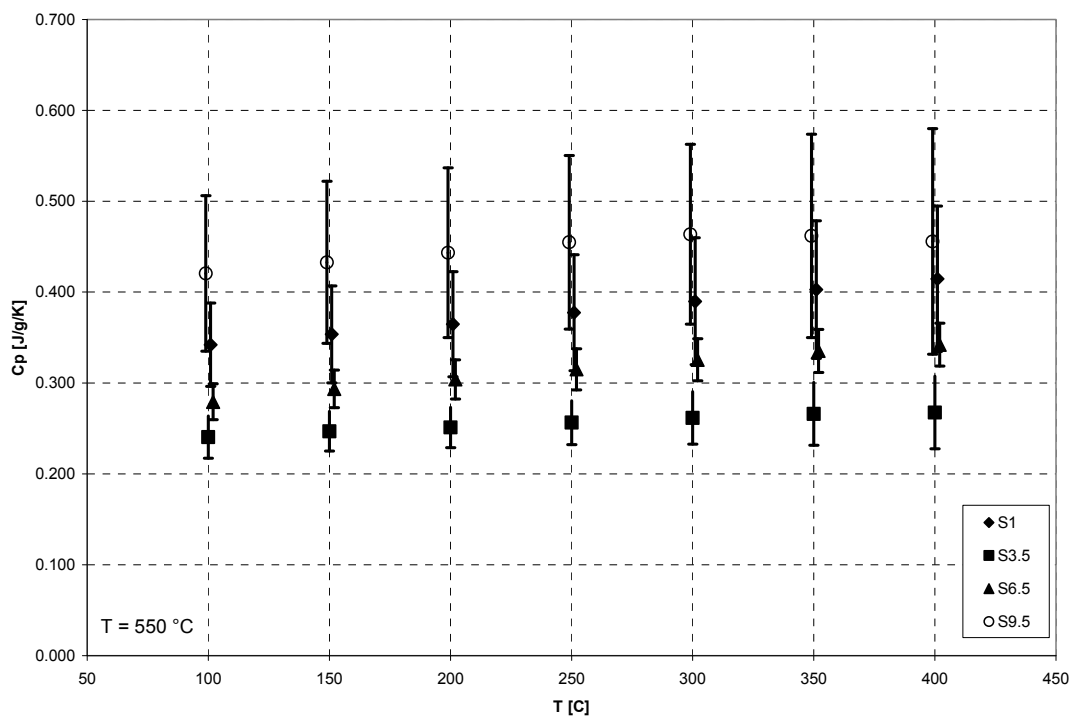


Figure 3.42. Heat capacity of fibers drawn at 550°C.

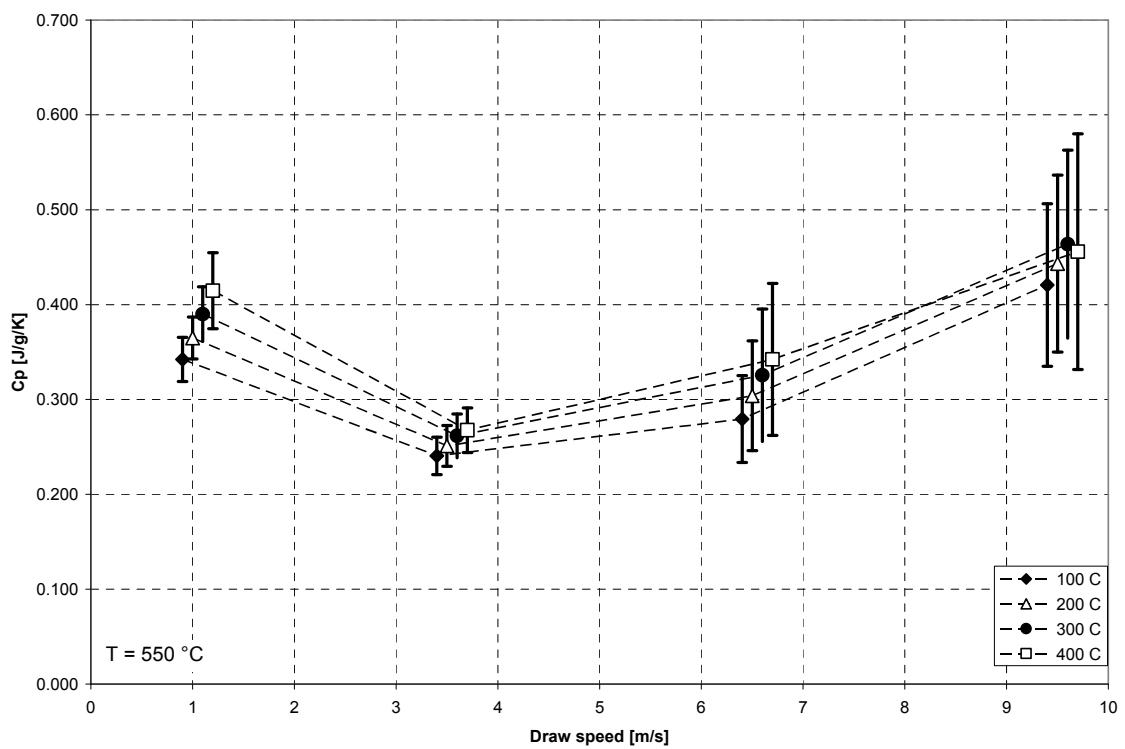


Figure 3.43. Heat capacity of fibers drawn at 550°C vs drawing speed (The lines were drawn to guide the eye).

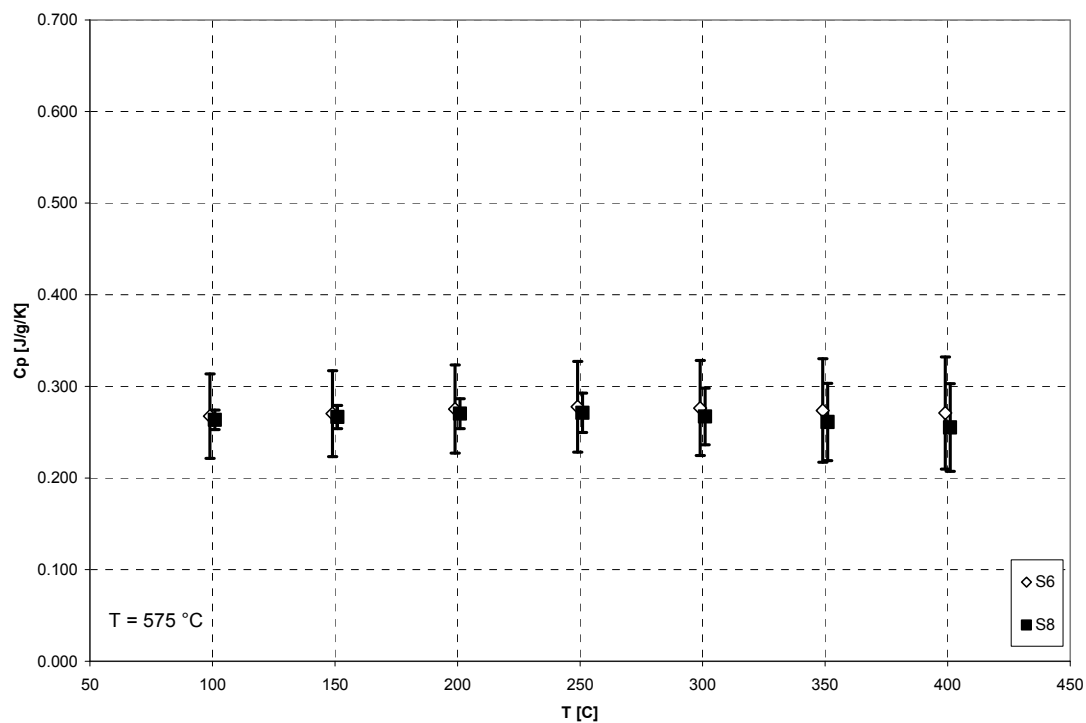


Figure 3.44. Heat capacity of fibers drawn at 575°C.

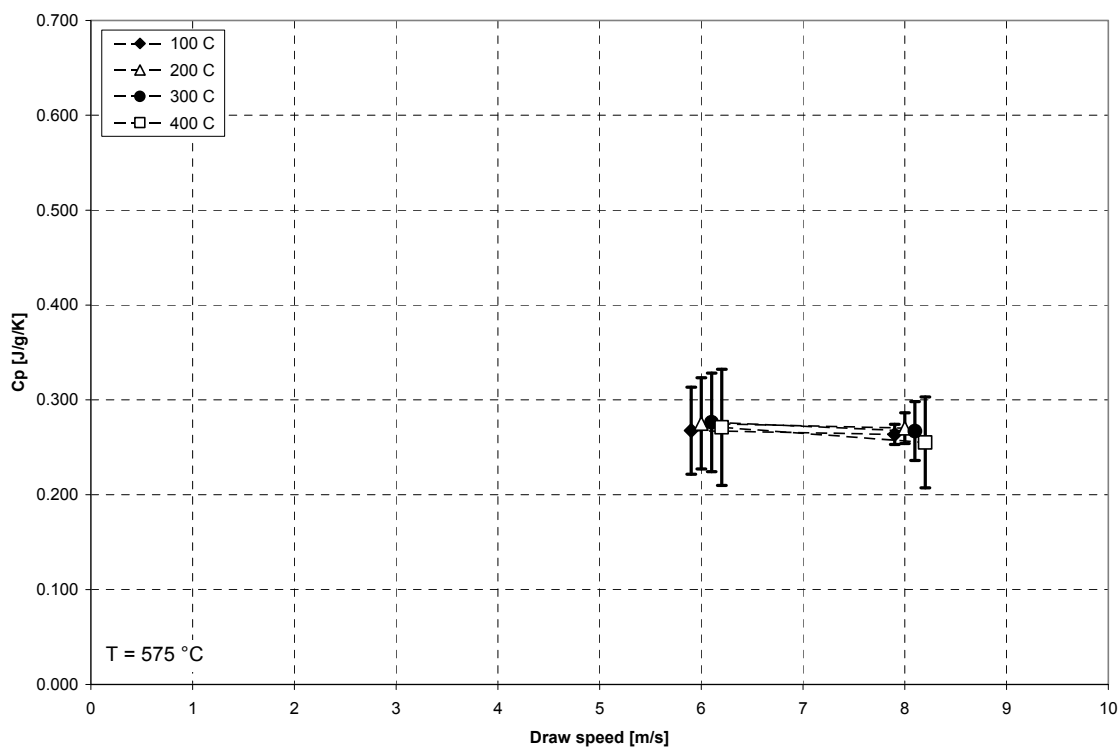


Figure 3.45. Heat capacity of fibers drawn at 575°C vs drawing speed (The lines were drawn to guide the eye).

3.4.7 Change of the glass transition of the fibers on reheating

All glass fibers show a change of glass transition behavior after being reheated through the glass transition multiple times. This behavior shows itself in a steadily decreasing peak height of the glass transition. This behavior can clearly be seen in Figure 3.47.

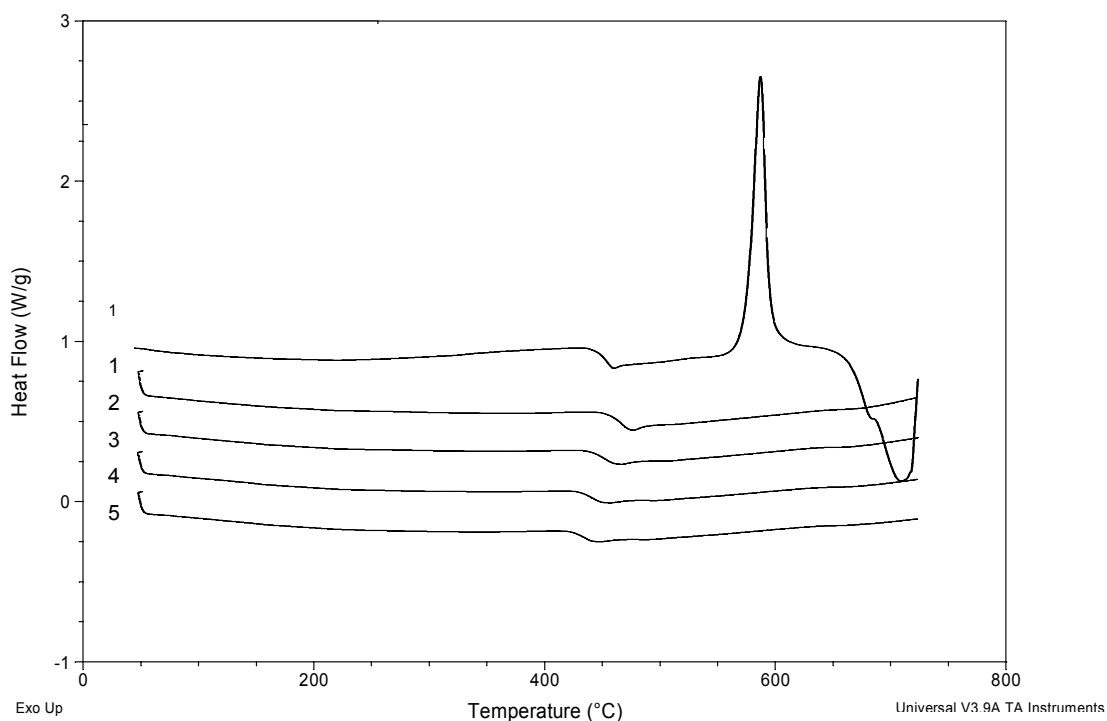


Figure 3.46. Reheating cycles of a glass fiber sample, heated to well above T_g .

The above sample has been heated to 725°C, which is well above the T_g of 443°C. This allows the fibers to crystallize as can be seen in the large exotherm. Fibers heated to temperatures closer to T_g exhibit the same behavior in the decreasing height of the glass transition however. Based on this assumption the height of the glass transition was plotted in Figure 3.49.

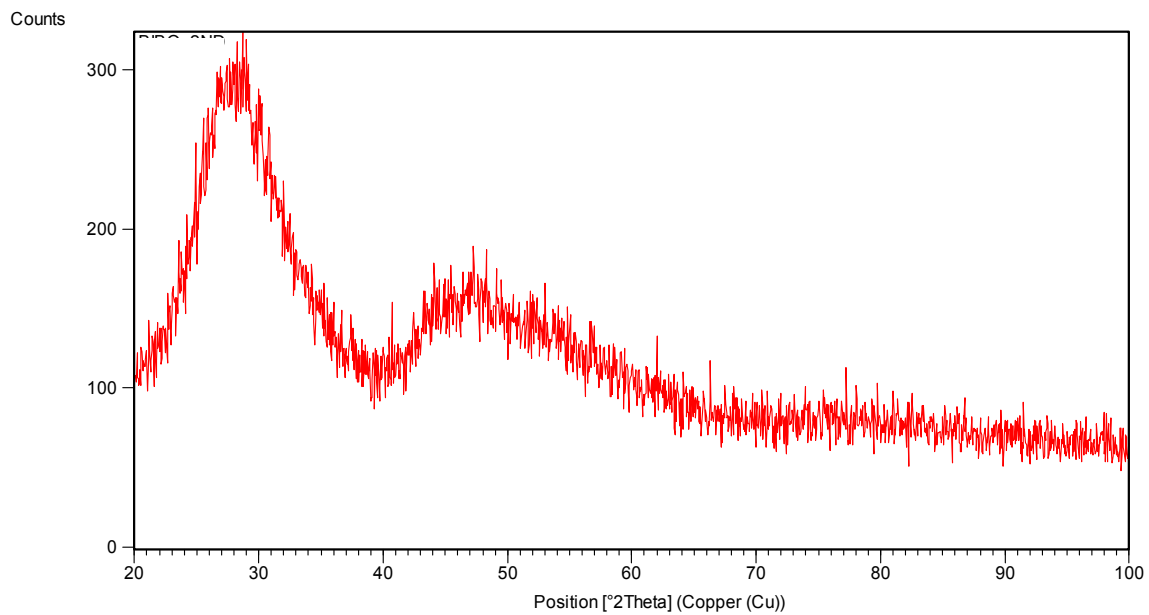


Figure 3.47. XRD pattern of glass fiber after a 1 hour soak at $T_g + 30^\circ\text{C}$.

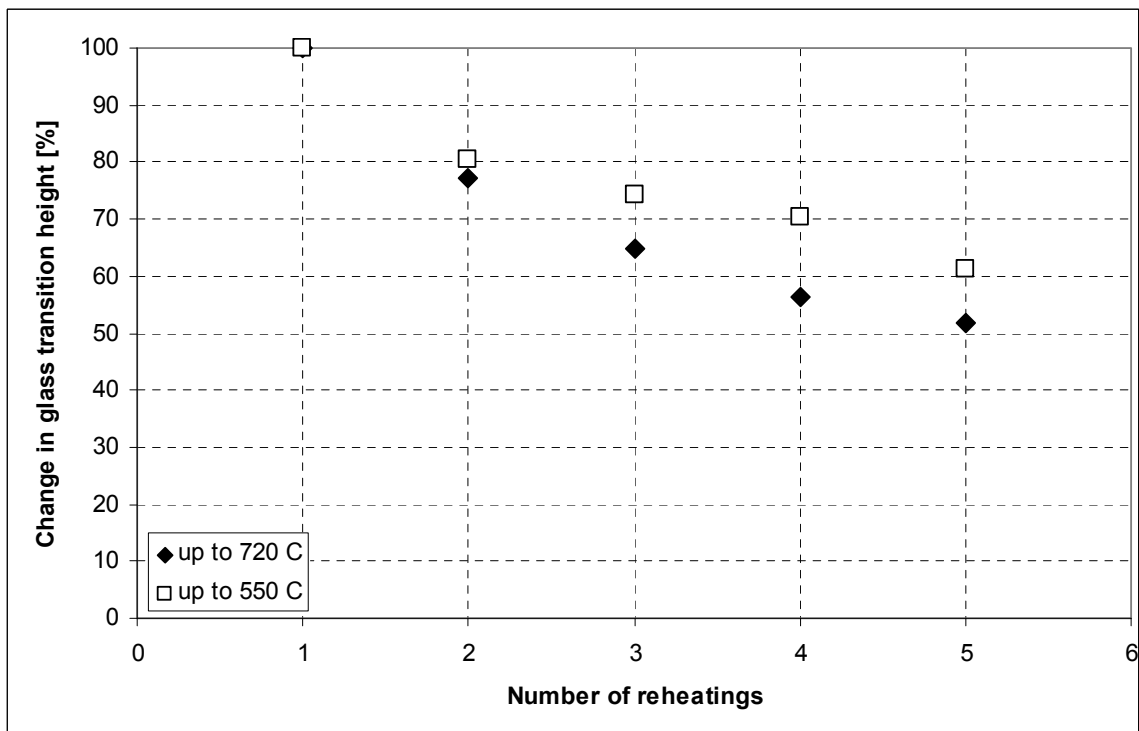


Figure 3.48. Change in crystallization in fibers upon reheating above T_g .

The data shows that the change in glass transition height is larger if the sample is heated to a higher temperature above T_g . However, even after 5 reheating cycles to temperatures 250 K above T_g there is still a measurable glass transition and there is still glass left.

Further XRD measurements of the fibers after five reheating cycles and after a soak at $T_g + 30^\circ\text{C}$ for 1 hour detected no crystals in the fibers. This is most likely due to the fact that the volume fraction of the crystals is too small for the experimental setup to detect. The experiment used a thin layer of powder on a zero – background holder with a medium count time of 5 seconds.

3.5 Discussion and Conclusions

The diameter of a glass fiber is determined by the mass flow rate of glass out of the bushing. This quantity is proportional to the geometry of the bushing and the pressure over the nozzle; and inversely proportional to the viscosity of the glass. This allows for the prediction of the general trends for the fiber diameter when the drawing parameters of speed and temperature change. At a constant temperature the viscosity of a glass is constant and so the mass flow rate out of the bushing is also constant. This will result in a decrease in the fiber diameter as draw speed increases because the same amount of glass flowing from the bushing will be drawn into a cylinder of the same volume. Since the length of the cylinder increases the diameter has to decrease to keep the volume constant. On the other hand, if the temperature increases the mass flow rate increases. Thus the amount of glass available for drawing into a fiber increases and the diameter of the fibers increases as well. The data shows this behavior very well. The fact that the slope of the curves changes is related to the fact that the viscosity of glasses does not change linearly with temperature.⁴

The glass transition temperatures show a similar trend for all draw temperatures. The glass transition temperature for low drawing speeds is lower than that of bulk glass and then increases to values similar to that of bulk glass. The data also indicates that in general the glass transition temperature is lower on the first cycle and then increases as the glass is reheated multiple times as shown by the higher average values of T_g with larger standard deviations. Figure 3.50 shows the glass transition of a single fiber sample. The glass transition increases as the fiber ages. The aging behavior of fibers has been noted by King⁴⁴ and Cerqua–Richardson^{37,43} in arsenic selenide fibers. They attribute this behavior with the healing of defects induced in the fiber by the drawing process. As the fiber is aged the structure of the glass is trying to relax and heal the defects induced in the glass. Temperatures above the glass transition make this very easy, allowing even structural rearrangement. However the reduction in the

glass transition peak height at the same time indicates a process that is reducing the total amount of glass available. This will change the composition of the glass that remains. The two most likely processes are phase separation of the glass as the composition of $0.25 \text{ Bi}_2\text{O}_3 - 0.75 \text{ B}_2\text{O}_3$ is situated at the edge of the miscibility dome for bismuth borate glasses and crystallization.

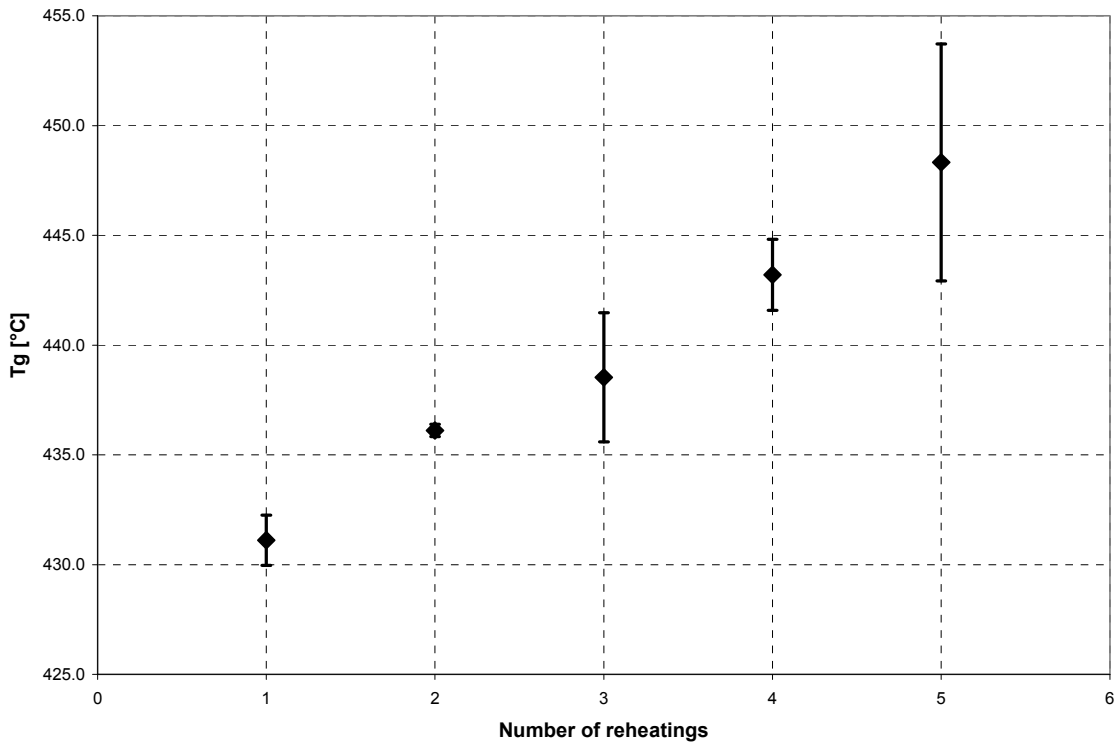


Figure 3.49. Change in glass transition over several reheating cycles.

The pre – T_g exotherm data for all temperatures show a maximum at intermediate drawing speeds. For the draw temperatures of 525 and 550°C that maximum occurs locally at a draw speed of 3.5 m/s whereas for the draw temperature of 575°C the maximum occurs at a draw speed of 6 m/s. For the two lower draw temperatures the absolute maximum for draw speeds occurs at the draw speed of 9.5 m/s. For the draw temperature of 575°C measurements at that draw speed are unfortunately unavailable, because the vibrations of the tower at speeds close to 10 m/s cause the fiber to break at this temperature. According to a number of authors^{3,12,37,43} a maximum in the pre – T_g exotherm

indicates the onset of shear thinning in the glass. In this case it is not exactly clear whether the onset of shear thinning is at the local or overall maxima. The magnitude of the absolute maximum however, seems to indicate that shear thinning only sets in at very high speeds at low temperatures. Whereas at high temperatures, the presence of only one maximum seems to indicate that the onset of shear thinning behavior occurs at a lower temperature. In addition the complex behavior of the data seems to indicate a number of structural changes are occurring during the drawing of the fibers. The fact that the diameters of the fibers and therefore the cooling rates are not exactly the same for all draw rates will influence this picture.^{3,43} Rapid relaxation phenomena such as King⁴³ observed in his work with arsenic selenides were not observed. The pre – T_g exotherm did not increase again for the fibers drawn at 575°C. This is a reasonable behavior since the glass transition temperatures of the bismuth borate glass fibers are far above those of arsenic selenides and room temperature relaxations processes are much more unlikely for these fibers. The fibers were also put into cold storage immediately after drawing further suppressing any relaxation processes. Therefore, mainly due to the higher glass transition temperatures, the fibers are expected to behave similar to silicate glass fibers. The shape of the data suggests that there are several distinct regions at each drawing temperature. For the data at 525°C the increase of the exotherm area at a draw speed of 3.5 m/s suggests that there is a defect process other than frozen in stress occurring that will be healed at higher draw speeds before the creation of high energy defects such as broken bonds begins. The same holds true for the data at 550°C. The data at 575°C is a little less clear due to the large standard deviations but the same general phenomena holds true.

The pre – T_g exotherm onset data shown in Figure 3.31 – Figure 3.33 shows a trend that decreases with increasing drawing speed for all three drawing temperatures. The highest onset temperature occurs for fibers drawn at 1 m/s at 550°C but all fibers show onsets in the same range for high draw speeds. The decreasing trend indicates that the spectrum of relaxation times shifts toward more rapid processes as drawing speed is increased¹⁵. These rapid processes

of excess energy release are able to begin at lower temperatures due to a lower kinetic barrier and a larger driving force.

Figure 3.34 to Figure 3.36 show the changes in the glass fibers as they are aged by cycling them back and forth to a temperature above T_g . The data shows that all samples show a memory effect. The fictive temperature decreases on reheating, tending towards the equilibrium. But then T_f begins to increase again trending away from equilibrium. When plotting the fictive temperature of the unrelaxed glass fibers the data shows the same trend for all draw temperatures. The fictive temperature increases with draw speed, as is expected. The higher the draw speed, the more disordered the material is. A more disordered material implies a higher fictive temperature. The surprising part is that the fictive temperature increases almost linearly with drawing speed. If one compares the fictive temperature data for the regions of drawing speeds directly with temperature one can note a trend that seems to invert itself. At low draw speeds 1 m/s the fictive temperature increases with draw speed. At slightly higher drawing speeds the fictive temperature shows only minimal changes with draw temperature (this is obscured by the large error for the data for 550°C). At medium draw speeds of ca 3 – 4.5 m/s the fictive temperature shows a decrease as the draw temperature increases. And at high draw speeds (6 – 6.5 m/s) the fictive temperature does again not show a large change as the temperature is increased. Most notable is the drop in fictive temperature at speeds of 3.5 to 4 m/s. There may be a connection between this behavior and the postulated existence of a secondary relaxation mechanism at these speeds.

The heat capacity data for the glass fibers is shown in Figure 3.41 - Figure 3.46. The two views for the heat capacity data are given so two distinct behaviors can be shown. First all fiber samples show a linear increase of the heat capacity with temperature. It should be noted that all heat capacity data was taken below the glass transition point. The heat capacity data of high speed and low temperature fibers and low speed high temperature fibers could not be taken due to the difficulty in reliably producing large enough amounts of fibers at those conditions.

When the heat capacity data is viewed versus draw speed the different draw temperatures show different behavior. For a low draw temperature of 525°C the heat capacity increases with draw speed, but seems to be approaching a equilibrium value. After increasing the draw temperature to 550°C the heat capacity shows a minimum value for all temperatures at a draw speed of 3.5 m/s. This also hints at the existence of a relaxation mechanism that is active at this draw speed. If the energy release of the samples is high then the heat capacity of these samples measured after the relaxation would be low. Then as the draw speed approaches the shear thinning regime, the heat capacity would rise again, as more and more defects are introduced into the structure. But since the shear thinning regime is actually not exceeded, the heat capacity measured at 9.5 m/s is high. Unfortunately due to the low amount of data available at a draw temperature of 575°C no trends can be seen clearly.

The next chapter examines the structural units in the glass with Raman spectroscopy. The reader is also referred to chapter 6 for a summary of the findings.

3.6 References

1. T.R. Bott and A.J. Barker, "The Examination of Glass Fiber Surfaces Using a Scanning Electron Microscope," *Glass Technol.*, **9** [2] 42-4 (1968).
2. I.M. Daniel and O. Ishai, *Engineering Mechanics*. Oxford University Press, New York, 1994.
3. C.T. Ho, "The Effect of Fiber Drawing Conditions on the Onset of Shear Thinning and the Corresponding Relaxation Phenomena of Silicate Glasses"; Ph.D. Thesis. Alfred University, Alfred, New York, 1995.
4. K.L. Loewenstein, *The Manufacturing Technology of Continuous Glass Fibers*, 3rd ed.; Ch. 1-3. Elsevier, Amsterdam, 1993.
5. K.L. Loewenstein and J. Dowd, "An Investigation of the Relationship Between Glass Fiber Tensile Strength, the Temperature of the Glass from which the Fiber is Drawn, and Fiber Diameter," *Glass Technol.*, **9** [6] 164-71 (1968).
6. C.L. McKinnis and J.W. Sutton, "The Glass Melting Process: II Glass Structure and the Effect of "Melting History" on Glass Properties," *J. Am. Ceram. Soc.*, **42** [5] 250-3 (1959).
7. J.F. Sproull and G.E. Rindone, "Effect of Melting History on the Mechanical Properties of Glass: I, Role of Melting Time and Atmosphere," *J. Am. Ceram. Soc.*, **57** [4] 160-4 (1974).
8. J.F. Sproull and G.E. Rindone, "Effect of Melting History on the Mechanical Properties of Glass: II, Effects of Raw Materials and Bubbling Gases through the Melt," *J. Am. Ceram. Soc.*, **58** [1] 35-40 (1975).
9. W.F. Thomas, "An Investigation of the Factors Likely to Affect the Strength and Properties of Glass Fibers," *Phys. Chem. Glasses*, **1** [1] 4-18 (1960).
10. A.K. Varshneya, *Fundamentals of Inorganic Glasses*; Ch. 2. Academic Press, Boston, Massachusetts, 1994.
11. E.-J. Donth, *The Glass Transition: Relaxation Dynamics in Liquids and Disordered Materials*; p. 1-63. Edited by A. Zunger, R. Hull, R.M. Osgood Jr., and H. Sakaki. Springer - Verlag, New York, 2001.
12. Y. Zheng, "Forming Condition Effects on Structure and Properties of Glass and Glass Fiber"; Ph.D. Thesis. Alfred University, Alfred, New York, 2002.

13. A.Q. Tool, "Relation between Inelastic Deformability and Thermal Expansion of Glass in Its Annealing Range," *J. Am. Ceram. Soc.*, **29** [8] 240-53 (1946).
14. G.W. Scherer, *Relaxation in Glass and Composites*; Ch. 1-3. John Wiley & Sons, New York, 1986.
15. S.A. Brawer, *Relaxation in Viscous Liquids and Glasses*; Ch. 1-4. American Ceramic Society, Ohio, 1985.
16. S.M. Rekhson and J.P. Ducroux, "Treatment of Non-Linearity in Structural Relaxation in Glass," pp.100-34 in *The Physics of Non - Crystalline Solids*. Edited by L.D. Pye, W.C. LaCourse, and H.J. Stevens. Taylor & Francis, London, England, 1992.
17. G.W. Scherer, "Theory of Relaxation," *J. Non-Cryst. Solids*, **123** [1-3] 75-89 (1990).
18. I.M. Hodge, "Enthalpy Relaxation and Recovery in Amorphous Materials," *J. Non-Cryst. Solids*, **196** [1] 211-66 (1994).
19. A.Q. Tool and C.G. Eichlin, "Variations Caused in the Heating Curves of Glass by Heat Treatment," *J. Am. Ceram. Soc.*, **14** [4] 276-308 (1931).
20. H.N. Ritland, "Limitations of the Fictive Temperature Concept," *J. Am. Ceram. Soc.*, **39** [12] 403-6 (1956).
21. S. Spinner and A. Napolitano, "Further Studies in the Annealing of a Borosilicate Glass," *J. Res. Natl. Bur. Stand. (U.S.)*, **70A** [2] 147-52 (1966).
22. M. Hara and S. Setoshi, "Density Changes of Glass over the Transition Range," *Rep. Res. Asahi Glass Co.*, **5** [1] 126-35 (1955).
23. P.B. Macedo and S. Spinner, "Effects of a Distribution of Volume Relaxation Time in the Annealing of BSC Glasses," *J. Res. Natl. Bur. Stand. (U.S.)*, **71A** [3] 231-8 (1967).
24. C.T. Moynihan, "Structural Relaxation and the Glass Transition," pp. 1-18 in *Structure, Dynamics and Properties of Silicate Melts*. Edited by J.F. Stebbins, P.F. McMillan, and D.B. Dingwell. Mineralogical Society of America, Washington, D.C., 1995.
25. O.S. Narayanaswamy, "A Model of Structural Relaxation in Glass," *J. Am. Ceram. Soc.*, **54** [10] 491-8 (1971).

26. C.T. Moynihan, A.J. Easteal, and M.A. DeBolt, "Dependence of the Fictive Temperature of Glass on Cooling Rate," *J. Am. Ceram. Soc.*, **59** [1-2] 12-21 (1976).
27. C.T. Moynihan, L.P. Boesch, and N.L. Laberge, "Electric Field Relaxation in Vitreous Ionic Conductors," *Phys. Chem. Glasses*, **14** [6] 122-5 (1973).
28. C.T. Moynihan and A.V. Lesikar, "Comparison and Analysis of Relaxation Processes at the Glass Transition Temperature," *Ann. N.Y. Acad. Sci.*, **371** [1] 151-64 (1981).
29. C.T. Moynihan, A.J. Bruce, D.L. Gavin, S.R. Loehr, S.M. Opalka, and M.G. Drexhage, "Physical Aging of Heavy Metal Fluoride Glasses - Sub - T_g Enthalpy Relaxation in a ZrF_4 - BaF_2 - LaF_3 - AlF_3 Glass," *Polym. Eng. Sci.*, **24** [14] 1117-22 (1984)).
30. M.A. DeBolt, A.J. Easteal, P.B. Macedo, and C.T. Moynihan, "Analysis of Structural Relaxation in Glass Using Rate Heating Data," *J. Am. Ceram. Soc.*, **59** [1-2] 16-21 (1976).
31. A.J. Easteal, J.A. Wilder, R.K. Mohr, and C.T. Moynihan, "Heat Capacity and Structural Relaxation of Enthalpy in As_2Se_3 Glass," *J. Am. Ceram. Soc.*, **60** [3-4] 134-8 (1977).
32. G. Adam and J. Gibbs, "On the Temperature Dependence of Cooperative Relaxation Properties in Glass - Forming Liquids," *J. Chem. Phys.*, **43** [1] 139-46 (1965).
33. P.K. Gupta, "Glass Fibers for Composite Materials," Ch. 2 in *Fibre Reinforcement for Composite Materials*. Edited by A.R. Bunsell. Elsevier, Cambridge, Massachusetts 1988.
34. J. Huang and P.K. Gupta, "Enthalpy Relaxation in Thin Glass Fibers," *J. Non-Cryst. Solids*, **151** [1-2] 175-81 (1992).
35. J. Huang, "Structural Relaxation in Thin Glass Fibers"; Ph.D. Thesis. Ohio State University, Ann Arbor, Ohio 1992.
36. J.P. Ducroux, S.M. Rekhson, and F.L. Merat, "Structural Relaxation in Thermorheological Complex Materials," *J. Non-Cryst. Solids*, **172-174** [1] 541-53 (1994).
37. K. Cerqua-Richardson, "Time-Dependence Defect Processes in Low T_g Chalcogenide Glasses"; Ph.D. Thesis. Alfred University, Alfred, New York, 1992.

38. N. Clavaguera, M.T. Clavaguera-Mora, S. Surinach, and M.D. Baro, "Relaxation Processes below the Glass Transition in a GeSe_2 - GeTe - Sb_2Te_3 Alloy," *J. Non-Cryst. Solids*, **104** [2-3] 283-90 (1988).
39. M. Koide, R. Sato, T. Komatsu, and K. Matusita, "Low-Temperature Deformation of Fluoride and Oxide Glasses below Their Glass Transition Temperatures," *J. Non-Cryst. Solids*, **177** [1] 427-31 (1994).
40. H.L. Ma, X.H. Zhang, J. Lucas and C.T. Moynihan, "Relaxation Near Room Temperature in Tellurium Chalcogenide Glasses," *J. Non-Cryst. Solids*, **140** [1-3] 209-14 (1992).
41. A.J. Pappin, J.M. Hutchinson, and M.D. Ingram, "The Appearance of Annealing Pre-Peaks in Inorganic Glasses: New Experimental Results: A Theoretical Interpretation," *J. Non-Cryst. Solids*, **172-174** [1] 584-91 (1994).
42. H.S. Chen and C.R. Kurkjian, "Sub-sub T_g Relaxations in a B_2O_3 Glass," *J. Am. Ceram. Soc.*, **66** [9] 613-8 (1983).
43. W. King, "Structural Investigation of Arsenic Selenide Glass Fibers"; Ph.D. Thesis. Alfred University, Alfred, New York, 1996.
44. G.W. Scherer, "Volume Relaxation far From Equilibrium," *J. Am. Ceram. Soc.*, **69** [4] 374-81 (1986).
45. S.H. Shieh, "Mechanical Properties of Arsenic Triselenide Glass Fibers"; Ph.D. Thesis. Alfred University, Alfred, New York, 1989.
46. C.Q. Shen, "Effects of Forming Conditions on Structure, Relaxation Phenomena and Aging Behaviors of Glass Fibers"; Ph.D. Thesis. Alfred University, Alfred, New York, 1999.
47. M.M. Hall and J. Walker, Fictive Temperature Calculation, [Computer Program] Alfred University, Alfred, New York, 2007.

4 Micro Confocal Raman Study

4.1 Introduction

In the early twentieth century the rapidly developing theory of quantum mechanics turned to the interactions between molecules and electromagnetic waves. The Austrian physicist Smekal¹ was the first to predict that photons scattering from molecules could have energies other than the incident frequency. The first experimental confirmation of this phenomenon was accomplished on benzene in 1928 by Indian physicist C. V. Raman. For this discovery Raman was awarded the Nobel prize and the effect carries his name to this day.

Early Raman instruments used the light of a mercury arc lamp to achieve their results. As the Raman effect is rather weak the experimental applicability of this technique was limited until a stronger light source could be found. The advent of cheap lasers in the mid 1960's provided such a source. This caused a great revival of the technique, which is in widespread use nowadays, despite great advances in IR spectroscopy.

Raman spectroscopy has several advantages over IR and the two techniques compliment each other as we will see. Raman spectra can be obtained from very small samples even without the use of microscopes. But since the addition of a microscope to the tools of Raman spectroscopy, spectra of single crystals, single fibers and liquid samples as small as 1 ml are experimentally possible. The weak Raman activity of water makes the technique ideal for studying aqueous solutions. And the fact that most spectra can be obtained in the visible region makes the technique very well suited for biological uses. The geometries of a Raman spectroscope also facilitate measurements in high temperature and high pressure cells.^{2,3}

4.2 Literature Review

4.2.1 Raman Spectroscopy^{2,3}

The following is a quick overview of the quantum mechanical basis of Raman scattering. Raman scattering is one of the phenomena occurring during the interaction of electromagnetic radiation with matter. Electromagnetic radiation can be described as both waves and particles. The following treatment will first treat the electromagnetic radiation as particles, despite the fact that historically the equations for the wave like aspect of the interactions were worked out first.

Electromagnetic “wave particles” are also called photons. According to Plack’s formula the relationship between their energy E and their frequency ν can be described as shown in Equation 4.1.

$$E = h \cdot \nu \quad (4.1)$$

h : Planck’s constant

Interaction of a photon with matter can result in three distinct processes:

- Absorption is caused when the energy of the photon is equal to the difference between two energy levels of the molecule
- Emission results from an excited molecule after the stable lifetime of the exited state has been reached
- Scattering of the photon takes place immediately during interaction ($\sim 10^{-14}$ sec) when the energy of the photon does not correspond to the difference between two energy levels of the molecule. Scattering occurring elastically, i.e. without a change in photon energy, is called Rayleigh scattering, while inelastic scattering – scattering where the photon energy is changed – is called Raman scattering.

The normal Raman effect is the photon interacting with the molecule and changing its energy in a characteristic fashion. Figure 4.1 shows the phenomena schematically.

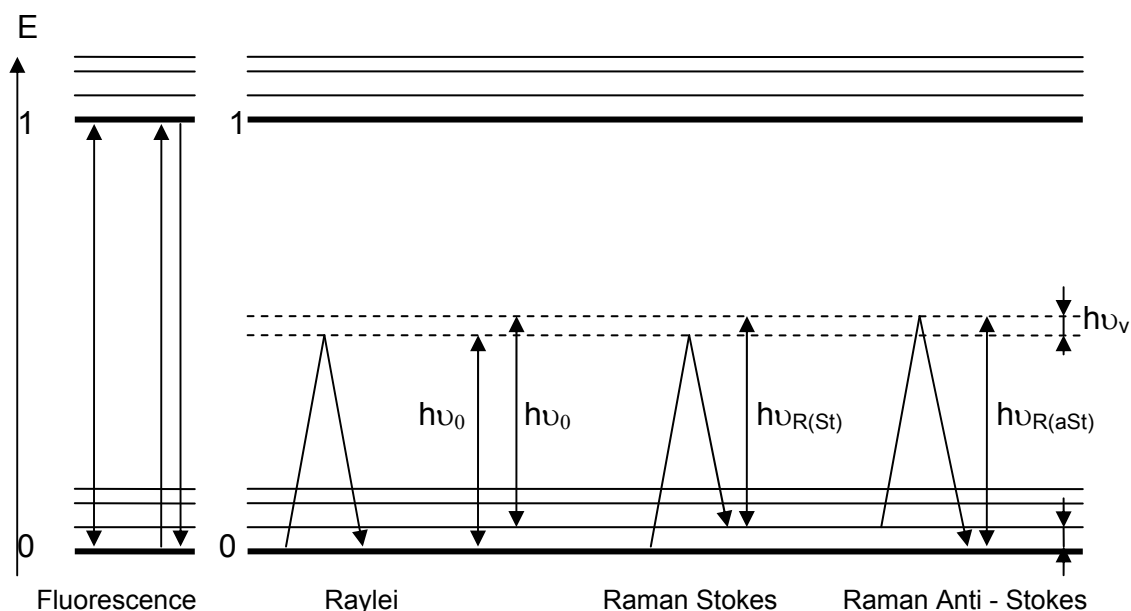


Figure 4.1. Comparison between resonance fluorescence and scattering ($h\nu_{R(st)}$: Energy of Raman Stokes shift, $h\nu_{R(aSt)}$: Energy of Raman Anti-Stokes shift).

In Figure 4.1 resonance fluorescence is compared to scattering phenomena. Fluorescence is a two – photon process. Each process, absorption and emission of two identical photons, can be observed separately. The two processes are separated by the lifetime of the excited state ($\sim 10^{-8}$ sec).

The scattering event cannot be separated into two single – photon steps. The energy levels shown by the dashed lines are non – stationary, i.e. not permanent, levels of the molecule. The initial photon of energy $h\nu_0$ may be unchanged during scattering (Rayleigh scattering), may be decreased during scattering (Stokes scattering) or may be increased during scattering (anti – Stokes scattering). Two electronic levels, 0 and 1, are shown in the diagram. At room temperature most of the molecules will occupy the ground vibrational state 0, according to Boltzman's law. When irradiated by monochromatic light of energy $h\nu_0$, a spectrum as shown in Figure 4.2 can be observed.

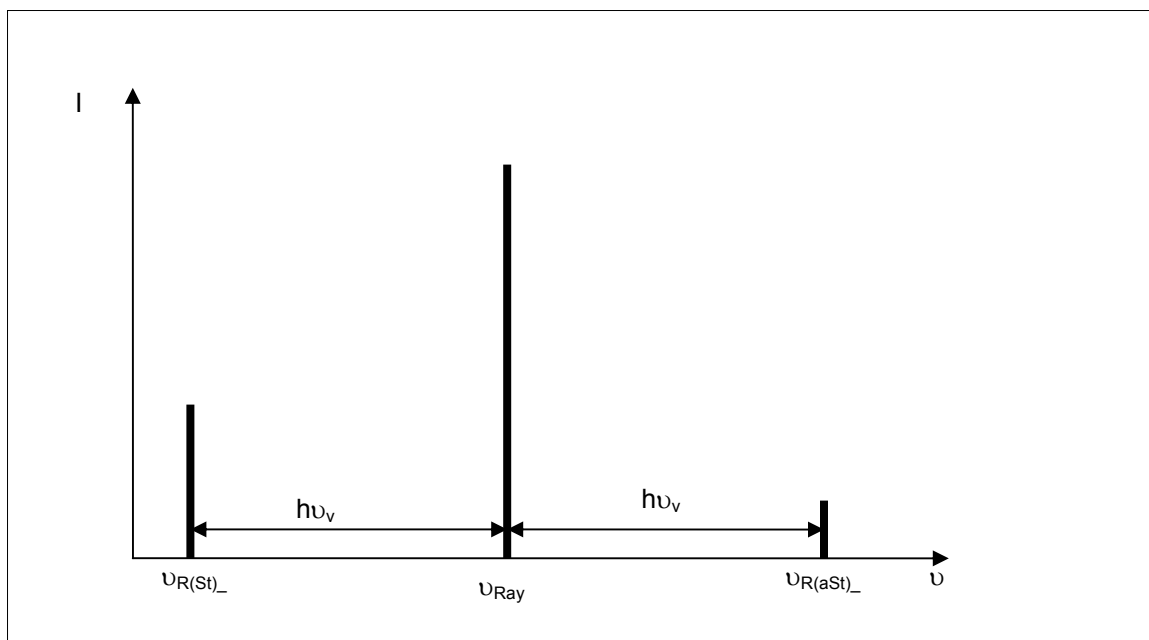


Figure 4.2. Scattering spectrum.

Many of the incident photons will be scattered elastically which gives rise to the very strong Rayleigh line in the center of the spectrum. The frequency ν_{Ray} is the same as the incident frequency, ν_0 . The intensity of the Rayleigh line is $10^3 - 10^4$ times greater than that of the accompanying Raman bands $\nu_{\text{R(St)}}$ and $\nu_{\text{R(aSt)}}$. The difference between the incident, ν_0 , and scattered photon frequencies are the same as the molecular vibration frequency ν_v as follows

$$\begin{array}{ccc}
 h\nu_0 - h\nu_{\text{R(St)}} = h\nu_v & \rightarrow & \nu_0 - \nu_{\text{R(St)}} = \nu_v \\
 h\nu_{\text{R(St)}} - h\nu_0 = h\nu_v & & \nu_{\text{R(St)}} - \nu_0 = -\nu_v
 \end{array}
 \quad (4.2)$$

This shows that the difference between the frequency of the incident versus the scattered radiation is characteristic of the molecule irradiated. The intensity of the anti-Stokes Raman peak is much lower than that of the Stokes peak due to the amounts of the population of molecules occupying ground and excited states at room temperature. For this reason usually the Stokes band is measured.

For comparison Figure 4.3 shows the mechanisms underlying the three most common vibrational spectroscopies, Raman, infrared and fluorimetry.

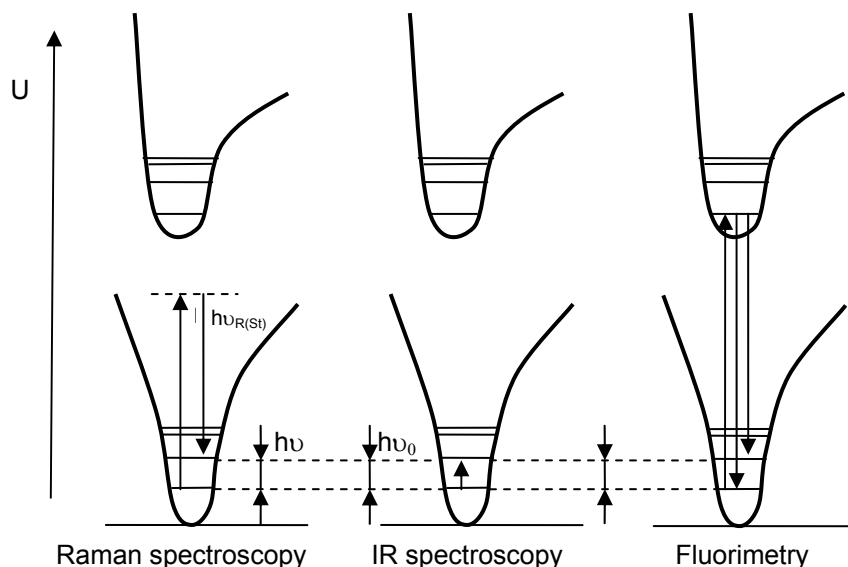


Figure 4.3. Potential energy curves of the ground and first excited states with the transitions observed in Raman spectroscopy, infra – red spectrometry, and Fluorimetry from Barańska.⁷⁷

For Raman scattering we observe

$$h\nu_v = h\nu_0 - h\nu_{R(St)} \quad (4.3)$$

where ν_0 is the incident photon frequency, $\nu_{R(St)}$ is the scattered photon frequency and ν_v is the frequency of molecular vibration.

For Infra-red spectrometry we observe

$$h\nu_v = h\nu_0 = h\nu_{IR} \quad (4.4)$$

where ν_0 the incident beam frequency is equal to the frequency of the absorbed photon ν_{IR} .

For Fluorimetry we observe

$$h\nu_v = h\nu_0 - h\nu_{em} \quad (4.5)$$

where ν_0 is the incident beam frequency and ν_{em} is the frequency of the emitted photon.

For a quantum mechanical treatment of Raman scattering we need to view the molecule as a vibrating dipole. When an electromagnetic wave interacts with

the molecule it induces a dipole moment μ_{ind} in the molecule that is proportional to the electric field strength of the incident radiation \mathbf{E} :

$$\mu_{ind} = \alpha \cdot E \quad (4.6)$$

The proportionality factor α is called the polarizability of the molecule. It is a function of the shape of the molecule and has the dimensions of volume [cm³]. The polarizability can be described as a symmetrical tensor α_{ij} , where $\alpha_{ij} = \alpha_{ji}$.

$$\alpha_{ij} = \begin{bmatrix} \alpha_{xx} & \alpha_{xy} & \alpha_{xz} \\ \alpha_{yx} & \alpha_{yy} & \alpha_{yz} \\ \alpha_{zx} & \alpha_{zy} & \alpha_{zz} \end{bmatrix} \quad (4.7)$$

In Raman scattering the tensor of the polarizability derivative with respect the vibrational normal coordinate Q is most important:

$$\alpha'_{ij} = \left(\frac{d\alpha}{dQ} \right)_0 \quad (4.8)$$

If now an electromagnetic wave with oscillating electric field vector E

$$E = E_0 \cos(2\pi\nu_0 t) \quad (4.9)$$

interacts with a molecule the induced dipole can be written as

$$\mu_{ind} = \alpha E_0 \cos(2\pi\nu_0 t) \quad (4.10)$$

This value varies with time. If the molecule was at 0 K and did not move internally at all, we would only obtain Rayleigh scattering. However the molecule will change its size and shape during the vibrations and therefore the shape of its polarization ellipsoid. This can be represented by

$$\alpha_{ij} = (\alpha_{ij})_0 + \left(\frac{\partial \alpha_{ij}}{\partial Q} \right)_0 Q + \text{higher order terms.} \quad (4.11)$$

Since we do not know the vibrational component of α_{ij} with respect to the normalized vibrational component Q , we represent the value of α_{ij} by expanding the function into a MacLaurin series. Doing this assumes that the displacements of the nuclei are close to zero. The series is also terminated after two terms (harmonic approximation).

The normal coordinate varies during vibration periodically as given by

$$Q_v = A_v \cos(2\pi\nu t). \quad (4.12)$$

The polarizability tensor can then be represented as a matrix

$$(\alpha_{ij}) = \alpha \quad (4.13)$$

(where i, j = x, y, z).

For the normal frequency ν this gives

$$\alpha = \alpha_0 + \left(\frac{\partial \alpha}{\partial Q} \right)_0 A_v \cos(2\pi\nu t) \quad (4.14)$$

Substituting this result leaves us with

$$\mu_{ind} = \alpha_0 E_0 \cos(2\pi\nu_0 t) + \left(\frac{\partial \alpha}{\partial Q_v} \right)_0 A_v E_0 \cos(2\pi\nu_0 t) \cos(2\pi\nu t) \quad (4.15)$$

Using the identity of $\cos \alpha \cos \beta = \frac{1}{2} \cos(\alpha - \beta) + \frac{1}{2} \cos(\alpha + \beta)$ we get

$$\begin{aligned} \mu_{ind} = & \alpha_0 E_0 \cos(2\pi\nu_0 t) + \\ & \frac{1}{2} \left(\frac{\partial \alpha}{\partial Q_v} \right)_0 A_v E_0 \{ \cos[2\pi(\nu_0 - \nu)t] + \cos[2\pi(\nu_0 + \nu)t] \} \end{aligned} \quad (4.16)$$

This shows that the vibrating molecule can be the source three different scattered radiation frequencies.

- ν_0 : frequency unchanged during scattering event (Rayleigh scattering)
- $(\nu_0 - \nu)$: frequency equal to the difference between the incident photon and that of the vibration of the molecule (Raman Stokes scattering)
- $(\nu_0 + \nu)$: frequency equal to the sum of the incident photon and that of the vibration of the molecule (Raman Anti - Stokes scattering)

In all matter the internal vibrations of the molecules can be reduced to a small number of normal vibrations. For non – linear molecules the number of normal vibrations is $3N - 6$ and $3N - 5$ for linear molecules. The Raman activity

of each mode is dependant on the geometry of the molecules themselves, as differentiated by their point groups.

In a molecule the electromagnetic field of the exciting laser couples with the lattice vibrations (phonon field) through the induced dipole moment by the variations in the polarization tensor χ . The polarization tensor is defined as

$$P = \tilde{\chi} E \quad (4.17)$$

Where P is the dielectric polarization and E is the electric field. Given the relations of

$$\begin{aligned} D &= E + 4\pi P \\ D &= E + 4\pi \tilde{\chi} E \\ \text{and} \\ D &= \tilde{\epsilon} E \end{aligned} \quad (4.18)$$

with D being the displacement field and ϵ being the dielectric constant tensor, we derive that

$$\tilde{\epsilon} = 1 + 4\pi \tilde{\chi}. \quad (4.19)$$

This shows the relationship between dielectric constant and polarization. The expansion of the polarization tensor for the nuclear displacement u is

$$\chi_{lm} = \chi_{lm}^{(0)} + \chi_{lm}^{(1)} u + \chi_{lm}^{(2)} u^2 + \dots \quad (4.20)$$

during normal vibrations. Therefore, for a j^{th} normal vibration mode we write

$$u_j = u_{j0} + \exp(i\omega_j t) \quad (4.21)$$

with ω_j being the frequency of vibration for the j^{th} normal mode and

$$\chi_{lm}^{(1)} = \chi_{lmj}^{(1)} = \left(\frac{\partial \chi_{lm}}{\partial u_j} \right)_{u_j=0} \quad (4.22)$$

From the relationship

$$E = E_0 \exp(i\omega_i t) \quad (4.23)$$

we can derive

$$P = \chi^0 E_0 \exp(i\omega_i t) + \chi^1 u_{j0} E_0 \exp[i(\omega_i \pm \omega_j)t] + \chi^2 u_{j0}^2 E_0 \exp[i(\omega_i \pm 2\omega_j)t] + \dots \quad (4.24)$$

The first term describes elastic Rayleigh scattering, in which the energy of the radiation is unchanged. The second term describes first order Raman scattering, involving the derivative of polarization. During this process the incident photon of frequency ω_i and wave vector k_i transitions from an initial state (n, v) (n : electronic quantum number, v : vibrational quantum number) through an intermediary state (n', v') to a final state $(n, v+1)$ in such a way that energy and momentum are preserved. This requires the creation or annihilation of a phonon (ω_j, q_j) and the emission of a photon of different frequency and wavevector (ω_s, k_s)

$$\begin{aligned} \eta\omega_s &= \eta\omega_i \pm \eta\omega_j \\ \eta k_s &= \eta k_i \pm \eta q_j \end{aligned} \quad (4.25)$$

The + sign denotes anti – Stokes Raman scatter and the – sign stands for Stokes Raman scatter.

These relationships show the interaction of the Raman effect with lattice vibrations in solids and they are the basis of the characterization of solid matter via Raman spectroscopy.

4.2.2 Confocal Micro Raman Spectroscopy

Confocal Micro Raman Spectroscopy is a successful mating of a conventional Laser Raman instrument with a microscope. The use of the microscope allows Raman spectra to be taken from very small areas, down to 200 nm in lateral resolution. Figure 4.4 shows how this is achieved. A beam splitter allows the same objective used in focusing the beam to collect the sample information. This reflected beam is then focused onto a pinhole, which ensures that only the Raman light taken from the focus plane and a small area of the center of the laser beam will reach the detector. The instrument is also capable of scanning the laser across the sample by using the piezo controlled mounting

stage. This allows the instrument to capture Raman images, by scanning the beam across the sample.

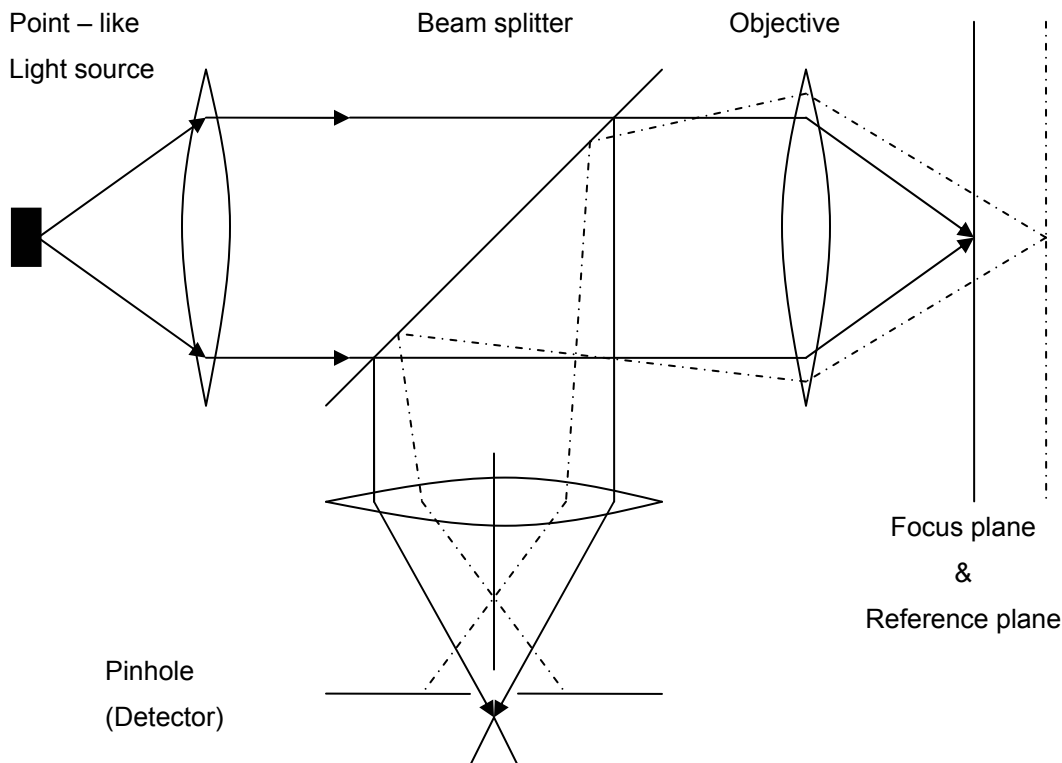


Figure 4.4. Principal setup of a confocal microscope.⁴

The CRM 200 uses a single mode optical fiber to deliver the laser beam to the sample. The single mode fiber only supports a single transversal mode (LP_{01}) to be focused onto the sample. The reflected light is captured with the same objective and transmitted through a multi – mode optical fiber to the spectrometer. The spectrometer contains both a CCD detector and a photon counting APD. The core of the multi mode fiber acts a pinhole in continuation of the mechanical pinhole.

4.2.3 Raman Spectroscopy of Borate Glasses

(For all referenced borate groups see Figure 4.7)

Some of the earliest Raman work on borate glasses was done by Konijnendijk and Stevels in 1975.⁵ They primarily investigated single and mixed alkali borate glasses with up to 50 mol% alkali content. The most consistent feature noted by the authors is the appearance of a sharp peak at ca. 806 cm^{-1} , which they assigned to the breathing mode of the boroxol ring group B_3O_6 . This is the only feature they noted in vitreous B_2O_3 . As alkali is added to the glass the boroxol rings are converted to other groups, and the peak at 806 cm^{-1} disappears at about 25 wt.% alkali for binary alkali borate glasses. At the same time as the boroxol rings are being converted a peak at 770 cm^{-1} appears which is attributed to the formation of a six – membered borate ring with one BO_4 group according to the reactions shown in Figure 4.5.

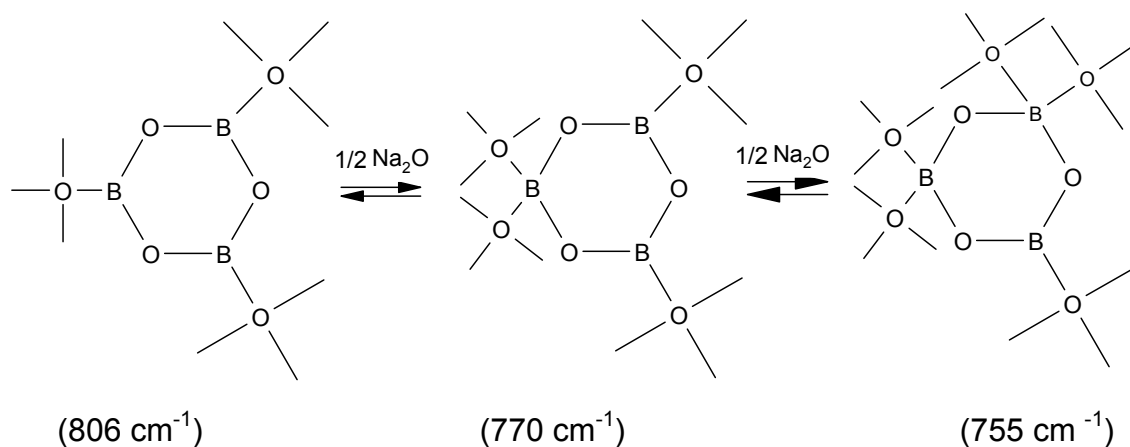


Figure 4.5. Conversion of boroxol ring.⁸⁰

Following further additions of alkali the ring structure decomposed more and more until at 45 wt% alkali the ring was resolved into several simpler structures as shown in Figure 4.6.

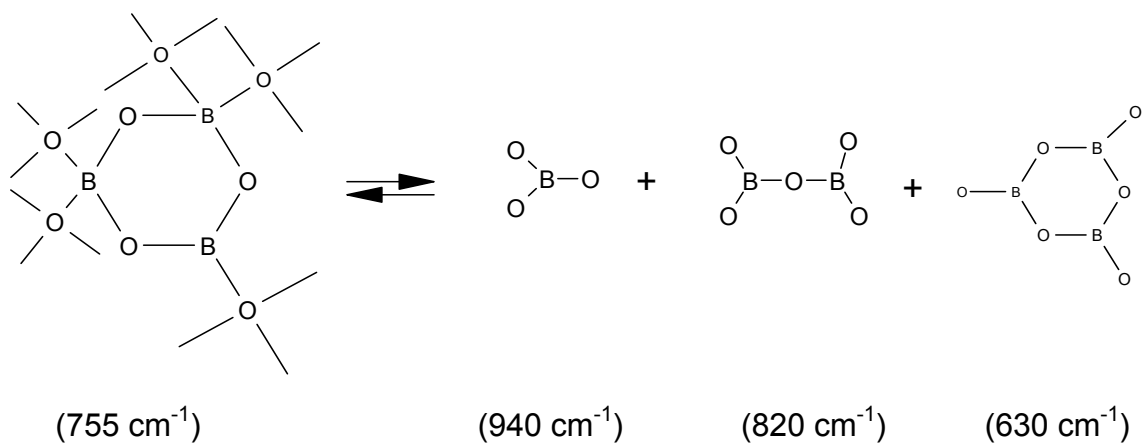
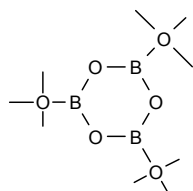
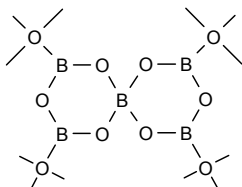


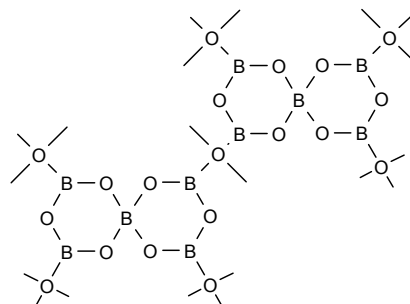
Figure 4.6. Further conversion of boroxol ring.⁸⁰



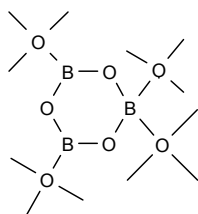
Boroxol ring



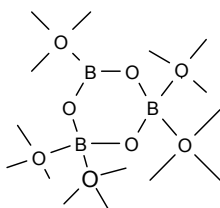
Pentaborate group



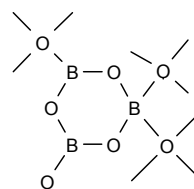
Tetraborate group



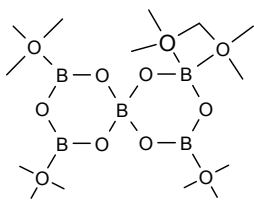
Triborate group



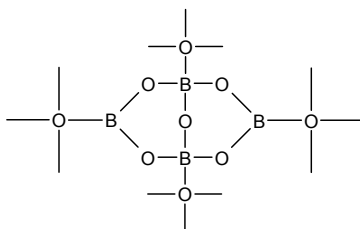
Di-triborate group



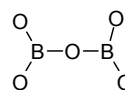
Triborate group with one non-bridging oxygen



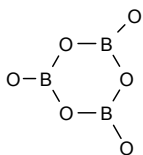
Dipentaborate group



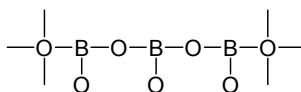
Diborate group



Pyroborate group



Ring - type metaborate group



Chain - type metaborate group



Orthoborate group

Figure 4.7. Type of borate groups occurring in glasses, derived from analog groups in crystalline compounds. After Konijnendijk et al.⁸⁰

The authors also found similar conversions in borate glasses when adding alkaline earths to vitreous boron oxide.

In a later work Galeener⁶ was able to predict the formation of planar rings in glasses theoretically by using an energy minimization argument. He was able to predict a 3 fold planar ring in vitreous B₂O₃ and other intermediate range order in several other glasses.

Yano et al.⁷⁻⁹ also systematically investigated sodium borate glasses via Raman spectroscopy. Their results are similar to those presented.

Other authors also examined the alkali borate system. Kamitsos et al.¹⁰⁻¹⁴ examined cesium, rubidium, potassium, sodium and lithium borate glasses with up to 70 mol% alkali content. For less than 20 mol% alkali they observed a band at 803 cm⁻¹ that indicates the presence of boroxol rings. This band decreased in favor of a band at 767 cm⁻¹ as alkali content increased suggesting the presence of boroxol rings containing one BO₄ tetrahedron. Other features observed were bands at 675 and 625 cm⁻¹, which the authors attribute to chain metaborates of the type (BØ₂O⁻)_n as first suggested by Konijnendijk and Stevels.⁵ These peaks were first observed at about 10 mol% alkali and became more pronounced at higher alkali concentrations. A strong band at 605 cm⁻¹ was assigned to ring type metaborate units on the basis of comparison with the Raman spectra of the crystalline compound. Another feature shown was a broad band centered at about 1500 cm⁻¹ that increased in intensity with increasing alkali content and was also assigned to the creation of ring type metaborate groups on the basis of comparison with the crystalline compounds. Other bands in the 500 – 900 cm⁻¹ region were assigned to complex ring type structures containing BO₄ tetrahedra in various arrangements. An exact assignment of bands to structures was almost impossible due to the very complex nature of the structures. The matter was complicated by the formation of non-bridging oxygen bonds at higher alkali concentrations. Bands centered at 545 and 900 cm⁻¹ could be assigned to BO₄ tetrahedra that do not participate in any other structural grouping in the glass. For alkali contents of above 45 mol% two characteristic bands were observed at 795 and 1240 cm⁻¹. The 795 cm⁻¹ band was assigned by the authors to the

symmetric stretching motion of the B – O – B bond, and the 1240 cm^{-1} band to the stretching motion of the B – O⁻ terminus of the $\text{B}_2\text{O}_5^{4-}$ group.

A review paper by Meera and Ramakrishna¹⁵ examined the Raman spectra of up to ternary borate glasses, concentrating on binary alkali borates. They summarized the literature of alkali borate glasses containing up to 40 mol% alkali; in the case of Na_2O up to 70 mol% and for Li_2O up to 60 mol%. In all cases the spectra of all alkali glasses were very similar below 10 mol% alkali, with the 806 cm^{-1} band being the defining feature. As alkali is added a band at 770 cm^{-1} appeared and shifted towards lower frequencies as the alkali content is increased. Konijnendijk⁵ assigned, in his paper, the 770 cm^{-1} band to tetraborate groups and the lower frequency band at 755 cm^{-1} to diborate groups. He also assigned other bands to various structures; orthoborate to the 940 cm^{-1} band, pyroborate to 820 cm^{-1} , ring type metaborate to 630 cm^{-1} , and chain type metaborate to 730 cm^{-1} . Bril on the other hand assigned the 770 cm^{-1} band to the symmetric breathing mode of a six membered ring containing one BO_4 tetrahedron and the down shifted band to a six membered ring containing two BO_4 groups. Akagi¹⁶ et al. examined potassium borate glasses and melts and their findings match those of other authors.

One paper by Irion¹⁷ et al. questioned the assignment of the 755 cm^{-1} band to the diborate group. They examined zinc borate and lithium borate glasses, which exhibit no band at 750 cm^{-1} , but contain diborate groups. Based on this evidence it is now accepted that the presence of diborate groups is identified by a band at 1100 cm^{-1} .^{10-14,17}

Analysis of the literature by Meera et al.²⁰ led them to the conclusion that the occurrence of pentaborate groups is indicated reliably only by the simultaneous presence of bands at 930 , 770 , 650 cm^{-1} and 500 cm^{-1} . This was based on comparisons with crystalline compounds. Incorporating a second BO_4 tetrahedron into the pentaborate group lead to a di-pentaborate group, which occurred at high alkali content,^{11,13,14} and was characterized by a band at 755 cm^{-1} .

For cesium borate glasses Kamitsos et al.¹⁰ assigned bands at 725, 675 and 625 cm⁻¹ to chain – type metaborates based on comparisons with crystalline CaO – B₂O₃ and Li₂O – B₂O₃, which were known to contain chain – type metaborate groups. Based on further examination, the band at 625 cm⁻¹ persisted after the alkali content is above 25 mol%, which lead Meera to conclude that the 625 cm⁻¹ band should not be assigned to chain – type metaborates, but rather together with bands at 900 and 700 cm⁻¹ to pentaborate groups.

Based on the studies, mainly, of Kamitsos^{10-12,14} and his co-workers, Meera and Ramakrishna¹⁵ tabulated the occurrence of various structural groups in alkali borate glasses. This can be seen in Table 4.I.

Table 4.I: Types of Borate Groups Occurring in Alkali Borates²⁰

Glass Examined region	Li ₂ O : B ₂ O ₃ 0 ≤ x ≤ 65	Na ₂ O : B ₂ O ₃ 0 ≤ x ≤ 75	K ₂ O : B ₂ O ₃ 0 ≤ x ≤ 45	Cs ₂ O : B ₂ O ₃ 0 ≤ x ≤ 50	Rb ₂ O : B ₂ O ₃ 0 ≤ x ≤ 45
Boroxol	0 ≤ x ≤ 26	0 ≤ x ≤ 25	0 ≤ x ≤ 25	0 ≤ x ≤ 25	0 ≤ x ≤ 25
Pentaborate	0 ≤ x ≤ 36	0 ≤ x ≤ 25	0 ≤ x ≤ 30	0 ≤ x ≤ 30	0 ≤ x ≤ 30
Di-Pentaborate	36 ≤ x ≤ 65	34 ≤ x ≤ 71	30 ≤ x ≤ 45	30 ≤ x ≤ 50	30 ≤ x ≤ 45
Diborate	20 ≤ x ≤ 65	25 ≤ x ≤ 40	25 ≤ x ≤ 42	25 ≤ x ≤ 50	25 ≤ x ≤ 40
Ring – type metaborate	46 ≤ x ≤ 65	35 ≤ x ≤ 67	30 ≤ x ≤ 45	30 ≤ x ≤ 50	30 ≤ x ≤ 45
Chain – type metaborate	-	-	42 ≤ x ≤ 45	14 ≤ x ≤ 20	-
Isolated diborate	41 ≤ x ≤ 65	45 ≤ x ≤ 65	-	-	-
'Loose' B ₄ units	-	45 ≤ x ≤ 65	-	40 ≤ x ≤ 50	-
Pyroborate	49 ≤ x ≤ 65	45 ≤ x ≤ 71	-	-	-
Orthoborate	56 ≤ x ≤ 65	61 ≤ x ≤ 75	-	X = 50	-

Soppe et al.¹⁸ also examined the lithium borate system. Their results confirmed the most prominent features being the 806 cm⁻¹ band, assigned to boroxol rings, and the 770 cm⁻¹ band, assigned to six-membered rings containing one BO₄ unit.

Lorösch et al.¹⁹ pointed out that the cation does have an effect on the network. They examined the Raman spectra of different alkali borate glasses containing a constant percentage of alkali. Chryssikos et al.²⁰ also confirmed this in their study. These studies showed that the intensity of the 806 cm⁻¹ boroxol band decreased faster in the larger alkali glasses, especially the cesium glass. The suggested reason was the formation of pentaborate and BO₂⁻ groups in the

cesium glass and triborate groups in the lithium glass. As alkali content increased above 20 mol%, the 770 cm^{-1} band shifted towards lower frequency due to the formation of six membered rings containing two BO_4 tetrahedra.^{10-14,20} For example at an alkali content of 35 mol% the band shifted to ca. 775 cm^{-1} in the cesium glass, whereas no shift occurs in the lithium glass. With further increasing alkali content, the shifted band disappeared, indicating a disruption of the six – membered rings. This resulted in chain – and ring – type metaborates being formed. This disruption was stronger in the cesium glass than in the other alkali glasses, as was seen in the lower intensity of the 755 cm^{-1} bands.^{10,13,20} The limiting concentrations for the formation of these chain – and ring – type metaborates was highest in the lithium glass, formation starting at 56 mol% alkali, and lowest in cesium glass, formation starting at 15 mol%.^{10,13} Glasses containing 45 mol% potassium or rubidium contained mainly chain – type metaborates, whereas a glass containing 45 mol% cesium contained mainly ring – type metaborates.¹⁰ In sodium and lithium borate glasses with 65 mol% alkali content, mainly orthoborate and pyroborate groups were present.

Maniu et al.²¹⁻²⁴ examined potassium borate glasses with the composition $x\text{ MO} \cdot (1-x)[3\text{ B}_2\text{O}_3 \cdot \text{K}_2\text{O}]$. Metal oxides used were up to $x = 50$ of TiO_2 , CuO and V_2O_5 . They found that even with small additions ($x \approx 0.03$) of metal oxide boroxol rings were broken and orthoborate groups were formed. For $x > 0.1$ TiO_2 , ring – type metaborates and ‘loose’ BO_4 tetrahedra are formed. All glasses showed a small amount of chain – type metaborates and pyroborate groups.

Soppe et al.¹⁸ were able in their paper to show a relationship between the mixed alkali effect in their lithium – cesium – borate compositions and the intensity ratio of the 806 and 770 cm^{-1} peaks.

Hassan et al.²⁵ examined the boson peak in their paper and tried to relate its properties to the fragility parameter of the alkali borate glasses they examined. They obtained the correlation length for their glasses and found that it decreased as the concentration of modifier oxide increases. They equated increasing modifier content with increased fragility. The correlation length was a measurement of disorder and was defined as $l_c \approx v / v_m$ (v = sound velocity, v_m =

boson peak frequency). They also found that the strength of the decrease in correlation length corresponds to the increase in fragility as they go from $K \rightarrow Na \rightarrow Li$. Higher temperature studies showed that the decrease of l_c accelerates as the temperature was increased above T_g .

Systematic investigations of alkaline earth borate glasses are relatively rare. Maniu²⁶ investigated calcium borate glasses containing 20 to 80 mol % CaO. The authors noted the presence of boroxol rings (band at 802 cm^{-1}) in glasses with less than 30 mol% CaO. As calcium content increased to 30 mol% the boroxol band diminished and was replaced by a band at 770 cm^{-1} . This indicated the conversion of boroxol rings into six – membered rings containing one boron tetrahedron. Together with bands at appearing 890 and 667 cm^{-1} this indicates pentaborate groups were present. Above 30 mol% calcium oxide content an orthoborate band appeared at 930 cm^{-1} and slowly shifted to 922 cm^{-1} at 80 mol% CaO (1050 cm^{-1} band indicating diborate groups was absent). At all examined calcium contents a band at 735 cm^{-1} was present. The intensity of this band increased strongly as the calcium content increased. This band was assigned to chain type metaborates. As calcium content increased above 60 mol%, ring – type metaborate groups appeared, as indicated by a band at 608 cm^{-1} . The high frequency band of pyroborate groups at 1247 cm^{-1} was present all throughout the composition range examined. It slowly increased in intensity as the modifier content was increased and also shifted slowly to lower wavenumbers (1216 cm^{-1} at 80 mol% CaO).

The magnesium borate glasses were examined by Kamitsos¹² over the glass forming region (44 – 54 mol%). The strongest feature of the spectra was the 806 cm^{-1} band indicating the presence of boroxol rings at 44 mol% MgO. As MgO content increased the boroxol band diminished, disappearing completely at 50 mol%, and the 785 cm^{-1} band became stronger. This band was attributed to six-membered rings containing one BO_4 unit. Konijnendijk²⁷ examined several ternary glass compositions in the $\text{MO} - \text{Na}_2\text{O} - \text{B}_2\text{O}_3$ system, with $M = \text{Mg, Ca}$. His results coincided with those of Kamitsos¹² for the magnesium borate.

Konijnendijk^{5,27,28} and Tang²⁹ examined barium borate glasses. The spectra are similar to those present in alkali borate glasses. Konijnendijk found that the 20 mol% barium containing glass did not exhibit the boroxol band at 806 cm^{-1} , whereas Tang found the same glass to show this peak. The discrepancy was not explained.

4.2.4 Raman Studies of Heavy Metal Containing Borate Glasses

Chryssikos et al.³⁰ examined cadmium borate glasses. Those glasses showed a characteristic peak at 1385 cm^{-1} . This peak increased in intensity as the cadmium content increased and was indicative of a triangular boron – oxygen stretch involving non-bridging oxygen. This peak showed a shoulder at 1230 cm^{-1} and together with a band at 830 cm^{-1} showed the existence of pyroborate units. A band at roughly 935 cm^{-1} showed a low compositional dependence and was assigned to orthoborate groups. The small 660 cm^{-1} band showed the presence of metaborate groups. The cadmium borate glasses showed bands at 806 cm^{-1} and 775 cm^{-1} which were assigned to boroxol rings and six-membered rings with one BO_4 unit, respectively. This was where the cadmium borate glasses showed differences to alkali borate glasses. Both bands diminished slowly as the cadmium content increased, whereas in alkali borate glasses the 775 cm^{-1} band would grow at the expense of the 806 cm^{-1} band. In cadmium glasses however, the disappearance of boroxol rings gave rise to six-membered rings with two BO_4 units at cadmium contents higher than 44 mol%

Meera et al.³¹ measured Raman spectra of lead borate glasses with 22 – 85 mol% lead. Konijnendijk²⁸ also showed a Raman spectrum for lead borate glass containing 20 mol% lead. His results were similar to those of Meera and coworkers. Lead borate glasses exhibit a strong peak at 806 cm^{-1} that was associated with the presence of boroxol rings and disappeared completely at 35 mol% lead. Also present was a peak at 775 cm^{-1} , indicating the presence of six-membered rings with one boron tetrahedron. This peak shifted to lower

frequencies and decreased as lead content increased and disappeared between 45 and 50 mol% lead. This shift was caused by the inclusion of one more boron tetrahedron into the six-membered rings. The presence of a band at 900 cm^{-1} allowed the six-membered ring to be assigned to pentaborate groups. The decrease, coupled with the increase of a band at 710 cm^{-1} , indicated a conversion of the ring type compounds into chain type metaborate units. Growing bands at 1050 and 950 cm^{-1} showed an increasing amount of diborate groups in the glasses as the lead content increased. The authors suggested that the formation of diborate groups slowed down the consumption of boroxol rings, allowing them to exist up to lead concentrations of 35 mol%. They suggested this occurred due to the ability of PbO to act as a network former as well as a network modifier. Other authors^{12,30} had noted the same behavior in cadmium and magnesium borate glasses. A PbO content above 50 mol% sees the diminishment of the 1050 cm^{-1} peak and the growth of a peak at 620 cm^{-1} , which was assigned to metaborate groups. As the lead content increased even further, a peak at 550 cm^{-1} began developing and growing. This peak was assigned to 'loose' diborate groups. For very high lead contents above 70 mol% peaks at 820 cm^{-1} and 1230 cm^{-1} appeared and they were assigned to pyroborate units. This indicated the back – conversion of B_4 into B_3 units contained in pyroborate. The lead ions in lead borate glasses were also shown to change their nature as lead content increases in the glass series. At low lead content the Pb – O bond was known to be ionic in nature, but as the lead content increases the bond became more covalent in nature. In the spectra this could be seen by the shift of the high frequency band at 1350 cm^{-1} , which was assigned to the B – O⁻ vibration, to lower frequencies around 1180 cm^{-1} .

Lines^{32,33} showed theoretical calculations and experimental results for the absolute Raman intensities of germania based heavy metal oxide glasses in his papers. He examined germanate glasses containing tellurium, lead, bismuth and antimony and he was able to classify four regions in their Raman spectra. He noted 1) acoustic Raman modes, 2) heavy metal ion vibrations, 3) bridging – anion modes and 4) non – bridging anion modes. He classified acoustic Raman

scattering as a not wave – vector conserving process which was only allowed in glasses, due to the absence of long – range translational symmetry. Heavy metal ion vibration modes were resultant from the vibrations of only heavy metal ions by themselves. (Covalently) bridged – anion modes resulted from symmetric stretching modes, such as the Si – O – Si bridges in fused silica. Non (covalently) – bridged anion modes resulted from either unbridged anions such as the stretching mode of the terminal oxygen ($P = O$) in P_2O_5 glass. In multi – component glasses, this class of modes could also result from asymmetric cation – anion – cation' stretches, in which the two cations were different. An example would be the Si – O – Na configuration in sodium silicate glasses. These regions of modes were also arranged in order of appearance in the spectra the author examined in his papers.

Kharlamov et al.³⁴ examined heavy metal containing gallate glasses containing varying amounts of lead and bismuth, up to 90 mol% modifier. They were able to classify the resulting Raman spectra as containing four regions according to Lines' model.^{32,33} They found low – frequency Raman modes from $30 - 70\text{ cm}^{-1}$, heavy metal ion vibration modes from $120 - 140\text{ cm}^{-1}$, bridging anion modes from $300 - 600\text{ cm}^{-1}$ and non – bridging anion modes from $600 - 700\text{ cm}^{-1}$ in their spectra. They noted the super position of modes resulting from Ga – O – Ga and Bi – O – Bi modes in the bridging anion regime between 500 and 600 cm^{-1} . They also associated a shoulder at $590 - 630\text{ cm}^{-1}$ with a non – bridging Ga – O⁻ stretching vibration and a further weak band at $660 - 700\text{ cm}^{-1}$ with a Bi – O⁻ stretching vibration in BiO_6 octahedra.

Baia et al.³⁵ studied bismuth borate glasses doped with 0.5 mol% CuO (95% $[x\text{ B}_2\text{O}_3 (1-x)\text{ Bi}_2\text{O}_3]$ 5% Fe_2O_3). They examined glasses with a range of x from $x = 0.07 - 0.90$. Infrared and Raman instruments were used in this study before and after the samples were all subjected to a heat treatment cycle. For samples with $x \leq 0.20$ they noted the absence of the characteristic band of $[BiO_3]$ tetrahedral in the infrared spectrum and concluded that therefore the glasses must be composed only of $[BiO_6]$ octahedra. In the Raman spectra they noted peaks in the $70 - 160\text{ cm}^{-1}$ region, which were due to heavy metal ion vibrations,

as noted earlier by Miller.³⁶ A peak at 82 cm^{-1} was due to acoustic vibrations because its position was not dependent on composition and its intensity increased with increasing bismuth content. Based on work by Kharlamov,³⁴ the authors assigned a peak at 123 cm^{-1} and a shoulder at 152 cm^{-1} to the presence of $[\text{BiO}_6]$ octahedral and peaks at 262 and 516 cm^{-1} , plus a shoulder at 328 cm^{-1} to the presence of $[\text{BiO}_3]$ tetrahedra. A very weak shoulder at 620 cm^{-1} was attributed to the stretching motion of the non – bridging $\text{Bi} - \text{O}^-$ arrangement in the $[\text{BiO}_6]$ octahedral units. After heat treatment all glasses with bismuth contents larger than 80 mol% ($x \leq 0.20$) crystallized. Crystallization was not total and the only identified phase was $\text{Bi}_{24}\text{B}_2\text{O}_{39}$. The Raman spectra showed a new band at 198 cm^{-1} which the authors ascribed to the $\text{Bi} - \text{O} - \text{Bi}$ vibration in $[\text{BiO}_3]$ and $[\text{BiO}_6]$ polyhedra. With the exception of a band at 516 cm^{-1} , attributed to the $\text{Bi} - \text{O}^-$ stretching motion, which shifts to 530 cm^{-1} upon heat treatment, all other bands were unaffected. This shift could be explained by the fact that in heat treated samples the $\text{Bi} - \text{O} - \text{Bi}$ vibration the band was attributed to can occur in either linked $[\text{BiO}_3]$ tetrahedra or in the arrangement of one $[\text{BiO}_3]$ tetrahedron to one $[\text{BiO}_6]$ octahedron. This was supported by the observation that for the $x = 0.30$ sample this band was observed at roughly the same position, 522 cm^{-1} , as in the untreated sample with $x = 0.20$, where only $[\text{BiO}_6]$ polyhedra occur in the glass.

For glasses with $x \geq 0.30$ the authors observed broad bands in the $50 - 180\text{ cm}^{-1}$ region, which they attributed to the presence of Bi^{3+} ions in $[\text{BiO}_6]$ octahedra. These bands broadened as x increases (bismuth content decreased) and the authors attributed this to an increasing distortion of the octahedral units. The weak Raman shoulder at 328 cm^{-1} , caused by the $\text{Bi} - \text{O} - \text{Bi}$ vibration, shifted to 380 cm^{-1} at $x = 0.30$. The weak shoulder at 612 cm^{-1} , which is due to the vibrations of $\text{B} - \text{O}^-$ non – bridging oxygens and typical for metaborate groups (both ring and chain type), increased in intensity as bismuth content decreased. As x grew larger, a shoulder at 720 cm^{-1} appeared, which indicated the presence of metaborate groups. Another band at 1216 cm^{-1} appeared and was linked with $\text{B} - \text{O}^-$ vibrations. After heat treatment the bands present in the samples

broadened indicating a higher degree of disorder in the samples. The band at 326 cm^{-1} shifted to higher wave numbers, which the authors linked to an increasing distortion of the $[\text{BiO}_6]$ tetrahedral that make up the structure of the glasses. At very low bismuth concentrations ($x = 0.90$), there appeared a band at 806 cm^{-1} , that showed the presence of boroxol rings.

These authors, Baia et al.,³⁷ also examined copper doped bismuth borate glasses with the formula $99.5\% [x\text{ B}_2\text{O}_3 (1-x)\text{ Bi}_2\text{O}_3]$ $0.5\% \text{ Fe}_2\text{O}_3$ and a range of $x = 0.07 - 0.625$. All glasses were measured in infrared and Raman spectroscopy before and after heat treatment. Strong bands at 135 and 155 cm^{-1} were noted and increased in intensity as the bismuth content increased. At $x = 0.07$ only, a band at 320 and 859 cm^{-1} and shoulders at 236 and 420 cm^{-1} could be observed. As bismuth content increased, these bands became convoluted under a large shoulder that decreased in intensity. A band at 1405 cm^{-1} was present at all concentrations and became shifted towards lower wave numbers as bismuth content decreases. A shoulder at 1220 cm^{-1} could be observed at the same intensity for all compositions except for $x = 0.625$ where the intensity was reduced. For $x \geq 0.20$ a very small broad band at 910 cm^{-1} and a shoulder at 730 cm^{-1} were observed. After heat treatment, samples with $0.07 \leq x \leq 0.33$ exhibited bands and shoulders at $129, 144, 205, 274, 328, 460, 537$ and 622 cm^{-1} . All these bands decreased in intensity as bismuth content decreased. At $x = 0.40$ these bands broadened and at $x = 0.625$ only the bands at 139 and 159 cm^{-1} could be clearly distinguished. Raman spectra could be classified into the four groups according to Lines.^{32,33} 1) low wave number modes (less than 100 cm^{-1}), 2) heavy metal ion vibrations ($70 - 160\text{ cm}^{-1}$), 3) bridged – anion modes ($300 - 600\text{ cm}^{-1}$) and 4) non – bridged anion modes (more than 600 cm^{-1}). The authors noted the presence of bands in the last three categories, and the authors interpreted this as a confirmation of the network forming character of the Bi^{3+} ions. At very high bismuth concentrations ($x = 0.07$) the band observed at 135 cm^{-1} indicated the presence of both $[\text{BiO}_3]$ and $[\text{BiO}_6]$ units. At this high bismuth content the bands at $320, 584$ and 1405 cm^{-1} and shoulders at 236 and 472 cm^{-1} could be assigned as follows. The $\text{Bi} - \text{O} - \text{Bi}$ vibration was responsible

for the bands at 320, 472 and 584 cm^{-1} , whereas the Bi – O⁻ vibration was responsible for the shoulder at 236 cm^{-1} . The shoulders at 1323 and 1490 cm^{-1} and the band at 1405 cm^{-1} , which appeared only for very high bismuth content could be attributed to B – O⁻ vibrations of units attached to large segments of the borate network. The intensity of the signal in the 1300 – 1500 cm^{-1} range decreased with increasing boron content. This was also noted by other authors^{10,31} in their studies. The band at 1405 cm^{-1} strongly shifted toward smaller wave numbers as x increases indicating the strong influence of bismuth oxide on the structure of the glasses. The evolution of the band at 155 cm^{-1} was connected with the distortion of the [BiO₆] groups. When the octahedra were not distorted, at very high bismuth content, the band appeared only as a small shoulder, but as bismuth content decreased, the shoulder evolved into a distinct band. Broad shoulders centered at 390 and 580 cm^{-1} were attributed to Bi – O and Bi – O – Bi vibrations in distorted linked [BiO₆] octahedra³⁴ and the weak shoulder at 730 cm^{-1} could be assigned to chain type metaborate groups.¹⁰ The heat treated samples were mostly crystalline and the spectra reflect this.

4.3 Experimental Procedure

A number of fibers were examined in a confocal Raman microscope^k. The microscope consists of a 532 nm laser, whose light was focused through an optical fiber into a microscope with a 100x Leitz objective. The reflected light was analyzed by a Peltier – cooled CCD detector and processed with the custom software of the instrument.

The laser was focused onto a single fiber and a spectrum was taken with a 600 lines/mm grating and an integration time of 5 sec. The laser was carefully aligned with the center of the fiber and the focus plane was carefully set to the center of the fiber. All fibers were cut to be shorter than the cover slide they lay on to prevent bowing of the fibers.

To achieve comparable spectra the experimental parameters were not changed between measurements.

The fibers were arranged in the microscope as shown in Figure 4.8. The red circle represents the location of the laser dot.

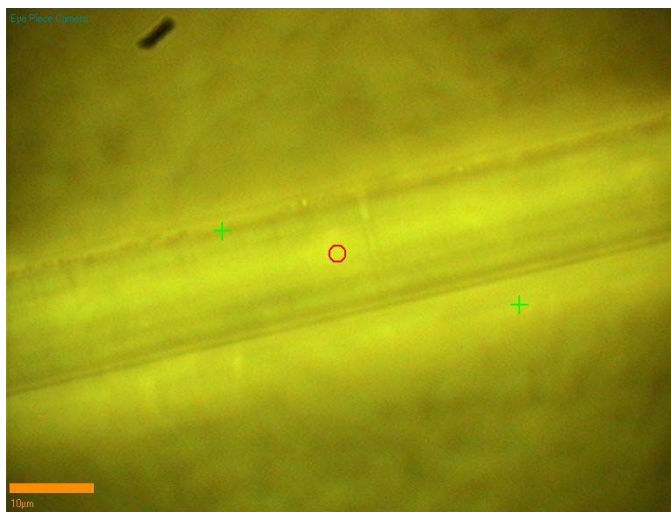


Figure 4.8. Bright field image of a glass fiber drawn at $T = 525^{\circ}\text{C}$, $S = 3.5 \text{ m/s}$.

^k WiTec CRM 200

4.4 Results

A sample Raman spectrum is shown in detail in Figure 4.9. As can be seen in Figure 4.10 to Figure 4.12, the spectra of all glass fibers measured were similar to the one shown in Figure 4.9. The spectrum shows several distinct features. There is a broad peak region ranging roughly from 120 – 700 cm^{-1} . Within this region several peaks stand out. Distinct bands can be observed at 165, 365, 490, 660, 1320 and 2450 cm^{-1} .

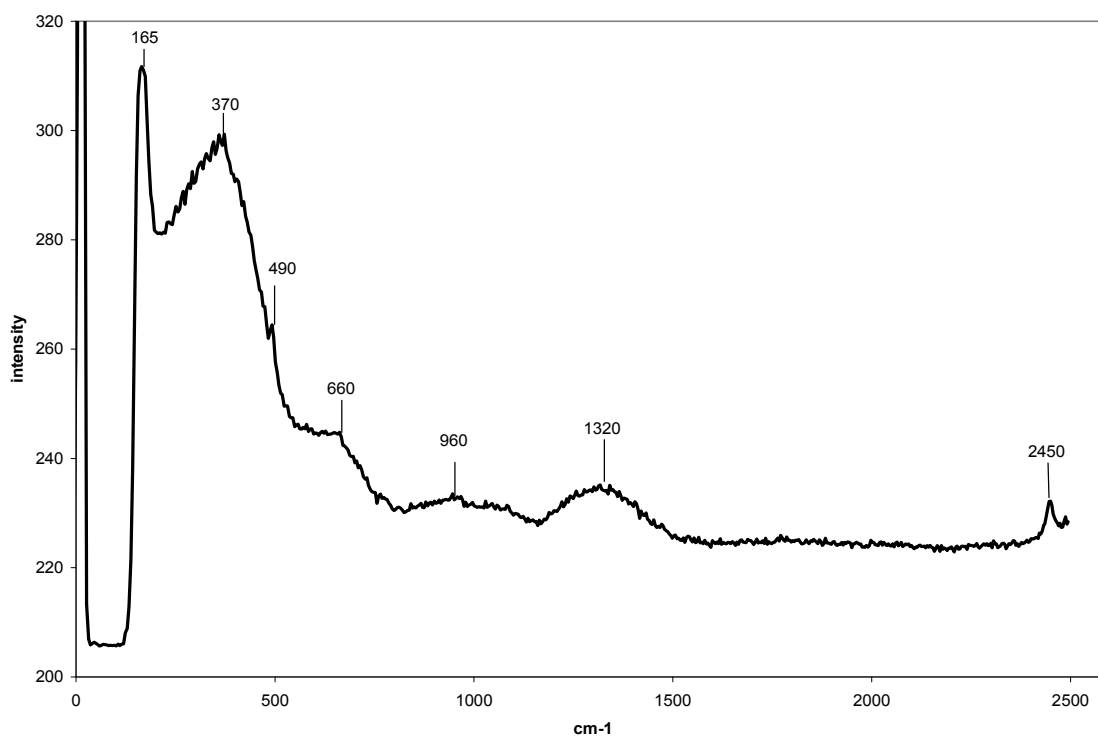


Figure 4.9. Raman spectrum of a 0.25 Bi_2O_3 – 0.75 B_2O_3 glass fiber drawn at $T = 575^\circ\text{C}$ and a draw speed of 8 m/s.

The spectra will be examined in detail below.

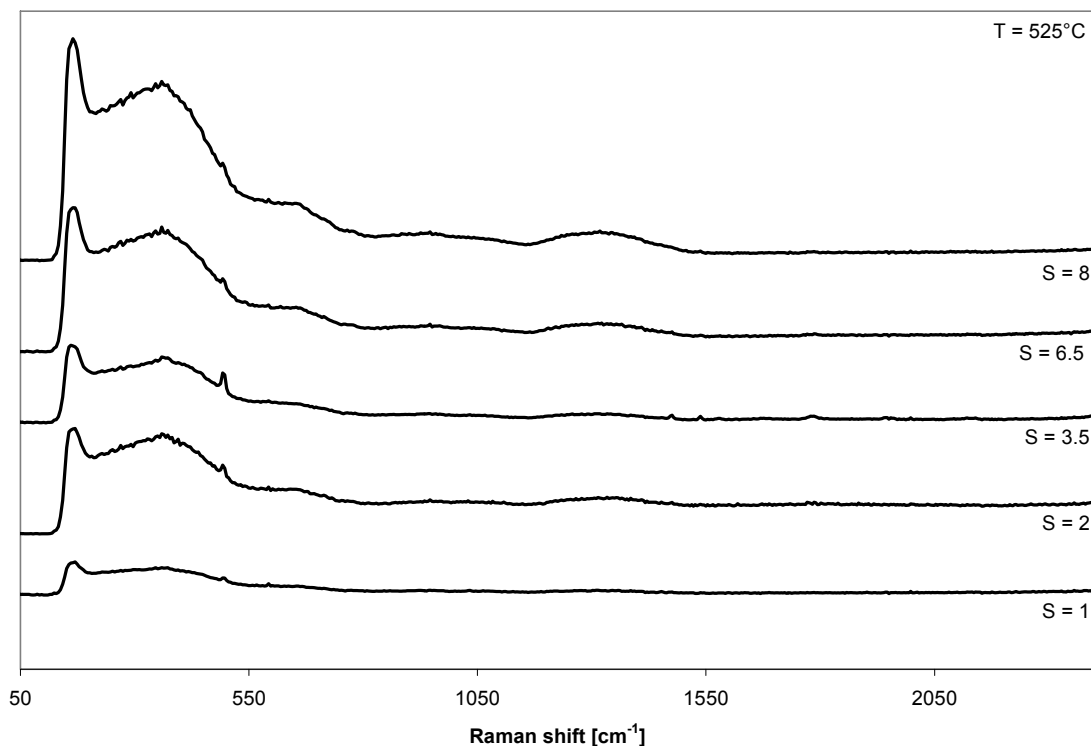


Figure 4.10. Raman spectra of fibers drawn at $T = 525^{\circ}\text{C}$, drawing speeds as shown.

For fibers drawn at a temperature of 525°C , the peaks at 165 and 370 cm^{-1} become stronger the higher the drawing speed. The shoulder at 490 cm^{-1} however shows a high intensity only for a middle drawing speed of 3.5 m/s and then decreases again in intensity. The weak band at 660 cm^{-1} shows a slight increase in intensity as drawing speed increases, as does the broad band at 1320 cm^{-1} . The band at 960 cm^{-1} does not show a change with drawing speed.

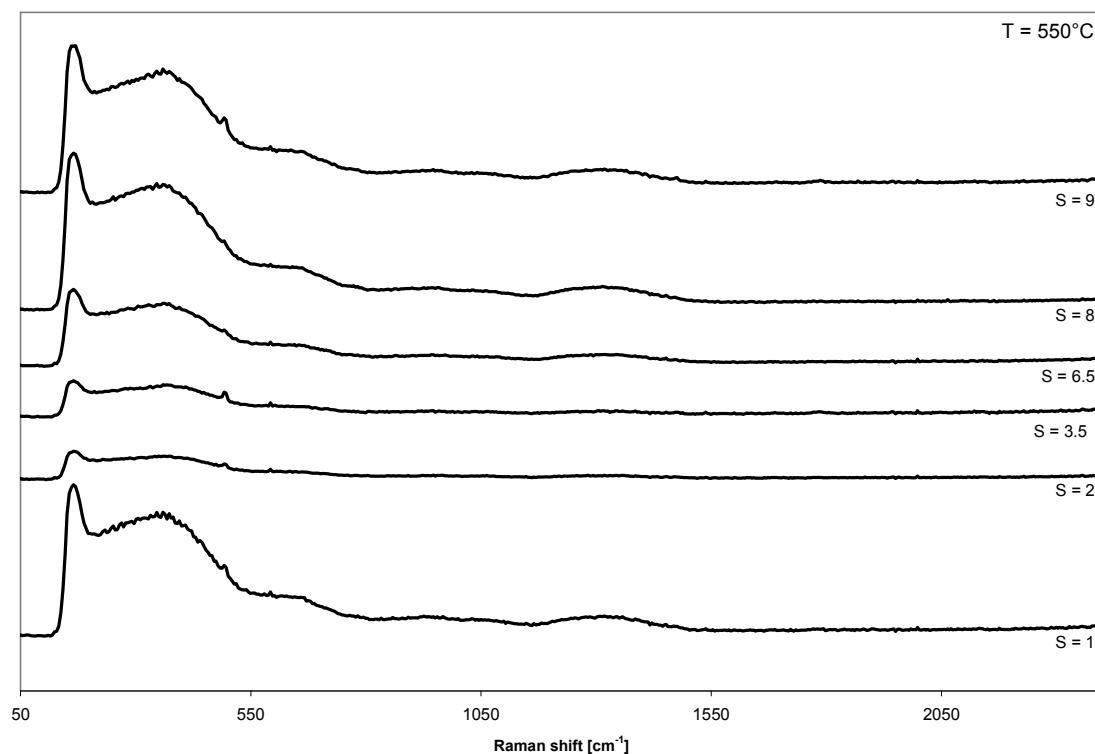


Figure 4.11. Raman spectra of fibers drawn at $T = 550^{\circ}\text{C}$, drawing speeds as shown.

For fibers drawn at 550°C , the peak at 165 cm^{-1} does not show a trend in intensity vs. drawing speed. The intensity fluctuates irregularly. The same is true for the band at 370 cm^{-1} . The intensity of the shoulder at 490 cm^{-1} shows a similar behavior as for the lower draw temperature fibers. The maximum intensity for this peak occurs at a draw speed of 6.5 m/s and decreases at both higher and lower draw speeds. The shoulder at 660 cm^{-1} appears to increase in intensity as the draw speed increases. The bands at 960 and 1320 cm^{-1} are not showing any regular change with drawing speed.

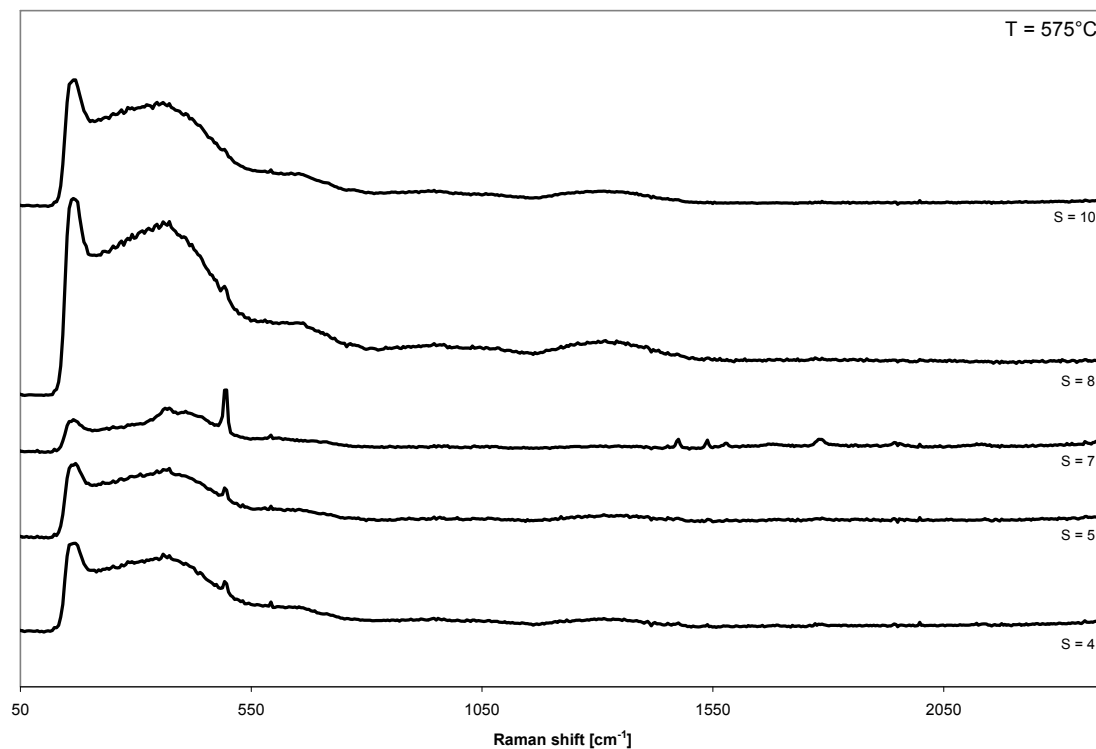


Figure 4.12. Raman spectra of fibers drawn at $T = 575^{\circ}\text{C}$, drawing speeds as shown.

The 165 cm^{-1} band for fibers drawn at 575°C shows a maximum at a draw speed of 5 m/s , as does the band at 370 cm^{-1} . The bands at 490 and 2450 cm^{-1} show a maximum in intensity at a draw speed of 7 m/s with lower intensities at both higher and lower draw speeds. The bands at 660 , 960 and 1310 cm^{-1} shows a maximum at 5 m/s draw speed and lower intensities at lower and higher draw speeds.

In order to better display the relationships of the individual peaks to drawing speed plots of the intensity of a single peak vs drawing speed are shown in Figure 4.14 to Figure 4.19. All intensities have been normalized to the Rayleigh intensity of the appropriate spectrum. All lines are drawn to guide the eye.

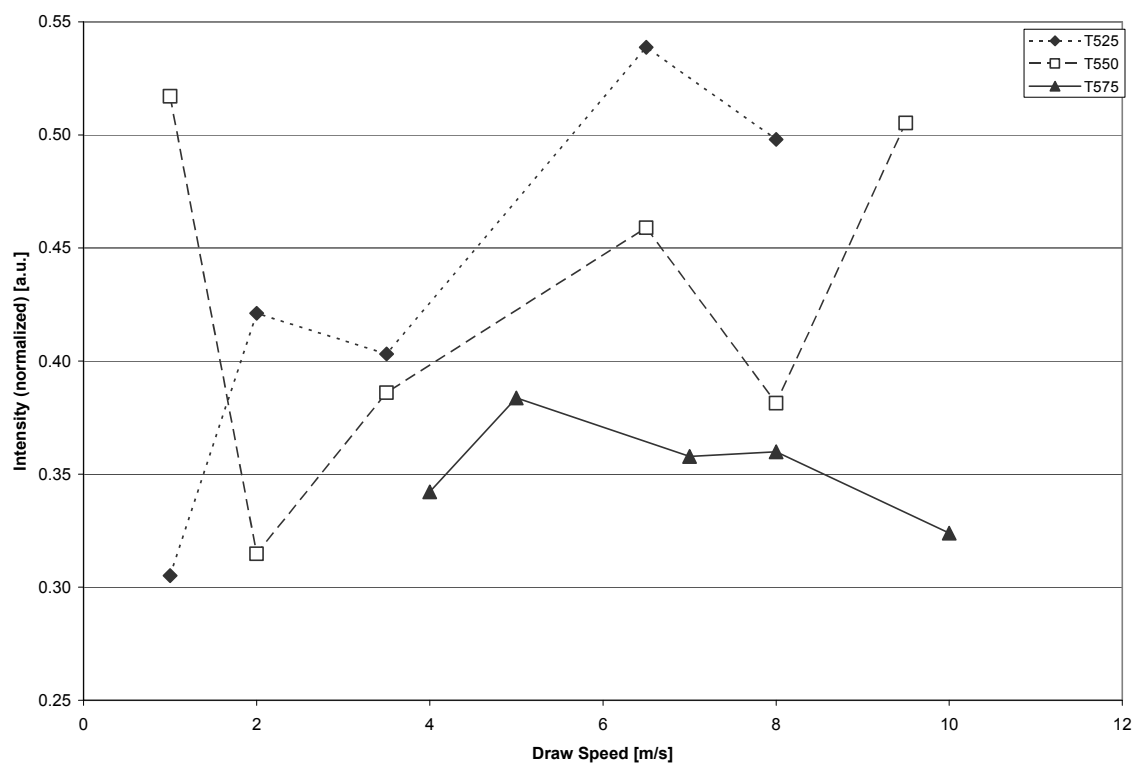


Figure 4.13. Intensities of the 165 cm⁻¹ peak vs drawing speed.

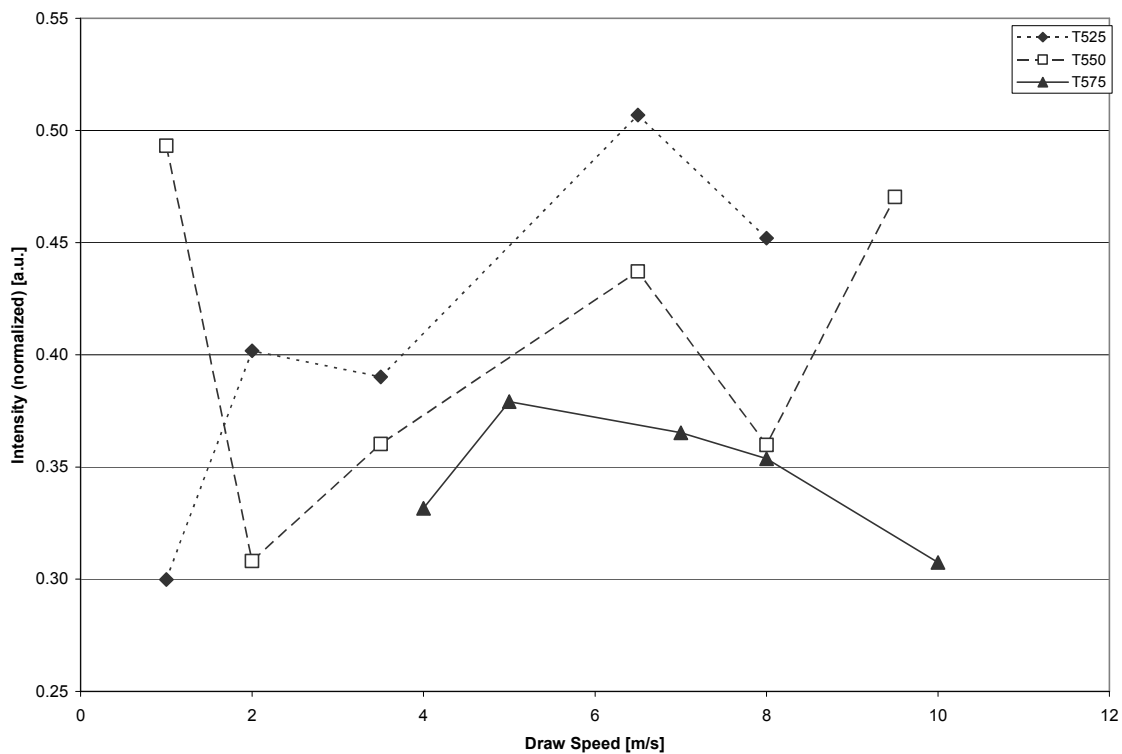


Figure 4.14. Intensities of the 370 cm^{-1} peak vs drawing speed.

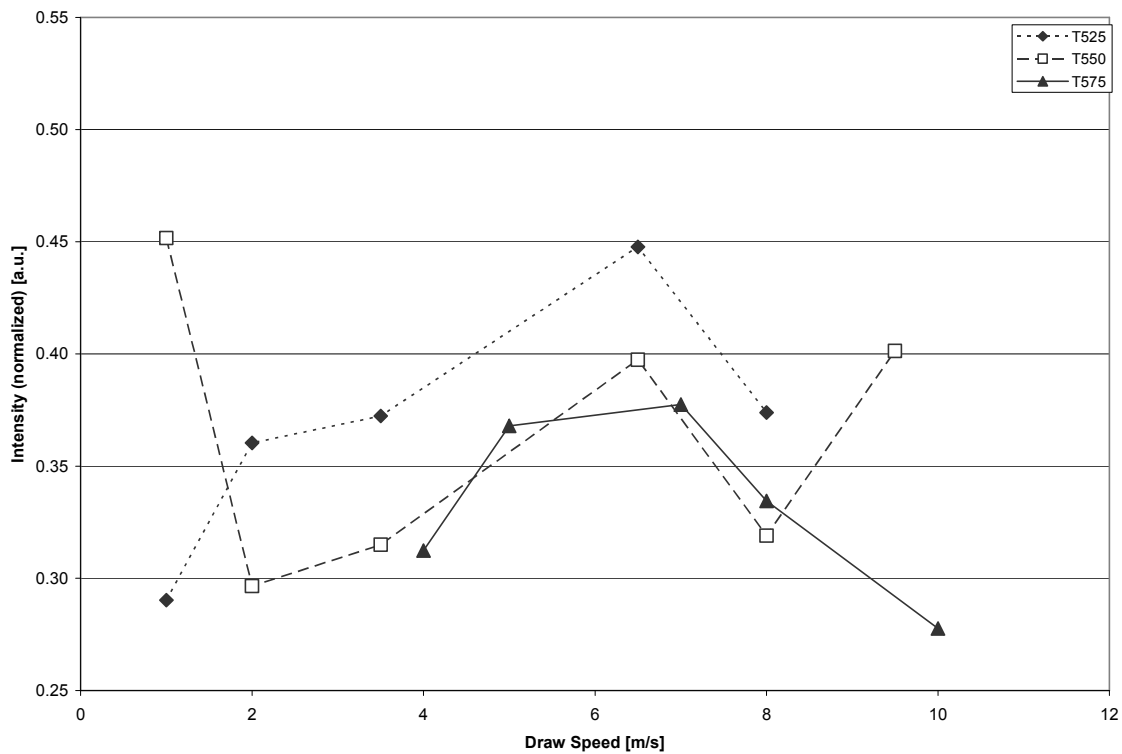


Figure 4.15. Intensities of the 490 cm^{-1} peak vs drawing speed.

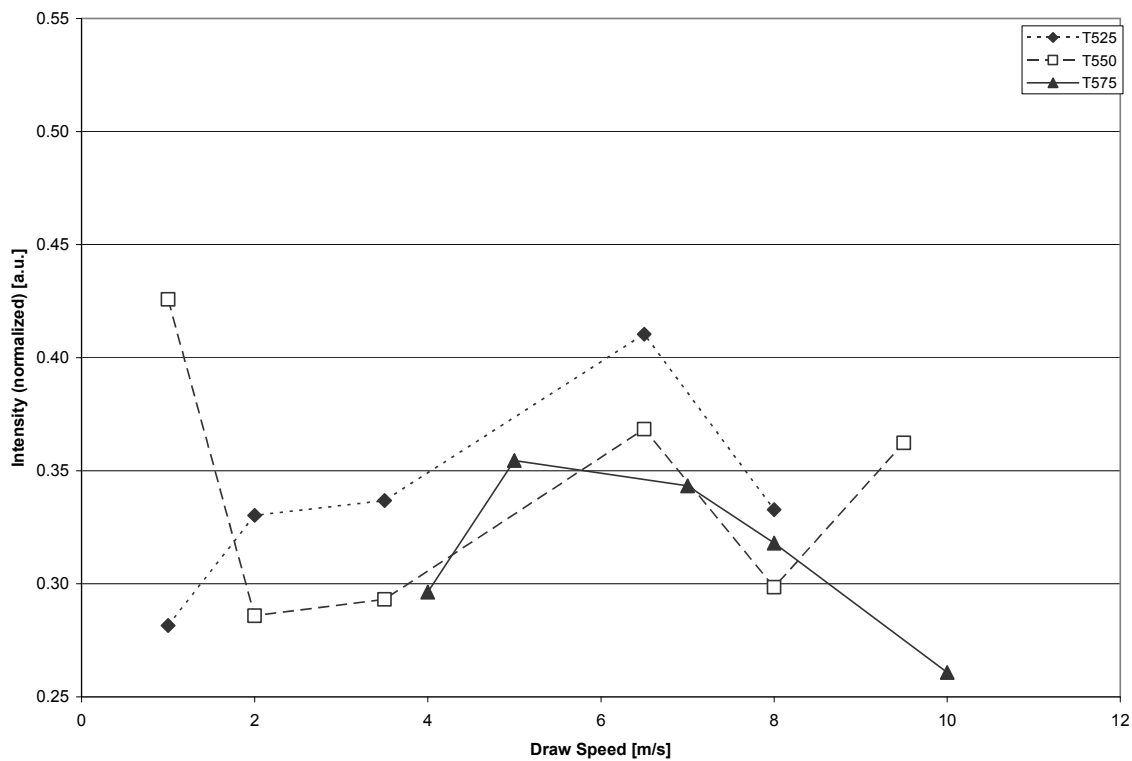


Figure 4.16. Intensities of the 660 cm⁻¹ peak vs drawing speed.

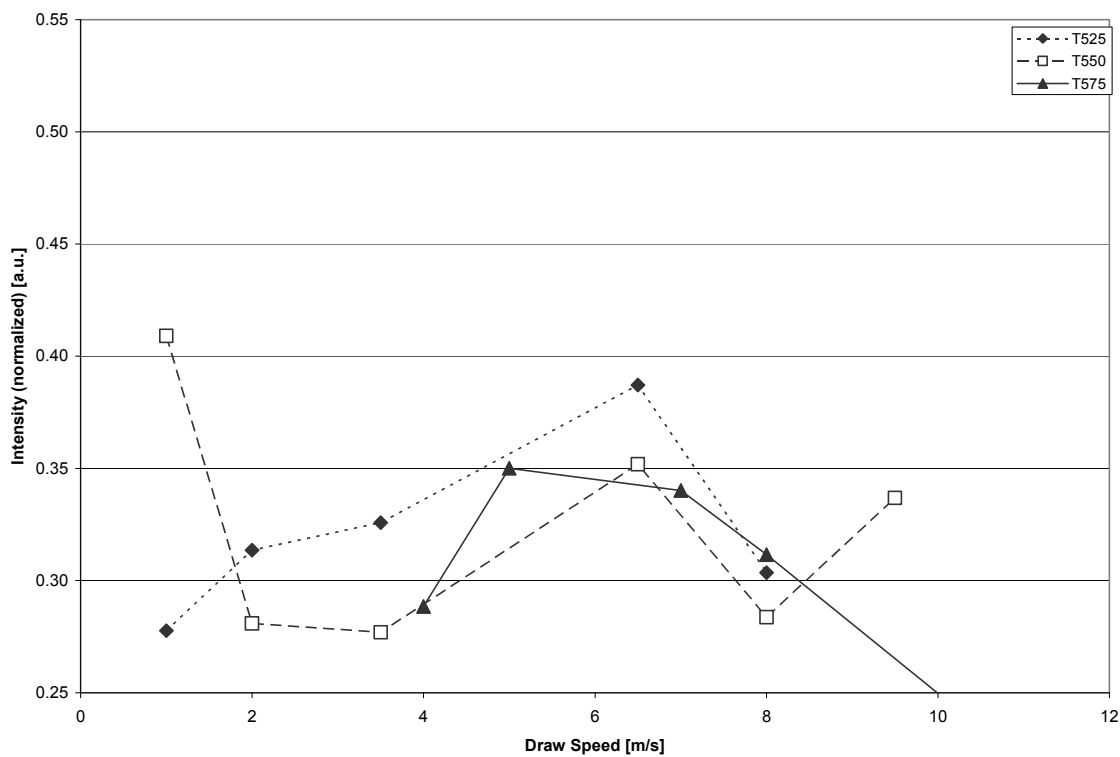


Figure 4.17. Intensities of the 960 cm⁻¹ peak vs drawing speed.

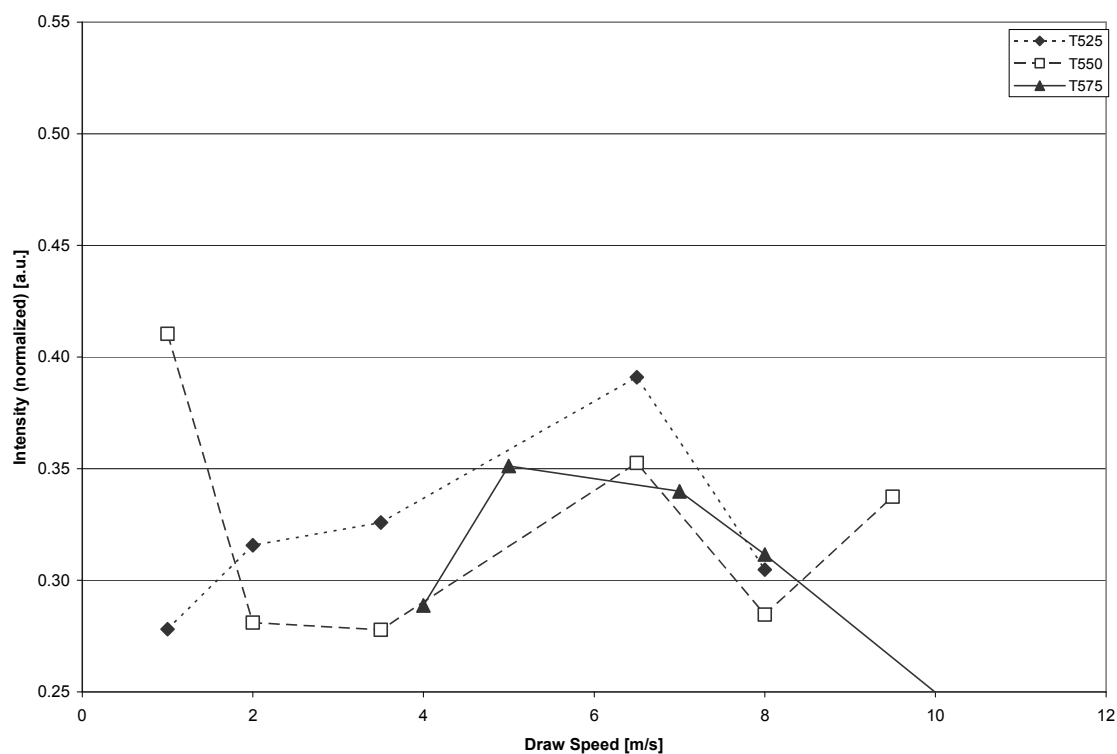


Figure 4.18. Intensities of the 1310 cm^{-1} peak vs drawing speed.

4.5 Discussion and Conclusions

According to Lines^{32,33} the Raman spectrum of heavy metal containing glasses can be divided into four regions (see Chapter 4.2). The first region below 100 cm^{-1} contains no peaks in our spectra.

The second region from roughly $70 - 160\text{ cm}^{-1}$ contains a peak at 165 cm^{-1} . This region is classified by Lines^{32,33} as stemming from heavy metal vibrations. Based on additional work by Kharlamov et al.³⁴ and Baia et al.,^{35,37} who examined bismuth gallate and doped bismuth borate glasses, respectively, the observed peak at 165 cm^{-1} can be assigned to the presence of distorted $[\text{BiO}_6]$ octahedral units.^{35,37}

The next range of bands as classified by Lines^{32,33} from roughly $300 - 600\text{ cm}^{-1}$ is caused by bridged anion motions. Baia et al.^{35,37} find peaks in their doped bismuth borate glasses at 380 cm^{-1} , assigned to $\text{Bi} - \text{O} - \text{Bi}$ bridging motions of O^- in highly distorted $[\text{BiO}_6]$ octahedral. Kharlamov³⁴ is able to show bands at roughly 370 , 500 and 650 cm^{-1} and also assigns these to heavy metal bridging motions in his glasses. He assigns the low frequency band at 370 cm^{-1} to bridging motions with two dissimilar cations in his glasses ($\text{Ga} - \text{O} - \text{Pb}$, $\text{Ga} - \text{O} - \text{Bi}$ and $\text{Bi} - \text{O} - \text{Pb}$). Therefore the peak in these spectra at 370 cm^{-1} can be assigned to the bridging motion of O in a $\text{B} - \text{O} - \text{Bi}$ bridge. The peak at roughly 500 cm^{-1} he assigns to the bridging motion of two similar cations in his glasses. The peak at 492 cm^{-1} is therefore tentatively assigned to this motion of either $\text{B} - \text{O} - \text{B}$ or $\text{Bi} - \text{O} - \text{Bi}$.

The peak at 660 cm^{-1} is noted by Chrysikos et al.³⁰ and Konijnendijk⁵ to be indicative of chain – type metaborate units.

According to Lines^{32,33} bands in the last region above 600 cm^{-1} are caused by non – bridging anion modes.

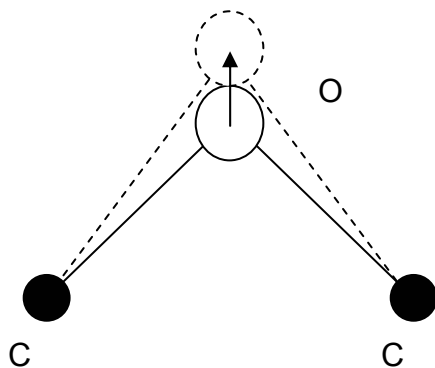


Figure 4.19. Bridged anion mode after Lines (C = cation).^{32,33}

Konijnendijk and Stevels noted in their papers^{5,27} that for more than 45 mol% alkali in alkali borate glasses, more complicated borate arrangements decompose into several smaller borate groups. The $[\text{BO}_3]$ triangle is one of these groups and is characterized by a peak at 940 cm^{-1} . Therefore the peak at 960 cm^{-1} is tentatively assigned to this group, as no other peaks noted by other authors are close to this region.

The band at 1320 cm^{-1} was noted by several authors^{28,31,34,35,37} and they all assigned the band to the asymmetric non – bridging Bi – O^- stretch in a $[\text{BiO}_6]$ octahedron.

Spectra for all draw temperatures show similar trends. The increase in the 165 cm^{-1} band shows that the heavy metal ion vibration increases in intensity as draw speed increases. This can be interpreted as a change in the configuration of the $[\text{BiO}_6]$ octahedra. The heavy metal vibration becoming more intense with higher draw speeds would indicate a higher degree of freedom of the heavy metal ion, resulting from an increasing distortion of the octahedral coordination. The behavior of the bands at 370 and 1320 cm^{-1} show similar behavior. They also result from vibrations in the $[\text{BiO}_6]$ octahedral confirming this interpretation. The band at 660 cm^{-1} also increases in intensity with increasing draw speed and indicating the formation of more chain – type metaborate groups. The band at 960 cm^{-1} does not change in intensity indicating that no new boron triangles are

formed. The band at 490 cm^{-1} shows a increase in intensity until a draw speed of 3.5 m/s is reached and then its intensity declines again. At higher draw temperatures the draw speed at which maximum intensity occurs changes towards higher draw speeds. Since this band is assigned to the bridging vibration of a similar cation bridge, this indicates an optimal distortion of the octahedron is possible to give the oxygen ions a maximum degree of freedom. But as draw speed increases the increasing distortion of the coordination decreases the freedom of the oxygen ions. All this behavior indicates a rearrangement in the alignment of the structure of the glass fiber without the decay of any structural groups.

After careful analysis the band at 2450 cm^{-1} was revealed to be a machine artifact resulting from the artificial lighting in the room where the experiments were conducted.

4.6 References

1. A. Smekal, "Zur Quantentheorie der Dispersion," *Naturwissenschaften*, **11** [43] 873-5 (1923).
2. H. Barańska, A. Łabudzińska, and J. Terpiński, *Laser Raman Spectrometry: Analytical Applications; Ch. 1*. Polish Scientific Publishers, Warszawa, Poland, 1987.
3. J.G. Grasselli and B.J. Bulkin, *Analytical Raman Spectroscopy*; Ch. 1-3. Wiley, New York, 1991.
4. WITec_GmbH, Confocal Raman Microscope CRM 2000, Operating Manual. WITec, Ulm, Germany, 2001.
5. W.L. Konijnendijk and J.M. Stevels, "The Structure of Borate Glasses Studied by Raman Scattering," *J. Non-Cryst. Solids*, **18** [3] 307-31 (1975).
6. F.I. Galeener, "Planar Rings in Glasses," *Solid State Commun.*, **44** [7] 1037-40 (1982).
7. T. Yano, N. Kunimine, S. Shibata, and M. Yamane, "Structural Investigation of Sodium Borate Glasses and Melts by Raman Spectroscopy. I. Quantitative Evaluation of Structural Units," *J. Non-Cryst. Solids*, **321** [3] 137-46 (2003).
8. T. Yano, N. Kunimine, S. Shibata, and M. Yamane, "Structural Investigation of Sodium Borate Glasses and Melts by Raman Spectroscopy. II. Conversion between BO_4 and BO_2O^- Units at High Temperature," *J. Non-Cryst. Solids*, **321** [3] 147-56 (2003).
9. T. Yano, N. Kunimine, S. Shibata, and M. Yamane, "Structural Investigation of Sodium Borate Glasses and Melts by Raman Spectroscopy. III. Relation between the Rearrangement of Super-Structures and the Properties of Glass," *J. Non-Cryst. Solids*, **321** [3] 157-68 (2003).
10. E.I. Kamitsos, M.A. Karakassides, and G.D. Chryssikos, "Structure of Borate Glasses. Part 1. Raman Study of Cesium, Rubidium and Potassium Borate Glasses," *Phys. Chem. Glasses*, **30** [6] 229-34 (1989).
11. E.I. Kamitsos and M.A. Karakassides, "Structural Studies of Binary and Pseudo Binary Sodium Borate Glasses of High Sodium Content," *Phys. Chem. Glasses*, **30** [1] 19-26 (1989).

12. E.I. Kamitsos, M.A. Karakassides, and G.D. Chryssikos, "Vibrational Spectra of Magnesium - Sodium - Borate Glasses. 2. Raman and Mid-Infrared Investigation of the Network Structure," *J. Phys. Chem.*, **91** [5] 1073-9 (1987).
13. E.I. Kamitsos, M.A. Karakassides, and G.D. Chryssikos, "A Vibrational Study of Lithium Borate Glasses with High Li₂O Content," *Phys. Chem. Glasses*, **28** [5] 203-9 (1987).
14. E.I. Kamitsos, M.A. Karakassides, and G.D. Chryssikos, "A Vibrational Study of Lithium Sulfate Based Fast Ionic Conducting Borate Glasses," *J. Phys. Chem.*, **90** [19] 4528-33 (1986).
15. B.N. Meera and J. Ramakrishna, "Raman Spectral Studies of Borate Glasses," *J. Non-Cryst. Solids*, **159** [1-2] 1-21 (1993).
16. R. Akagi, N. Ohtori, and N. Umesaki, "Raman Spectra of K₂O - B₂O₃ Glasses and Melts," *J. Non-Cryst. Solids*, **293-5** [1] 471-6 (2001).
17. M. Irion, M. Couzi, A. Levasseur, J.M. Reau, and J.C. Brethous, "An Infrared and Raman Study of New Ionic-Conductor Lithium Glasses," *J. Solid State Chem.*, **31** [3] 285-94 (1980).
18. W. Soppe, J. Kleerebzem, and H.W. den Hartog, "Raman Spectroscopy Study of 1-x-y(B₂O₃)x(Li₂O)y(Li₂Cl₂) and 1-x-y(B₂O₃)x(Li₂O)y(Cs₂O)," *J. Non-Cryst. Solids*, **93** [1] 142-54 (1987).
19. J. Loroersch, M. Couzi, J. Pelous, R. Vacher, and A. Levasseur, "Brillouin and Raman Scattering Study of Borate Glasses," *J. Non-Cryst. Solids*, **69** [1] 1-25 (1984).
20. G.D. Chryssikos, E.I. Kamitsos, and M.A. Karakassides, "Structure of Borate Glasses. Part 2. Alkali Induced Network Modifications in Terms of Structure and Properties," *Phys. Chem. Glasses*, **31** [3] 109-16 (1990).
21. D. Maniu, I. Ardelean, and T. Iliescu, "Raman Spectroscopic Investigations of the Structure of x V₂O₅. (1-x)[3 B₂O₃ · K₂O] Glasses," *Mater. Lett.*, **25** [3-4] 147-9 (1995).
22. D. Maniu, I. Ardelean, T. Iliescu, S. Cinta, and O. Cozar, "Raman Spectroscopic Investigations of the Oxide Glass System (1-x)[3 B₂O₃ · K₂O]. x MO (MO = V₂O₅, CuO)," *J. Mol. Struct.*, **410-1** 291-4 (1997).
23. D. Maniu, I. Ardelean, T. Iliescu, S. Cinta, V. Nagel, and W. Kiefer, "Raman Spectroscopic Investigations on Oxide Glass System (1-x)[3 B₂O₃ · K₂O]. x TiO₂," *J. Mol. Struct.*, **480-1** 657-9 (1999).

24. D. Maniu, I. Ardelean, T. Iliescu, and C. Pantea, "Raman Spectroscopic Investigations of the Structure of x CuO. $(1-x)[3 \text{ B}_2\text{O}_3 \cdot \text{K}_2\text{O}]$," *J. Mat. Sci. Lett.*, **16** [1] 19-20 (1997).
25. A.K. Hassan, L. Borjesson, and L.M. Torell, "The Boson Peak in Glass Formers of Increasing Fragility," *J. Non-Cryst. Solids*, **172-4** 154-60 (1994).
26. D. Maniu, T. Iliescu, I. Ardelean, S. Cinta-Pinzaru, N. Tarcea, and W. Kiefer, "Raman Study of B_2O_3 - CaO glasses," *J. Mol. Struct.*, **651-3** 485-8 (2003).
27. W.L. Konijnendijk, "Structure of Glasses in the Systems CaO - Na_2O - B_2O_3 and MgO - Na_2O - B_2O_3 Studied by Raman Scattering," *Phys. Chem. Glasses*, **17** [6] 205-8 (1976).
28. W.L. Konijnendijk and H. Verweij, "Structural Aspects of Vitreous PbO 2 B_2O_3 Studied by Raman Scattering," *J. Am. Ceram. Soc.*, **59** [9] 459-61 (1976).
29. Y. Tang, Z. Jiang, and X. Song, "NMR, IR and Raman Spectra Study of the Structure of Borate and Borosilicate Glasses," *J. Non-Cryst. Solids*, **112** [2-3] 131-5 (1989).
30. G.D. Chryssikos, E.I. Kamitsos, and W.M. Risen, "A Raman Investigation of Cadmium Borate and Borogermanate Glasses," *J. Non-Cryst. Solids*, **93** [1] 155-68 (1987).
31. B.N. Meera, A.K. Sood, N. Chandrabhas, and J. Ramakrishna, "Raman Study of Lead Borate Glasses," *J. Non-Cryst. Solids*, **126** [3] 224-30 (1990).
32. M.E. Lines, "Absolute Raman Intensities in Glasses. I. Theory," *J. Non-Cryst. Solids*, **89** [3] 143-62 (1987).
33. M.E. Lines, A.E. Miller, K. Nassau, and K.B. Lyons, "Absolute Raman Intensities in Glasses. II. Germania Based Heavy Metal Oxides and Global Criteria," *J. Non-Cryst. Solids*, **89** [1-2] 163-80 (1987).
34. A.A. Kharlamov, R.M. Almeida, and J. Heo, "Vibrational Spectra and Structure of Heavy Metal Oxide Glasses," *J. Non-Cryst. Solids*, **202** [3] 233-40 (1996).
35. L. Baia, R. Stefan, W. Kiefer, J. Popp, and S. Simon, "Structural Investigations of Copper Doped B_2O_3 - Bi_2O_3 Glasses with High Bismuth Oxide Content," *J. Non-Cryst. Solids*, **303** [3] 379-86 (2003).

36. A.E. Miller, K. Nassau, K.B. Lyons, and M.E. Lines, "The Intensity of Raman Scattering in Glasses Containing Heavy Metal Ions," *J. Non-Cryst. Solids*, **99** [2-3] 289-307 (1988).
37. L. Baia, R. Stefan, J. Popp, S. Simon, and W. Kiefer, "Vibrational Spectroscopy of Highly Iron Doped B_2O_3 - Bi_2O_3 Glass Systems," *J. Non-Cryst. Solids*, **324** [1-2] 109-17 (2003).

5 Dependence of Heat Capacity of Fibers on Aspect Ratio

5.1 Introduction

It has been previously noted by a number of authors¹⁻⁵ that fibers of a material show an anomalously high heat capacity compared to the bulk material. Raszewski³ noted that the heat capacity of glass coated amorphous metal wire differs from that of glass coated amorphous metal ribbon by a factor of 3 – 4.

This study attempts to determine the origin of this difference for bismuth borate glass fibers. Towards this end the heat capacity of glass fibers with different aspect ratios was measured. The aspect ratio of a cylindrical body is defined as its length divided by its diameter. Care was taken to vary only the aspect ratio of the fibers in each measurement.

The heat capacity of a glass fiber is of importance in many fields such as optics⁶ and composites.⁷ The heat capacity of a material determines its sensitivity to temperature, which is of prime importance in glass fibers in optical communications, where a small change of refractive index due to temperature fluctuations is very detrimental to the properties of the fiber. This property is also of importance in composite materials containing short fibers or other aspected materials, where fluctuations in temperature can affect the different components rather dissimilarly, causing stresses in the material.⁷ The heat capacity also influences other thermal properties such as thermal conductivity which is of prime importance in determining the thermal insulation properties of a material.

Heat capacity can be modeled very well for some materials such as gasses. But solid materials are difficult to describe accurately with models. The basic models of heat capacity are presented in the following chapter.

5.2 Literature Review

The heat stored in a solid increases as temperature increases and decreases as temperature falls. The amount of heat necessary to increase the temperature of a mole of solid by 1 K is called the molar heat capacity. Thus heat capacity can be defined as the derivative of the internal energy U with respect to temperature, because in a solid almost all of the heat is stored as internal energy.

$$C = \frac{dU}{dT} \quad (5.1)$$

This definition needs to take into account the differences between heat capacity at constant pressure versus the heat capacity at constant volume. For a solid, however, this difference is small. The heat capacity at constant pressure however includes that caused by thermal expansion so that for solids C_p is always larger than C_v .

5.2.1 The heat capacity of an ideal gas^{8,9}

The first model of heat capacity was derived for a perfect gas. In a perfect gas the motion of the gas particles is totally random and the interaction between the gas particles is limited to elastic collisions. This means that the thermal energy of the system as a whole is simply the mean of the kinetic energy of the particles that make up the system:

$$\langle \frac{1}{2}mv^2 \rangle = 3k_B T/2 \quad (5.2)$$

where k_B is Boltzmann's coefficient, $k_B = 1.38 \cdot 10^{-23} \text{ JK}^{-1}$.

In a crystal an atom is vibrating about its rest position in a manner easily approximated by a linear harmonic oscillator model, assuming a displacement $x = A \sin \omega t$ and a “spring” force of $-Kx$. This results in a kinetic energy of

$$\frac{1}{2}mv^2 = \frac{1}{2}mA^2\omega^2 \cos^2 \omega t \quad (5.3)$$

And a potential energy of

$$\frac{1}{2}Kx^2 = \frac{1}{2}KA^2 \sin^2 \omega t \quad (5.4)$$

However, since $\omega^2 = K/m$, the total energy of the oscillator equals twice its mean energy.

Since an atom in a gas vibrates in three dimensions around its resting position the mean value of the kinetic energy of the atom is given by $3k_B T/2$. Therefore in a mole of crystal the mean energy is given by

$$U = 3RT \quad (5.5)$$

And therefore the heat capacity of an ideal crystal is

$$C = \frac{dU}{dT} = 3R = 25 \text{ JK}^{-1}\text{mol}^{-1} \quad (5.6)$$

This is called the Dulong – Petit limit of heat capacity.

This model works well for materials that approximate the behavior of a perfect gas. However, for materials such as crystals, in which the atomic interactions are not negligible the deviation of the heat capacity from the predicted amount is significant.

5.2.2 The Einstein model of heat capacity^{8,9}

Einstein proposed a model for heat capacity based on the vibrations of an atom inside a crystal. He proposed that the vibrations of N_A molecules in a crystal can be modeled by the vibrations of $3 N_A$ identical oscillators having the same frequency and no interactions with each other. The new idea introduced by Einstein was that of quantization of the energy of the oscillators. According to quantum theory the energy of the oscillators cannot change in a continuous fashion. There must be a minimum energy for each oscillator in order to preserve Heisenberg's uncertainty principle. And therefore there must also be a number of defined energy levels that the oscillator can inhabit that are multiples

of that energy. The minimum energy is defined by $\frac{1}{2}\eta\omega$ and the energy of the n -th energy level is therefore given by

$$E_n = \left(n + \frac{1}{2}\right)\eta\omega \quad (5.7)$$

This model does not affect the heat capacity at higher temperatures very much but has profound implications at low temperatures, when the abrupt changes from one small energy level to another are large compared to the total energy of the oscillator.

When considering a set of $3N$ oscillators, which corresponds to N atom vibrating in three dimensions, at a temperature T , each oscillator contains a number of quanta $(n+1/2)$. The number of quanta in each oscillator varies but the mean value can be determined via thermodynamics. The probability of an oscillator at temperature T occupying an energy state $E_n = (n + \frac{1}{2})\eta\omega$, as given by its quantum number n is proportional to $\exp(-E_n/k_B T)$. Thus the value of the mean of n can be determined using the equipartition principle

$$\begin{aligned} \bar{n} &= \frac{1}{Z} \sum n \exp\left(-\frac{E_n}{k_B T}\right) = \frac{\exp\left(-\frac{1}{2} \frac{\eta\omega}{k_B T}\right)}{Z} \sum n \exp\left(-\frac{n\eta\omega}{k_B T}\right) \\ Z &= \sum \exp\left(-\frac{E_n}{k_B T}\right) = \exp\left(-\frac{1}{2} \frac{\eta\omega}{k_B T}\right) \sum \exp\left(-\frac{n\eta\omega}{k_B T}\right) \end{aligned} \quad (5.8)$$

With $\exp(-\eta\omega/k_B T) = y$ it follows that

$$\bar{n} = \frac{\sum n y^n}{\sum y^n} \quad (5.9)$$

The denominator of the sum is a simple geometric series described as

$$\sum y^n = 1 + y + y^2 + y^3 + \dots = \frac{1}{1-y} \quad (5.10)$$

And the numerator can be shown to be

$$\sum n y^n = y + 2y^2 + 3y^3 + \dots = y(1 + 2y + 3y^2 + \dots) \quad (5.11)$$

Which is the derivative of the above sum, and so

$$\sum ny^n = \frac{y}{(1-y)^2} \quad (5.12)$$

Therefore

$$\bar{n} = \frac{y}{(1-y)} = \frac{1}{\exp\left(\frac{\eta\omega}{k_B T}\right) - 1} \quad (5.13)$$

This allows the calculation of the average energy of the set of $3N$ oscillators to be carried out

$$\bar{E} = 3N\left(\bar{n} + \frac{1}{2}\right) = 3N\left(\frac{\eta\omega}{2} + \frac{\eta\omega}{\exp\left(\frac{\eta\omega}{k_B T}\right) - 1}\right) \quad (5.14)$$

By definition of a characteristic temperature Θ_E , the Einstein temperature, such that, $\eta\omega = k_B \Theta_E$ this reduces the energy to

$$\bar{E} = 3R\Theta_E\left(\frac{1}{2} + \frac{1}{\exp\left(\frac{\Theta_E}{T}\right) - 1}\right) \quad (5.15)$$

and allows the calculation of the heat capacity as

$$C = \frac{d\bar{E}}{dT} = 3R\left(\frac{\Theta_E}{T}\right)^2 \frac{\exp\left(\frac{\Theta_E}{T}\right)}{\left(\exp\left(\frac{\Theta_E}{T}\right) - 1\right)^2} \quad (5.16)$$

While this model predicts the experimental data of some metals quite nicely, especially copper, the main objection is the assumption that there is no interaction between the oscillators. Also the model deviates from experimental data at low temperatures.

5.2.3 The Debye model of heat capacity^{8,9}

In order to take into account these interactions Debye proposed his own model of thermal excitations in a crystal. Basing his model on calculations performed on vibrating solid rods he defines several conditions for vibrations in a solid. For an exhaustive treatment, the reader is referred to the literature.

Debye assumed the following

- In case of a linear chain of N species, there are N longitudinal waves present. However, in a solid a given chain can also propagate transverse waves, which can be resolved into two vibrations with perpendicular directions. This results in three waves per wave vector. In a crystal the directions of these waves form an orthogonal system, that corresponds to the axes of the crystal. The modes of vibration present in a crystal form a discrete and finite series. The number N of wavevectors present in a crystal is equal to the number of atoms present in the same crystal regardless of shape. In a longitudinal chain model, there are N longitudinal modes.
- The ends of the wave vectors for a given atom lie inside a polyhedral surface in reciprocal space named the Brillouin zone, which can be defined in terms of the corresponding lattice of the crystal. Each of the N wave vectors has associated with it three frequencies, which correspond to its three modes. For small wave vectors the waves behave as in a macroscopic solid. The discontinuous structure of the solid has no influence on the vibration because of the large number of atoms involved in the mode. The mode frequency in this case is simply proportional to the wave vector $\omega = vk$. The propagation velocity v is the speed of sound in the crystal. Anisotropy can cause this speed to vary depending on the direction of propagation. If the wave vector is not small compared to the limiting values dispersion becomes a factor; ω/k is no longer constant. This results in an upper limit on the frequency of the mode for the propagation of a wave.

The Debye model involves a set $3N$ modes for N atoms that occupy quantized energy levels just as the Einstein model does. However the quanta for a modes with frequency ω are defined as phonons and have an energy of $\eta\omega$. At equilibrium the Bose – Einstein statistics give the mean energy per mode as

$$\bar{E} = \frac{\eta\omega}{2} + \frac{\eta\omega}{\exp\left(\frac{\eta\omega}{k_B T}\right) - 1} \quad (5.17)$$

The difference to the Einstein model is that the vibrational frequency ω is no longer constant but is allowed to vary between 0 and ω_{\max} . In order to determine the exact amount of energy in a given mode the calculation proves very difficult.

In order to circumvent this problem Debye suggested a simplification. He suggested the following assumptions.

- The distribution of the modes is assumed to be spherically symmetrical, i.e. the frequency of a given mode depends only on the magnitude of the corresponding wave vector.
- Dispersion is neglected. The upper limit on the frequency of ω no longer applies. But since the number of modes must obey the Dulong – Petit law, a cutoff frequency ω_D is introduced so that the total number of modes is equal to $3N$. The value of ω_D is converted into a temperature equivalent

$$\Theta_D = \frac{\eta}{k_B} \omega_D \quad (5.18)$$

where Θ_D is called the Debye temperature.

These assumptions allow the heat capacity to be calculated to

$$C = k_B \int_0^{\omega_D} \left(\frac{\eta\omega}{k_B T} \right)^2 \frac{\exp\left(\frac{\eta\omega}{k_B T}\right)}{\left(\exp\left(\frac{\eta\omega}{k_B T}\right) - 1\right)} \left(\frac{9N_A \omega^2}{\omega_D^3} \right) d\omega \quad (5.19)$$

Debye's approximations reduces this to ($x = \left(\frac{\eta\omega}{k_B T}\right)$):

$$C = 9R \left(\frac{T}{\Theta_D} \right)^3 \int_0^{\frac{\Theta_D}{T}} \frac{e^x}{(e^x - 1)^2} x^4 dx \quad (5.20)$$

This shows the heat capacity depends only on one parameter T/Θ_D . This has several implications. If the temperature is large the integral only involves small x and the exponential expression can be replaced by $1/x^2$. This results in

$$C = 9R \left(\frac{T}{\Theta_D} \right)^3 \int_0^{\frac{\Theta_D}{T}} x^2 dx = 3R \quad (5.21)$$

Which is the Petit – Dulong limit for high temperatures.

When T is very small and tends to zero we can use the approximation

$$\int_0^{+\infty} \frac{e^x}{(e^x - 1)^2} x^4 dx = \frac{4\pi^4}{15} \quad (5.22)$$

to get

$$C = \frac{12\pi^4}{5} R \left(\frac{T}{\Theta_D} \right)^3 \quad (5.23)$$

Which shows that the heat capacity trends to zero. But as opposed to the Einstein model the trend is not as strong as in Einstein's exponential model, which agrees better with experimental data.

5.2.4 Heat capacity in amorphous solids via low energy excitations⁹

In amorphous solids there have been deviations from the Debye law as discussed above. Experiments at very low temperatures have found that for example the heat capacity of vitreous silica at 25 mK exceeds that calculated by the Debye law by a factor of 1000. Many insulating glasses show a linear term in the heat capacity below 1K. Experiments give evidence that these properties arise from two – level systems and not from the multi – level systems Debye predicts.

For an amorphous solid with N two level systems at low energies the calculation of the heat capacity is as follows. Consider two energy levels split by

an amount of energy equal to Δ which is much less than the minimum Debye energy $k_B\Theta_D$.

The partition function for such a system is ($\tau = k_B T$)

$$Z = \exp\left(\frac{\Delta}{2\tau}\right) + \exp\left(-\frac{\Delta}{2\tau}\right) = 2 \cosh\left(\frac{\Delta}{2\tau}\right) \quad (5.24)$$

and therefore the average internal energy is

$$U = -\frac{1}{2} \Delta \tanh\left(\frac{\Delta}{2\tau}\right) \quad (5.25)$$

The heat capacity calculates to

$$C_V = k_B \left(\frac{\partial U}{\partial \tau} \right) = k_B \left(\frac{\Delta}{2\tau} \right)^2 \sec^2 h^2 \left(\frac{\Delta}{2\tau} \right) \quad (5.26)$$

Supposing that Δ is distributed equally throughout the range of $\Delta = 0$ to $\Delta = \Delta_0$, the average value of C_V is equal to

$$C_V = \left(\frac{k_B}{4\tau^2} \right) \int_0^{\Delta_0} \frac{\Delta^2}{\Delta_0} \sec^2 h^2 \frac{\Delta}{2\tau} d\Delta = \left(\frac{2k_B\tau}{\Delta_0} \right) \int_0^{\Delta_0/2\tau} x^2 \sec^2 h^2 x dx \quad (5.27)$$

This integral cannot be solved analytically but two limit conditions are of special interest. At higher T ($\tau \gg \Delta_0$) the value of C_V reduces to

$$C_V \approx \frac{\Delta_0^2}{12k_B T^2} \quad (5.28)$$

Which tends to zero quickly as T increases. This shows that the low – energy two – level systems are only available and contributing to the heat capacity at very low temperatures, around 1K.

Thus for $T < \Delta_0/k_B$ the heat capacity is roughly

$$C_V \approx \frac{2k_B}{3\Delta_0} T \quad (5.29)$$

which is the contributing linear term.

The relationship between C_p and C_V can be described according to Atkins as

$$C_p = C_v + \frac{T \cdot V_m \cdot \alpha^2}{\kappa_T} \quad (5.30)$$

5.2.5 Previous work

Some of the earliest indications for an aspect ratio effect on thermal properties is presented by Inoue et al.¹⁰ and Chen^{1,11} in their work with the amorphous metallic alloys, Pd₄₈Ni₃₂P₂₀, Fe₇₅Si₁₀B₁₅ and Co_{72.5}-Si_{12.5}B₁₅. Each of those studies examines relaxation behavior for different forms of the alloys. Each study examines samples in the form of a wire with 90 - 250 μm diameter, in the form of a ribbon with circa 20 μm thickness and a width of 1 mm and in the case of the work of Inoue et al.¹⁰ also in the form of a cylinder of 1 mm diameter. The wires are produced using an in - rotating – water spinning method, the ribbons are produced via a melt – spinning drum method and the cylindrical samples are produced by quenching a quartz capillary in water. The main focus of each study is on relaxation behavior but heat capacity measurements via DSC were carried out in each case. The authors find that the heat released by wires and ribbons made of the same material differed significantly. The heat release from wires is 3 – 5 times as large as that released from the ribbons. The authors attribute this behavior due in a large part to the release of energy below T_g and differences in the cooling during processing between the different forms of material.

Raszewski³ in her work with amorphous glass coated metal wires showed a significant difference in heat capacities between different sample shapes of materials of the same composition; wires and ribbons made of Fe_{77.5}Si_{7.5}B₁₅ metallic glass. The wires were formed using a Taylor glass coated melt spinning technique and the ribbons were formed using chill block melt – spinning. Amorphous wire had total diameter of 40 μm with a metallic core 23 μm in diameter. The author examined the heat capacities of the materials using modulated DSC measurements. It was found that the heat capacity of the wire

material was higher by a factor of 3 than that of the ribbon material. The author states similar results are obtained using a non – specified oxide glass fiber.

In their work on silica glass fibers Koike and Tomozawa⁵ and in earlier work by Tomozawa and Peng⁴ the authors examine surface structural relaxation in the presence of water vapor. They measured the fictive temperature of the surface of the samples in fiber glass and plate glass samples over time as the samples are heated in 350 Torr of water partial pressure at 950°C. The measurement is performed via IR spectroscopy by following the evolution of two IR peaks allowing the simultaneous probe of the surface and the bulk of the material. The authors find that the relaxation kinetics of the fiber are faster than that of the plate glass samples despite the samples all having the same initial fictive temperature and composition. The authors simulate the relaxation process with a diffusion equation and predict that the surface structural relaxation of micrometer - sized particles, fibers and thin films should be faster than that of bulk material by at least two orders of magnitude, given a constant composition of the glass.

Kwon et al.² hints at similar results in his works on gel-spun, ultra - high molar mass polyethylene fibers. The authors examine four different fibers samples all made via a gel – spinning technique and all with a molar mass of more than 10^6 Daltons. Heat capacity measurements show a higher heat capacity for all fibers compared to a bulk sample of 100 % crystalline polyethylene. The examined fibers fall into two groups, those that were annealed after stretching and those that were not. Both groups show a higher heat capacity than the bulk sample. The authors reason that this is solely due to a vibrational contribution to heat capacity in a disordered material versus a crystalline polymer.

Weidenfeller et al.⁷ studied thermal properties of particle filled polypropylene. The authors used commercial polypropylene compositions filled with 0 – 50 vol% of a number of filler materials. Magnetite (Fe_3O_4), barite (BaSO_4), talc ($\text{Mg}_3[\text{Si}_4\text{O}_{10}][\text{OH}]_2$), strontium ferrite ($\text{SrFe}_{12}\text{O}_{19}$), copper and glass fibers were used as fillers. The particle shape of all fillers was analyzed; all fillers except talc which has platelet shaped particles and the glass fibers, the shape of the filler

particles was irregular. Samples for analysis were produced in an injection molding process. Despite the higher thermal conductivity and heat capacity values of copper, the talc and glass fiber filled samples show a higher heat capacity than the copper filled ones. At a filler volume of 30 vol% the glass fiber filled sample shows the highest heat capacity of all samples, exceeding even that of pure polypropylene. The authors concentrate their analysis on thermal conductivity properties and do not analyze the heat capacity data further. They are able to explain the high thermal conductivity of talc filled polypropylene by examining the interconnectivity of the platelet network. They find a very high interconnectivity of the talc platelets as the reason for the high value thermal conductivity.

5.3 Experimental Procedure

Bismuth borate glass fibers were produced as described in chapter 3. Fibers that were drawn at a temperature of 575°C and a draw speed of 5 m/s were chosen for this study due to the large amount of fibers available for this set of drawing conditions.

In order to produce different aspect ratios some of the fibers were cut using a razor blade mounted on a small adjustable arm with a ruler (see Figure 5.1) to lengths of 1, 2, 3, 4, and 5 mm.

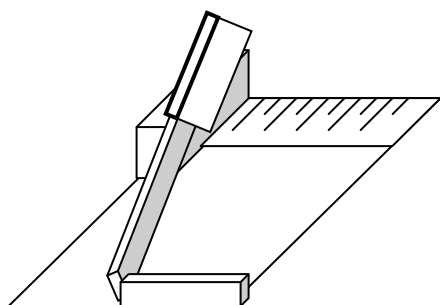


Figure 5.1. Fiber cutter

For the smaller aspect ratios the fibers were embedded in paraffin wax and cut using a microtome as shown in Figure 5.2. After cutting the fibers were eluted from the wax using p – Xylene and rinsed with acetone and water. Under the optical microscope no change in surface topology could be observed.

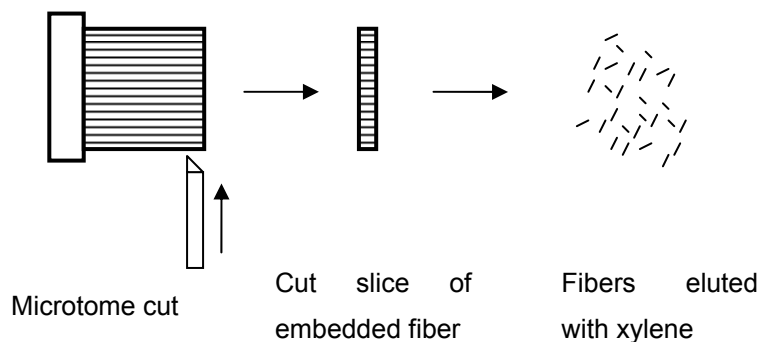


Figure 5.2. Fiber preparation via microtome and elution

The diameter and lengths of the fibers were measured using an optical microscope^l with an attached CCD camera. An image analysis program^m was used to calculate length and diameter from a standard measurement. At least 15 measurements were taken and averaged for the diameter measurement and at least 50 measurements to determine the length. The fiber aspect ratios were calculated using the shortest and longest of the measured fiber lengths and then averaged.

20 mg of the cut fibers were filled into hermetically sealed DSC pans and cold welded shut with the lid inverted to guarantee good thermal contact (see Figure 5.3).

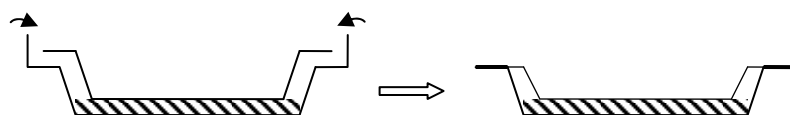


Figure 5.3. Cold welded hermetic DSC pan

The heat capacity and the glass transition temperature of the fibers were measured using the ASTM method described in Chapter 3.

Two different sets of experiments were run. In the first set the fibers' heat capacity was measured below T_g . Each sample was measured five times and the temperature of the samples was always kept to temperatures 50°C below T_g in order to minimize relaxations. These samples are labeled “unrelaxed” in the graphs. In the second set of experiments the sample was deliberately heated to 100°C above T_g and the heat capacity was also measured five times. This was done to determine the influence of relaxation on the aspect ratio effect. These samples were labeled “relaxed” in the graphs.

^l Leitz Laborlux II POL

^m Image Pro 3.1

5.4 Results

The lengths and aspect ratio of the fibers used are shown in Table 5.I. The diameter of the fibers was measured to be $30.4 \pm 1.4 \mu\text{m}$.

Table 5.I: Length and Aspect Ratios of T575 S5 Fibers

Length [μm]				Aspect ratio			
Average		Minimum	Maximum	Minimum	Maximum	Average	
$3827 \pm$	1320	2507	5147	86	162	$124 \pm$	53
$3271 \pm$	997	2274	4268	78	134	$106 \pm$	39
$2225 \pm$	1095	1130	3319	39	104	$72 \pm$	46
$1239 \pm$	311	929	1550	32	49	$40 \pm$	12
$1027 \pm$	366	661	1394	23	44	$33 \pm$	15
$82 \pm$	45	37	128	1	4	$3 \pm$	2
$41 \pm$	30	11	70	1	2	$1 \pm$	1

The heat capacity of the fibers from 100 to 400°C in 50°C intervals is shown in Figure 5.4 to Figure 5.10. Measurements were carried out in the manner described in Chapter 3.

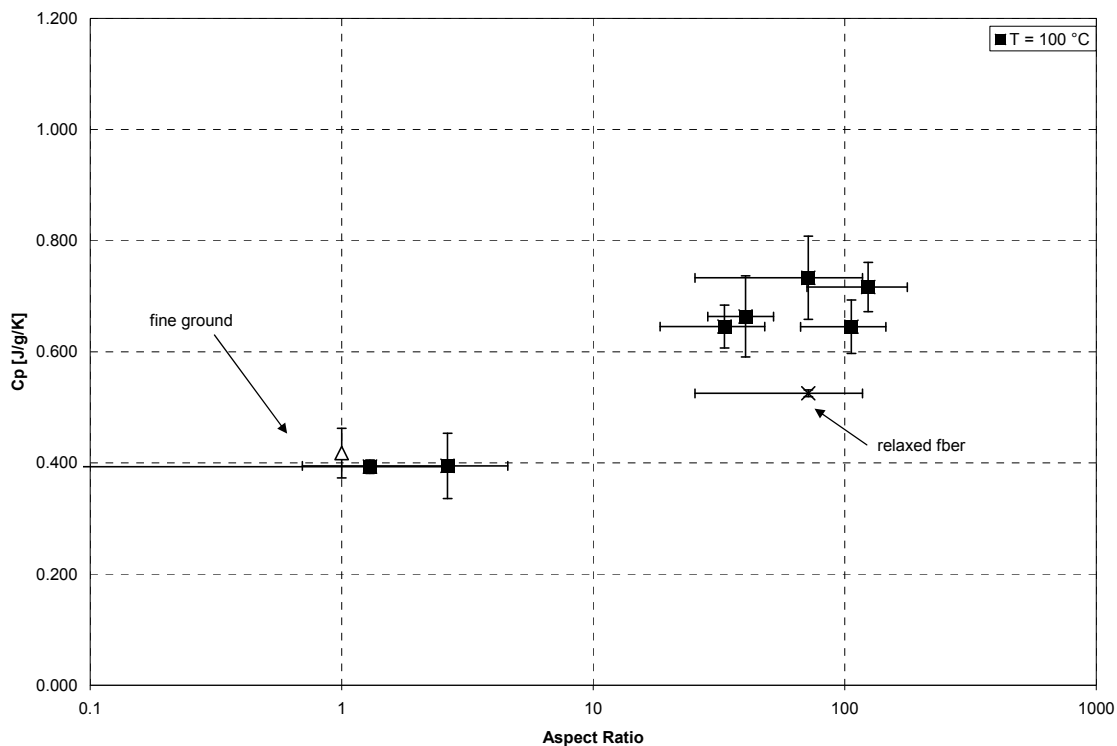


Figure 5.4. Heat capacity dependence fibers on aspect ratio at 100°C

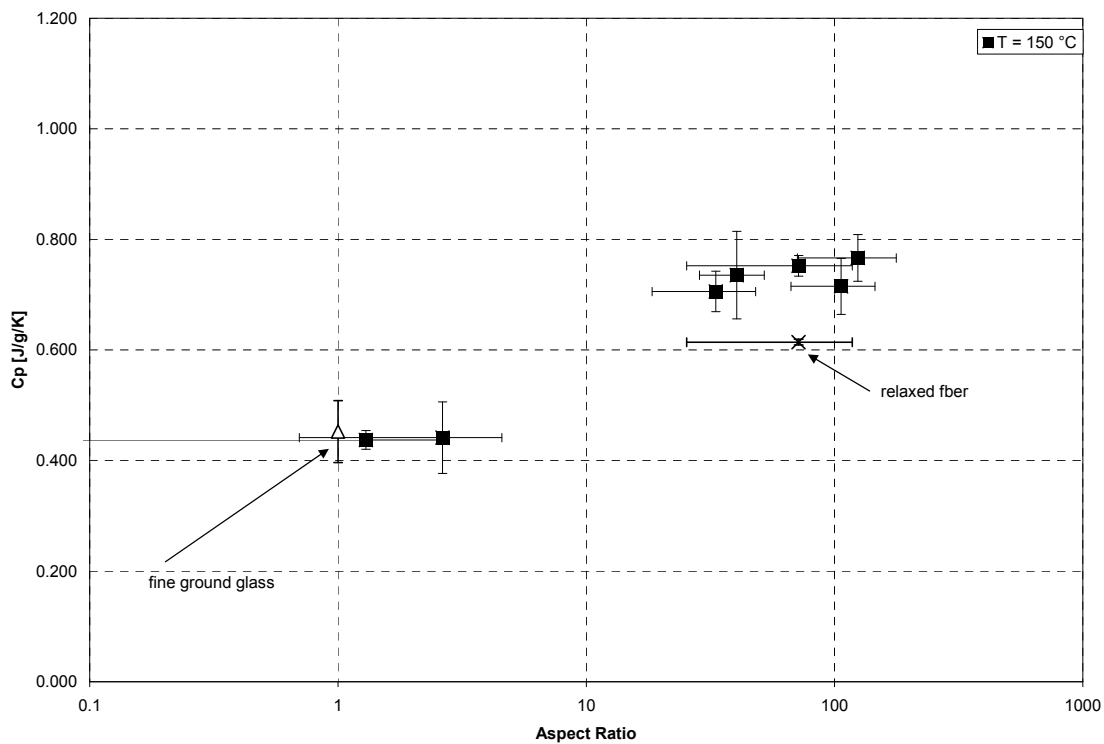


Figure 5.5. Heat capacity dependence of fibers on aspect ratio at 150°C

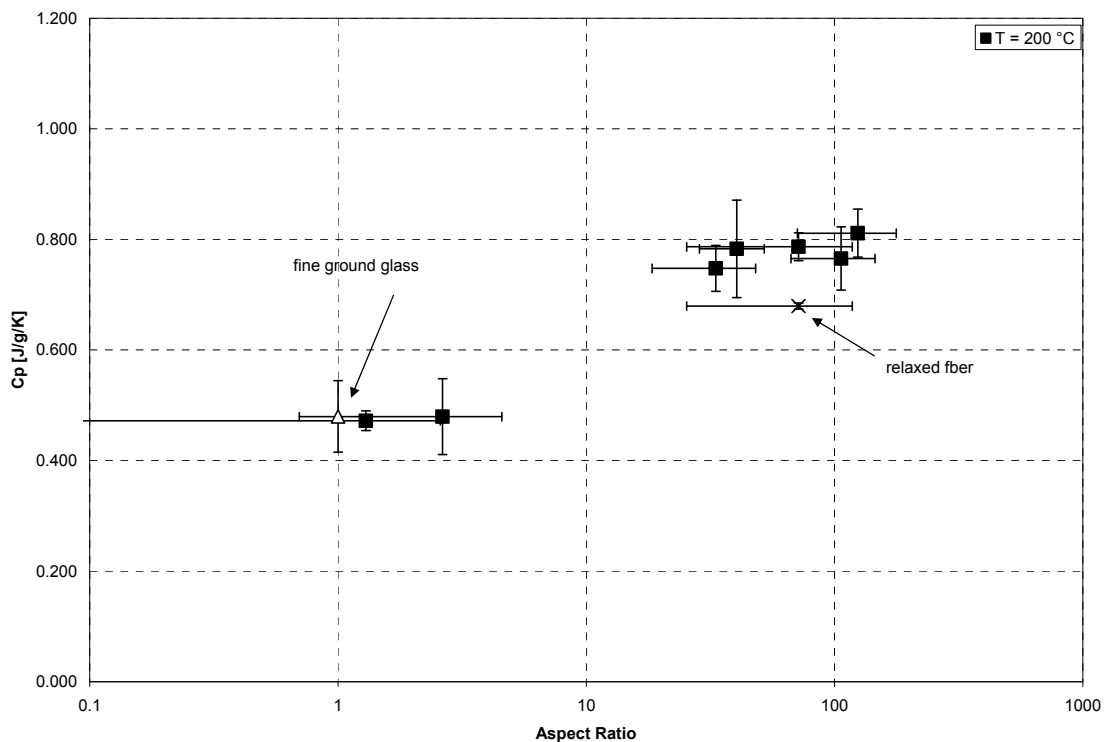


Figure 5.6. Heat capacity dependence of fibers on aspect ratio at 200°C

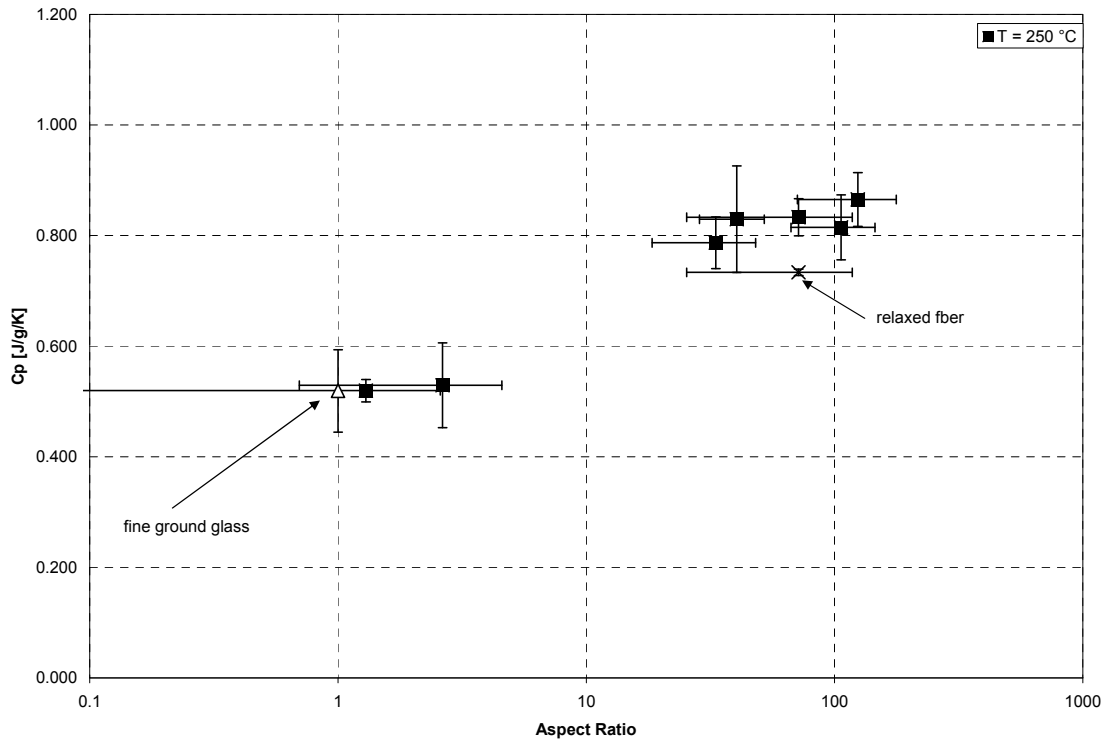


Figure 5.7. Heat capacity dependence of fibers on aspect ratio at 250°C

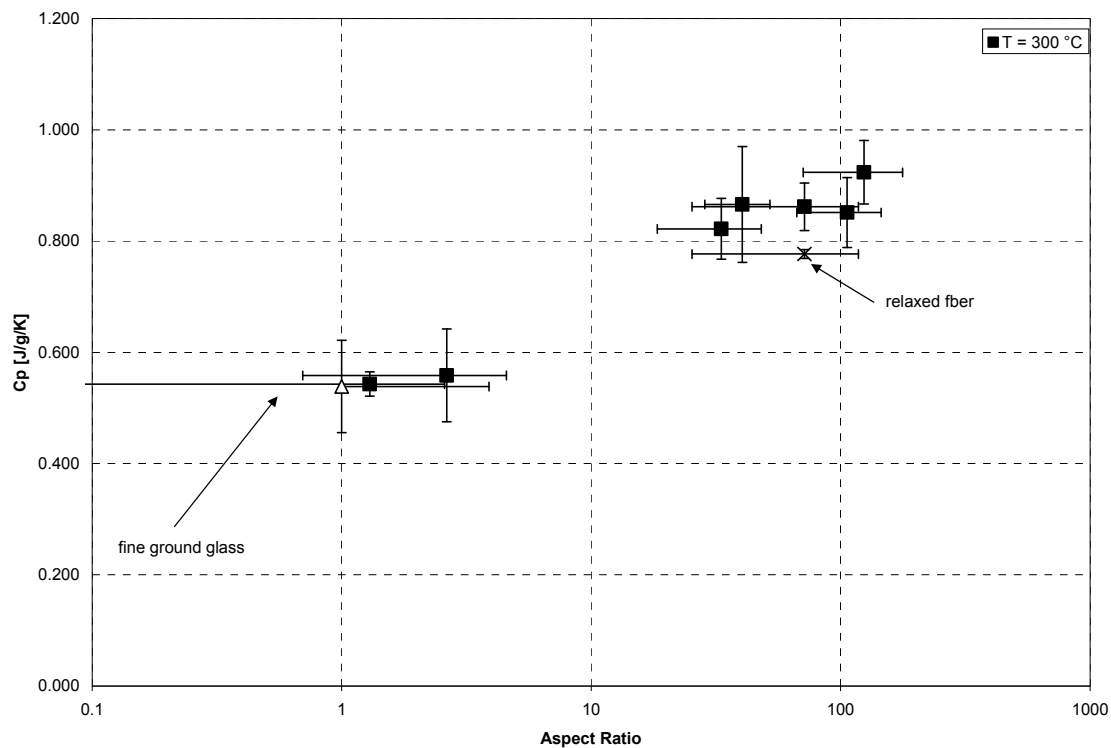


Figure 5.8. Heat capacity dependence of fibers on aspect ratio at 300°C

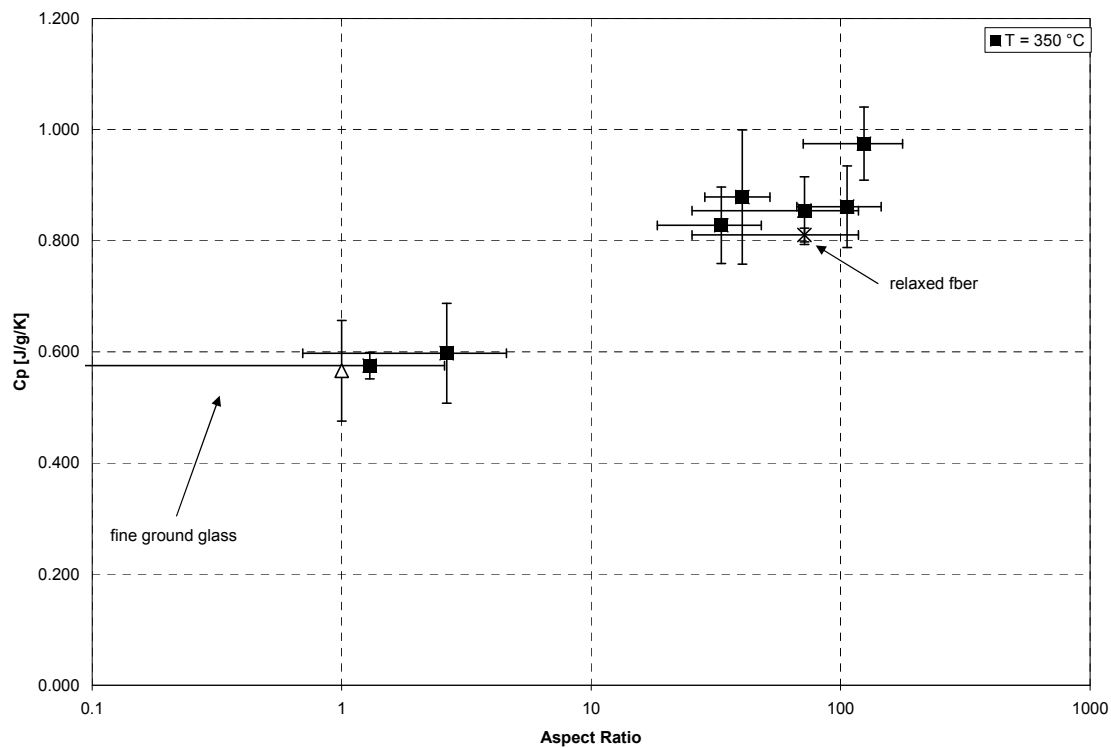


Figure 5.9. Heat capacity dependence of fibers on aspect ratio at 350°C

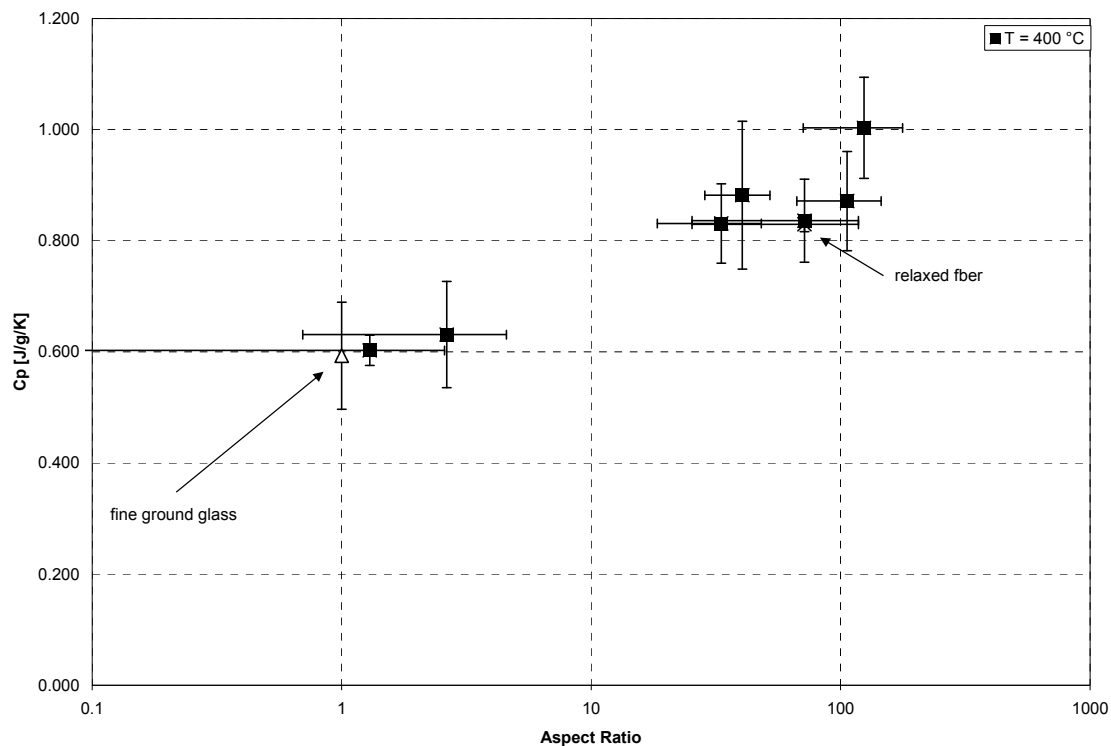


Figure 5.10. Heat capacity dependence of fibers on aspect ratio at 400°C

At the same time the glass transition of the fibers at different aspect ratios was recorded and is shown in Figure 5.11.

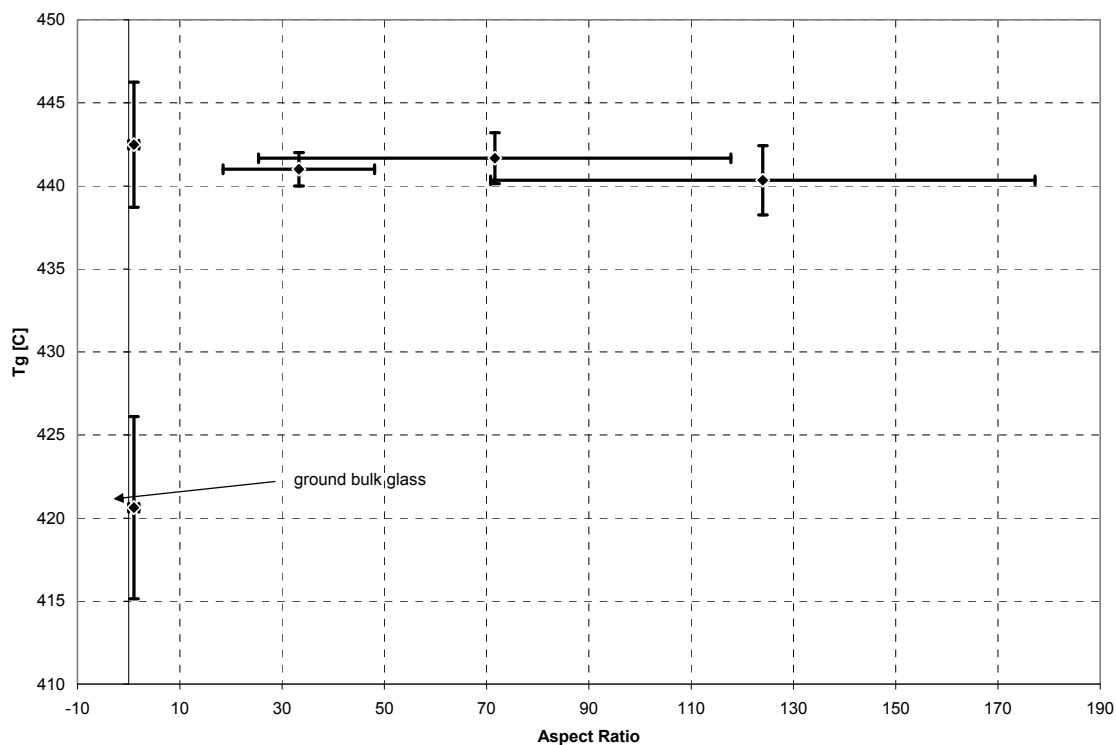


Figure 5.11. T_g dependence of fibers on aspect ratio

The heat capacities were measured below the glass transition region, with the sample temperature never exceeding T_g . Therefore the values shown in Table 5.1 and Figure 5.4 to Figure 5.11 are those of unrelaxed fibers. However, the heat capacity of the fibers with an aspect ratio of 72 ± 46 was also measured with a sample temperature above T_g , resulting in relaxed fibers. The effect of increased heat capacity is somewhat smaller, but still present.

5.5 Discussion and Conclusions

As can be seen in Figure 5.4 to Figure 5.10 there is a marked increase in heat capacity of the fibers after the aspect ratio exceeds 2 – 5. This is true for both the relaxed and unrelaxed fibers, as shown in Figure 5.12. At the same time the glass transition temperatures of the fibers do not change with aspect ratio, but are higher than T_g of the bulk glass.

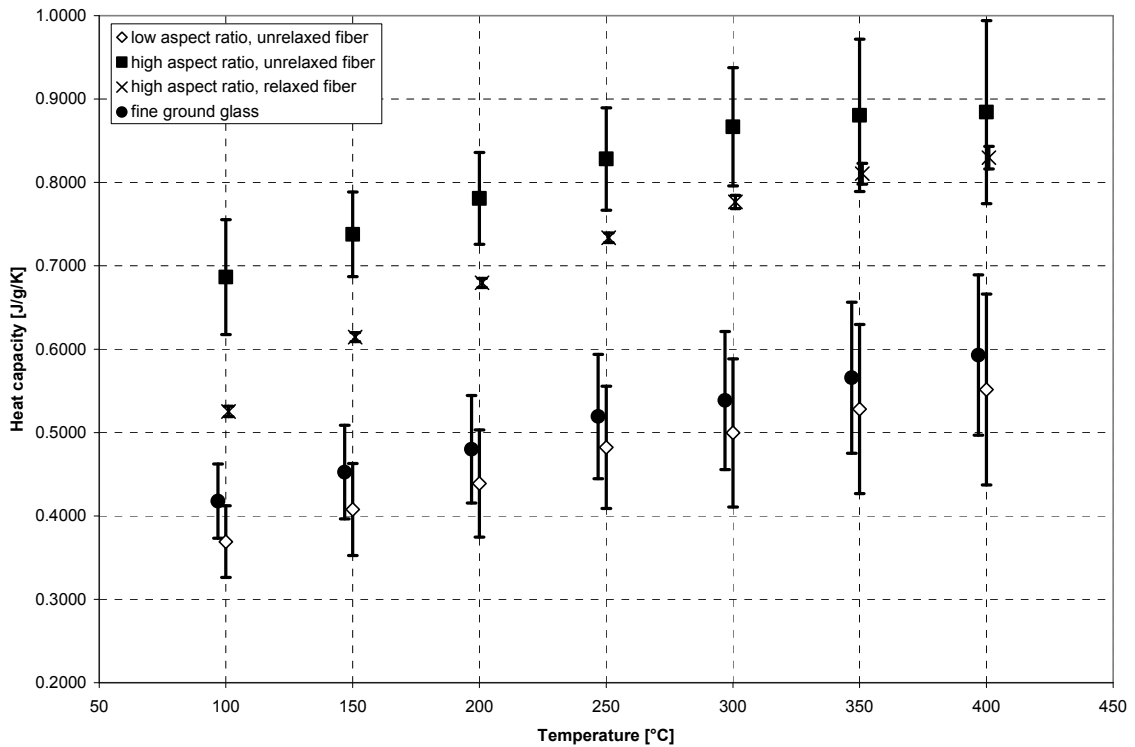


Figure 5.12. Averaged heat capacities for different aspect ratio regions

The general trends are that the heat capacity increases with temperature, which is expected by all models. Also the difference in heat capacity between the high aspect ratio fibers and the low aspect ratio fibers stays the same at any temperature for the unrelaxed fibers.

At the same time the fibers that were heated above T_g , display a different behavior. The difference in heat capacity starts out at roughly 50% of heat

capacity of the high aspect ratio fibers, but as the temperature increases the heat capacity of the relaxed fibers approaches less than 20% of that of the high aspect ratio fibers. This behavior is shown in Figure 5.13.

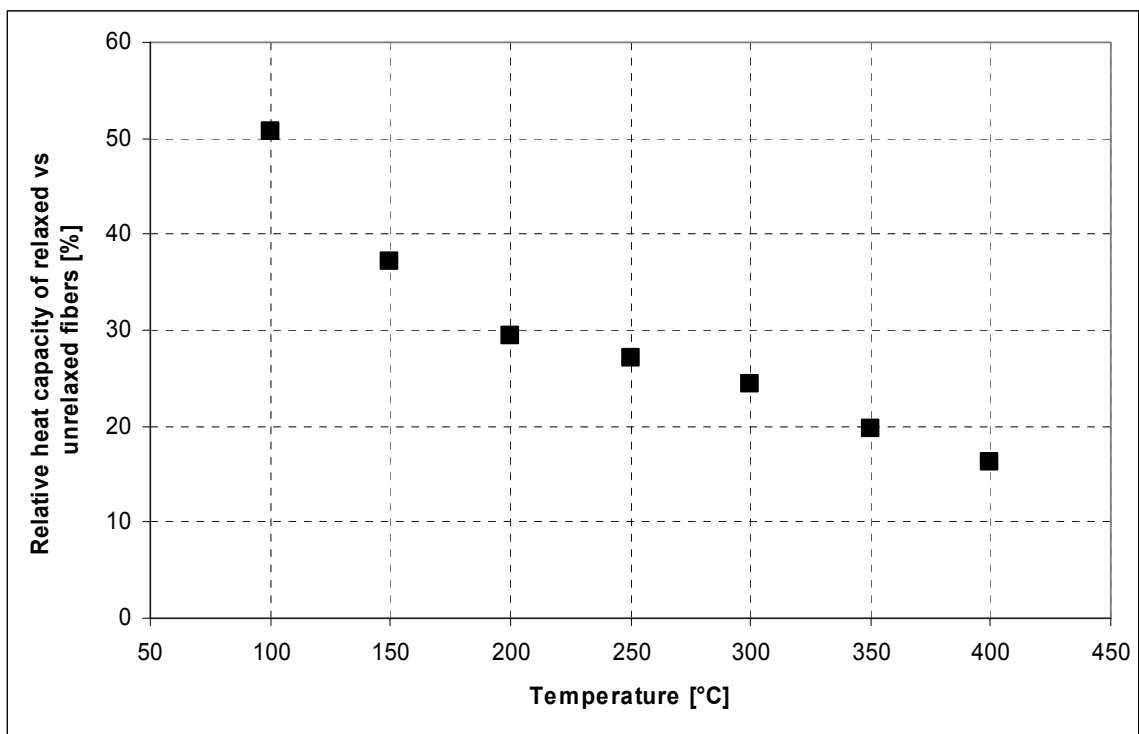


Figure 5.13. Difference in heat capacity between relaxed and unrelaxed fibers at high aspect ratio

The picture is also complicated by the fact that by heating the fiber above T_g one may induce crystallization of the fiber. The DSC plot shows a large exotherm peaking at 586°C as shown in Figure 5.14. The change in the amount of glass can be estimated by measuring the decrease in the distance between the height of the trace before and after the glass transition. The difference between tangents on cycle one is taken to be 0 %, due to the XRD results showing a purely glassy fiber, as seen in chapter 3. Figure 5.15 shows the change in peak height in a fiber sample on reheating up to five times. The plot also shows that the change increases if the temperature to which the fibers were heated increases. This is explained by the fact that at a constant heating rate, the sample heated to a higher temperature spends a longer time above T_g , giving the glass a longer time to crystallize or phase separate.

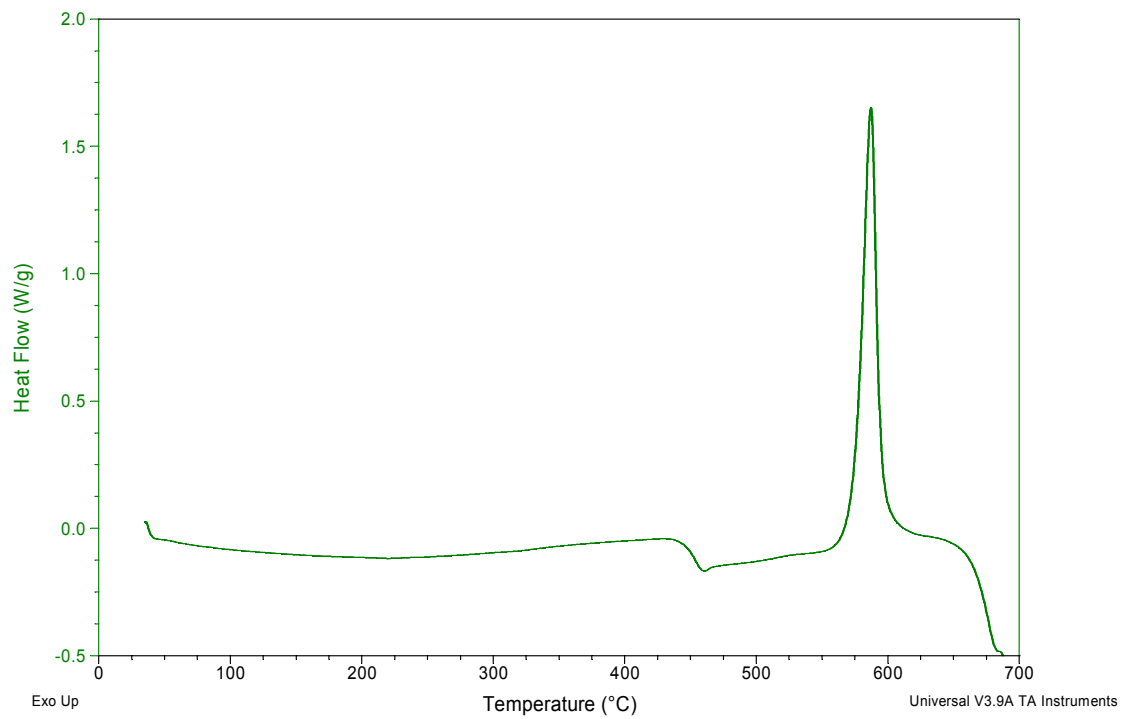


Figure 5.14. DSC plot of fibers heated far above T_g

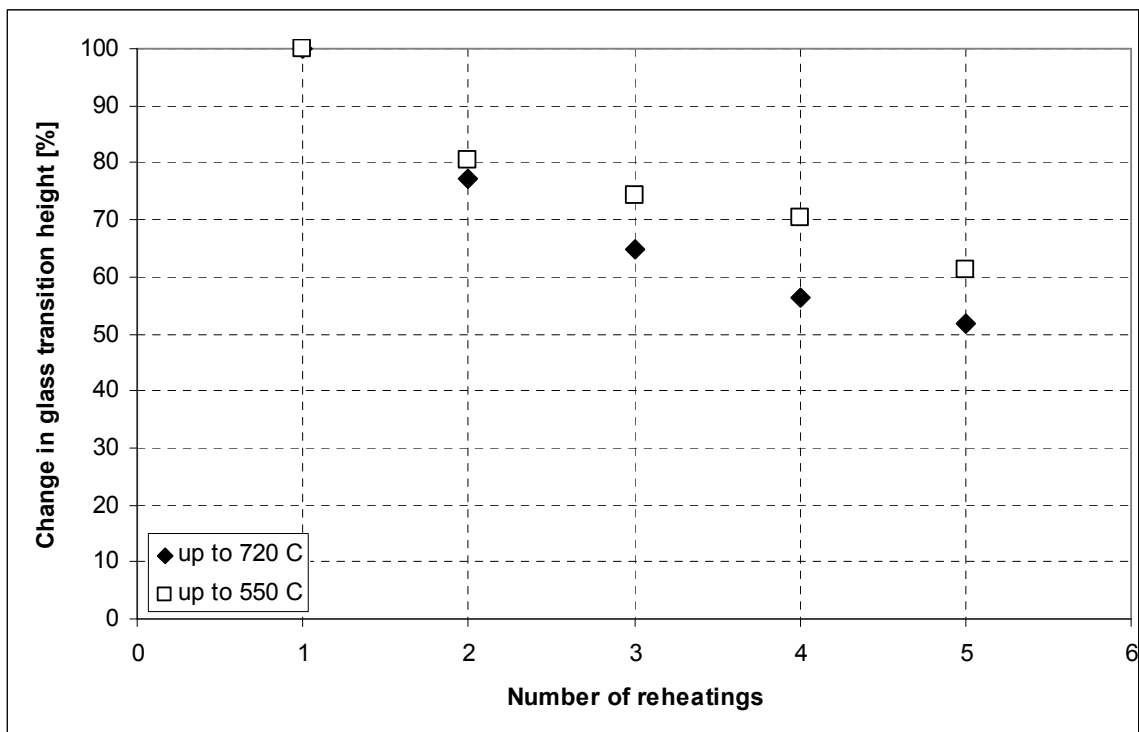


Figure 5.15. Change in glass transition height in fibers upon reheating above T_g

Unfortunately XRD measurements are not sensitive enough to determine the presence of crystals in the sample due to the need to use a zero – background holder with a very small sample size.

The exact origin of the high heat capacity of the fibers at high aspect ratios is unclear. One may assume that there has to be a way of energy storage in the high aspect ratio fibers that is not present in fibers of low aspect ratio fibers or bulk glass.

There are several speculations that may give clues as to the reason.

Energy may be diverted into crystallization. If this were true then the heat capacity at low temperatures should be low as well, since isothermal holds at low temperatures have not produced crystallization. The data shows, however, that the heat capacity of high aspect ratio fibers is high at all temperatures, as is the heat capacity of the relaxed fibers. This indicates that crystallization alone cannot explain this behavior.

Alternatively energy may be stored in surface phonon states. One may speculate that there are surface phonon states that can only be activated if there is a sufficient length in one dimension to support a long wavelength phonon. So as the aspect ratio increases, more of these states become available leading to a higher heat capacity. If this is the case, however, why is the heat capacity at low temperatures lower in the relaxed fibers than in the unrelaxed ones.

Finally, energy may be diverted into relaxing the strained structure produced by fiber drawing. If this were the case, the relaxed fiber, should show a low heat capacity, since heating above T_g will release the pre – T_g exotherm energy. However, the heat capacity of the relaxed fibers is higher than that of the low aspect ratio fibers. The picture of this explanation is confused by the crystallization of the fibers. Of possible influence on the relaxation is the influence of water vapor as described by Tomozawa.⁴ In his paper he describes how the presence of water vapor at elevated temperatures increases the surface relaxation kinetics in fibers more than in bulk material. Since no special precautions were taken to prevent water from entering the hermetically sealed measurement pans, it is reasonable to assume that there would be water

adsorbed onto the surface of the sample. The powder samples, small cut fiber or crushed glass, have a larger surface area than the higher aspect ratio fibers, and the sample mass is constant between all experiments. Therefore the presence of more water in the powder samples could explain the low heat capacities, since one could assume that even after 5 reheating cycles the high aspect ratio fibers are not totally relaxed, whereas in the powder samples, the water vapor has assisted the relaxation to a state much closer to equilibrium. This however does not explain similar effects in amorphous metals, as demonstrated by Raszewski,³ Inoue¹ and Chen,¹¹ nor does it explain the fact that the glass transition temperature stays constant for all samples, since it is well known that T_g is very sensitive to water content in glass.¹²

5.6 References

1. H.S. Chen, "On Mechanisms of Structural Relaxation in a $\text{Pd}_{48}\text{Ni}_{32}\text{P}_{20}$ Glass," *J. Non-Cryst. Solids*, **46** [3] 289-305 (1981).
2. Y.K. Kwon, A. Boller, M. Pyda, and B. Wunderlich, "Melting and Heat Capacity of Gel-Spun, Ultra - High Molar Mass Polyethylene Fibers," *Polymer*, **41** [16] 6237-49 (2000).
3. F.C. Raszewski, "Thermal Analysis of Glass - Covered Amorphous Metal Wires and Amorphous Ribbon for Security Applications"; M.S. Thesis. Alfred University, Alfred, New York, 2004.
4. M. Tomozawa and Y.-L. Peng, "Surface Relaxation as a Mechanism of Static Fatigue of Pristine Silica Glass Fibers," *J. Non-Cryst. Solids*, **240** [1-3] 104-9 (1998).
5. M. Tomozawa and A. Koike, "Size Effect on Surface Structural Relaxation Kinetics of Silica Glass Sample," *J. Non-Cryst. Solids*, **352** [36-37] 3787-93 (2006).
6. N. Sugimoto, "Ultrafast Optical Switches and Wavelength Division Multiplexing (WDM) Amplifiers Based on Bismuth Oxide Glasses," *J. Am. Ceram. Soc.*, **85** [5] 1083-8 (2002).
7. B. Weidenfeller, M. Höfer, and F.R. Schilling, "Thermal Conductivity, Thermal Diffusivity and Specific Heat Capacity of Particle Filled Polypropylene," *Composites: Part A*, **35** [4] 423-9 (2004).
8. A. Guinier and J. Rémi, *The Solid State: from Superconductors to Superalloys*, translated from French by W.J. Duffin; Ch. 1. Oxford University Press, Oxford, England, 1989.
9. C. Kittel, *Introduction to Solid State Physics*; Ch. 5. Wiley, New York, 1996.
10. A. Inoue, T. Masumoto, M. Hagiwara, and H.S. Chen, "The Structural Relaxation Behavior of $\text{Pd}_{48}\text{Ni}_{32}\text{P}_{20}$, $\text{Fe}_{75}\text{Si}_{10}\text{B}_{15}$ and $\text{Co}_{72.5}\text{Si}_{12.5}\text{B}_{15}$ Amorphous Alloy Wire and Ribbon," *Scr. Metall.*, **17** [10] 1205-8 (1983).
11. H.S. Chen and A. Inoue, "Sub T_g Enthalpy Relaxation in PdNiSi Alloy Glasses," *J. Non-Cryst. Solids*, **61-2 Part II** 805-10 (1984).
12. P.B. McGinnis and J.E. Shelby, "Diffusion of Water in Vitreous Silica," *J. Non-Cryst. Solids*, **179** [1] 185-93 (1979).

6 Summary and Conclusions

The characterization of the bulk glass showed that bismuth borate is a normal glass and that the properties of the composition used, with 25 mol% bismuth oxide, agrees well with the values published in the literature. Unfortunately, no literature data on fibers of the same composition was available.

Production of the glass fibers proved somewhat challenging, due to the small draw window this glass exhibits. The extremely steep viscosity curve of the glass made fiber drawing at temperatures above and below the optimum difficult and hard to reproduce. The fiber diameters showed the expected trends. The characterization of the glass fibers showed some interesting phenomena, however. The glass transition temperatures of the fibers all show that for low draw speeds the value of T_g is lower than that for bulk glass and higher draw speeds by as much as 20°C. The glass transition temperatures of fibers drawn at higher speeds are in a similar range as that of the bulk glass. This behavior is shown not only on the first reheating of the glass fiber, which is not relaxed at that time, but on subsequent reheatings as well. It is also interesting to note that T_g decreases again at very high draw speeds. Due to the difficulties in drawing the fibers however, the only draw temperature at which these high speeds could be reached is at the optimum of 550°C.

The pre – T_g exotherm is a measure of the stress on the glass structure that is relieved on reheating. The pre – T_g exotherms show a local maximum at middling draw speeds of circa 4 – 5 m/s depending on draw temperature. The reduction of the pre – T_g exotherms on reheating is equivalent with the healing of stress induced flaws in the glass structure. It is interesting to note that Raman spectroscopy shows a similar result in the spectra. The flaws however seem not to be of severe enough nature that a major structural rearrangement is necessary, as shown by Raman spectroscopy. Raman measurements indicate the presence of $[\text{BiO}_6]$ octahedra. As the draw speed increases, these octahedra are more and more distorted by the bismuth ion assuming a new location in the octahedron. However, since the measurements show a maximum in the intensity of the octahedral band, the conclusion must be that there is an optimum position

for the bismuth ion in the structure. The bismuth ions is prohibited from assuming that optimum position as draw speed increases due to the increasing distortion of the octahedra. An additional band in the spectra shows the formation of additional chain – type metaborate groups but not the formation of new $[\text{BO}_3]$ triangles. This indicates that some decomposition of the structure is taking place but at the draw speeds achieved is not advanced enough to cause the glass to rearrange itself into its most basic arrangement. Pre – T_g exotherm onset temperatures support this conclusion. They decrease with increasing draw speed, showing an increase in flaws in the glass that can be relieved at increasingly lower temperatures. However, the decrease of the onset temperature is nearly linear, indicating that there is no major rearrangement in the fibers, which would cause a departure from linearity. The fictive temperature shows a similar if opposite trend. The fictive temperature of the fibers increases almost linearly with drawing speed but shows no departures from that linearity, indicating a major structural rearrangement.

The drawing conditions show only a small influence on heat capacity.

It is also interesting to note that all the fibers show an additional process happening during the cyclical reheating. The height of the glass transition decreases. This indicates that the amount of glass inside the DSC pan is decreasing. This can be explained by crystallization of part of the glass. DSC measurements show a large exotherm in the trace on the first reheating. And a steady decrease of the glass transition height on subsequent cycles. XRD measurements, however, do not detect any crystals in the sample. This may be due to the fact that the crystal fraction is too small to detect with the type of XRD measurement performed. The fiber is not completely crystallized, as shown by the fact that there is still a measureable glass transition even after five reheating cycles.

The last puzzling aspect of amorphous fibers in general investigated in this work is the influence of aspect ratio on the heat capacity of fibers. As the aspect ratio of the examined fibers increases, the heat capacity increases after a certain threshold value in a step like fashion. This means that the increase is sudden

and it does not continue to increase with aspect ratio but assumes a new plateau. This behavior cannot be explained by any simple phenomenon. The most likely assumption is that there is a combination of mechanisms at work. The untangling of these mechanisms would likely provide great insight into the phenomenon of heat capacity in general and that of amorphous fibers in particular.

Finis delectat.

JW